The Pennsylvania State University

The Graduate School

ROTORCRAFT FLIGHT CONTROL DESIGN WITH ALLEVIATION OF UNSTEADY ROTOR LOADS

A Dissertation in

Aerospace Engineering

by

Umberto Saetti

Submitted in Partial Fulfillment

of the Requirements

for the Degree of

Doctor of Philosophy

August 2019

The dissertation of Umberto Saetti was reviewed and approved* by the following:

Joseph F. Horn
Professor of Aerospace Engineering
Dissertation Co-Advisor, Committee Co-Chair

Constantino Lagoa
Professor of Electrical Engineering
Dissertation Co-Advisor, Committee Co-Chair

Edward C. Smith
Professor of Aerospace Engineering

Puneet Singla
Associate Professor of Aerospace Engineering

Stephanie Stockar
Assistant Professor of Mechanical Engineering

J. V. R. Prasad
Professor of Aerospace Engineering
Special Member

Amy R. Pritchett
Professor of Aerospace Engineering
Department Head

*Signatures are on file in the Graduate School.

Abstract

The objective of this research effort is to develop rotorcraft flight control laws that minimize unsteady rotor loads by acting solely through the primary flight controls (1^{st} harmonic swashplate control). As opposed to Higher-Harmonic Control, this strategy does not affect stationary (periodic trim) loads, and is therefore effective only in maneuvering flight. However, such system could be readily integrated with existing or future Automatic Flight Control Systems (AFCS). The study considers control designs for both conventional and compound configurations.

Starting from a non-linear simulation model of the rotorcraft developed in FLIGHTLAB®, which includes sufficient fidelity to simulate rotor loads and vibrations, Linear Time-Periodic models (LTP) are derived via linearization. Next, the Harmonic Decomposition methodology is used to approximate the LTP systems with higher-order Linear Time-Invariant (LTI) systems. Reduced-order systems are subsequently obtained by using singular perturbation theory. By retaining the higher-harmonics of the rotor loads in the output, the reduced-order models are shown to accurately predicted the influence of the 0^{th} harmonics of the rigid-body and rotor flapping states on the higher-harmonics of the rotor loads. This way, previous limitations such as the reliance on non-physics-based models and curve fits to approximate rotor loads are lifted. Next, model following flight control laws are developed based on the reduced-order models. Parametric studies are performed to provide insights on how both the feed-forward and feedback paths of the model following control laws can be used to alleviate the rotor loads. Also, the impact of load alleviation on handling qualities is studied.

It is shown that, for a standard helicopter configuration, load alleviation comes at the cost of a degradation in handling qualities. However, for the case of a compound rotorcraft, allocation of the control signal to the redundant control surfaces provides load alleviation without degradation in the handling qualities.

The flight control laws are subsequently optimized using CONDUIT® to meet a comprehensive set of stability, handling qualities, and performance specifications for specific mission task elements while minimizing the unsteady rotor loads.

Finally, since industry will not only rely on LTP systems obtained from simulation models, a novel methodology is developed to identify LTP systems from flight test data. The methodology is successfully applied to JUH-60A Black Hawk flight test data using CIFER®. The identified LTP systems capture the N_b/rev component of the rotorcraft dynamics. Further, it is shown how the higher-harmonics of the rotor states contribute to the overall rotorcraft dynamics for up to a 7%. On the other hand, the rigid-body states contribute to the overall rotorcraft dynamics almost entirely through their 0^{th} harmonic.

Flight control design based on LTP systems identified from flight-test data could benefit the Future Vertical Lift (FVL) program. FVL is a plan to develop a new generation of military helicopters for the U.S. Army with increased capabilities in speed, range, and payload, and reduced maintenance and operational cost. Because these rotorcraft would operate at significantly higher speeds than the current helicopters, alleviation of the higher harmonic rotor loads and flight envelope protection are key elements to reduced maintenance cost. These rotorcraft are also likely to employ redundant control surfaces which, in connection with LTP-based flight control design, demonstrated outstanding effectiveness towards the alleviation of unsteady rotor loads.

Table of Contents

List of Figures

List of Tables

Nomenclature

Mathematical Symbols

$\mathbf{A}$	Linear Time-Invariant System State Matrix
a_z	Vertical Acceleration
$\mathbf{B}$	Linear Time-Invariant System Control Matrix
$\mathbf{C}$	Linear Time-Invariant System Output Matrix
$\mathbf{D}$	Linear Time-Invariant System Feed-Through Matrix
$\mathbf{d}$	Pseudo-Input Vector
$\mathbf{F}$	Linear Time-Periodic System State Matrix
$\mathbf{G}$	Linear Time-Periodic Input State Matrix, Pseudo-Inverse Ganging Matrix
g	Gravitational Acceleration J Average System Identification Cost Function, Linear Quadratic Regulator Cost Function
$k_{\delta_{\text{lat}}}$	Roll Command Filter Gain
$k_{\delta_{\text{lon}}}$	Pitch Command Filter Gain
$k_{\delta_{\text{ped}}}$	Yaw Command Filter Gain
L	Number of Output Harmonics Retained
L_p	Roll Damping Derivative
m	Main Rotor Blade Number
$M_{f_{\beta_{1c}}}$	Longitudinal Flap Angle Rate Due to Longitudinal Flap Angle
$M_{f_{\delta_{\text{lon}}}}$	Longitudinal Flap Angle Rate Due to Longitudinal Stick
M_w	Pitch Acceleration Due to Vertical Speed

M_q	Pitch Acceleration Due to Pitch Rate
$M_{\beta_{1c}}$	Pitch Acceleration Due to Longitudinal Flap Angle
M_q	Pitch Acceleration Due to Pitch Rate
N	Number of State Harmonics Retained
N_b	Number of Blades
N_r	Yaw Damping Derivative
n_t	Number of Time-History Points
$\mathbf{P}$	Linear Time-Periodic Output State Matrix
p	Roll Rate
PLL	Pitch Link Load
$\mathbf{Q}$	Linear Quadratic Regulator State Penalty Matrix
q	Pitch Rate
$\mathbf{R}$	Linear Time-Periodic Feed-Through State Matrix, Linear Quadratic Regulator Controls Penalty Matrix
r	Yaw Rate
T	Fundamental Period
t	Dimensional Time
$\mathbf{U}$	Linear Time-Invariant System Input Vector
$\mathbf{u}$	Linear Time-Periodic System Input Vector
$\mathbf{W}$	Pseudo-Inverse Weighting Matrix
$\mathbf{w}$	Linear Quadratic Regulator Weight Vector
$\mathbf{X}$	Linear Time-Invariant System State Vector
$\mathbf{x}$	Linear Time-Periodic System State Vector
$\mathbf{x}_b$	Bias Vector
$\mathbf{Y}$	Linear Time-Invariant System Output Vector
$\mathbf{y}$	Linear Time-Periodic System Output Vector
$\mathbf{y}_{\text{ref}}$	Reference Shift Vector
Z_w	Vertical Speed Rate Due to Vertical Speed
Z_q	Vertical Speed Rate Due to Pitch Rate
$Z_{\beta_{1c}}$	Vertical Speed Rate Due to Longitudinal Flap Angle

$Z_{\delta_{\text{lon}}}$	Vertical Speed Rate Due to Longitudinal Stick
β	Main Rotor Flapping Angle
Δ_t	Simulation Time Step
δ_{dif}	Differential Flaperons Input
δ_{lat}	Lateral Stick Input
δ_{lon}	Longitudinal Stick Input
δ_{ped}	Pedal Input
δ_{stb}	Stabilator Input
δ_{sym}	Symmetric Flaperons Input
θ	Pitch Attitude
θ_0	Trim Pitch Attitude
τ_p	Roll Command Filter Time Constant
τ_q	Pitch Command Filter Time Constant
τ_r	Yaw Command Filter Time Constant
τ_ϕ	Roll Equivalent Time Delay
τ_θ	Pitch Equivalent Time Delay
τ_ψ	Yaw Equivalent Time Delay
ψ	Main Rotor Azimuth Angle (Non-Dimensional Time)
Ω	Main Rotor Angular Speed
Ω_f	Fundamental frequency
ω_L	Parametric Identification Lower Limit
ω_p	Roll Command Filter Break Frequency
ω_q	Pitch Command Filter Break Frequency
ω_r	Yaw Command Filter Break Frequency
ω_U	Parametric Identification Upper Limit

Subscripts

cmd	Command
e	Equilibrium
f	Fast

fb	Feedback
ff	Feed-Forward
nc	n^{th} Cosine Harmonic
ns	n^{th} Sine Harmonic
R	Rotor
RB	Rigid Body
s	Slow
0	Zeroth Harmonic, Coning
$0d$	Differential Coning
$1c$	Longitudinal Cyclic
$1s$	Lateral Cyclic

Acronyms

AFCS	Automatic Flight Control System
CFM	Carefree Maneuvering
DMC	Damage Mitigation Control
DRB	Disturbance Rejection Bandwidth
DRP	Disturbance Rejection Peak
ERITS	Equivalent Retreating Indicated Tip Speed
FBW	Fly By Wire
HHC	Higher-Harmonic Control
IBC	Individual Blade Control, Individual Blade Coordinates
LAC	Load Alleviation Control
LQR	Linear Quadratic Regulator
LTI	Linear Time-Invariant
LTP	Linear Time-Periodic
MBC	Multi-Blade Coordinates
MTE	Mission Task Element
MUAD	Maximum Unnoticeable Added Dynamics
OBC	On-Blade Control

RBFB	Rigid-Body Feedback
RCAH	Rate Command / Attitude Hold
RMS	Root Mean Square
RSF	Rotor State Feedback
RSFB	Rotor State Feedback
SCAS	Stability and Control Augmentation System

Acknowledgments

This research was partially funded by the Government under Agreement No. W911W6-17-2-0003. The U.S. Government is authorized to reproduce and distribute reprints for Government purposes notwithstanding any copyright notation thereon. The views and conclusions contained in this document are those of the authors and should not be interpreted as representing the official policies, either expressed or implied, of the Aviation Development Directorate or the U.S Government.

First and foremost, I would like to thank my advisor, Joseph F. Horn, for his support and patience in showing me the ropes of research, and for being an impeccable example of fairness and hard work.

I wish to thank the members of my dissertation committee: Ed Smith, Constantino Lagoa, Stephanie Stockar, Puneet Singla, and J.V.R. Prasad for offering their time, support and guidance throughout the preparation and review of this document.

My gratitude also goes to Prof. Marco Borri, advocate of my acceptance at Penn State and pursuit of rotorcraft studies.

Great inspiration and advice was provided to me by U.S. Army Aviation Development Directorate (ADD) at NASA Ames. Particularly, I wish to thank Tom Berger for his guidance and friendship, Mark Lopez for sharing the algorithms developed during his PhD, and Mark Tischler for his unfailing enthusiasm, for having me at Ames for a period of time, and for providing me with the flight test data used in this research.

The long hours spent at the Vertical Lift Research Center of Excellence (VLRCOE) created a great comradery among my fellow collegues, especially Junfeng Yang, Ilker Oruc, Keerti Prakash, Ahmad Haidar, Yu Xiong, Tanmay Mathur, Ethan Corle, and Regis Thedin, which I thank for the help with the difficulties and questions arisen along the way, and for the countless nights at Cafe 210 across the street from the research center.

I probably would have not been able to achieve the perseverance necessary for doctoral studies without the continued support and patience of my girlfriend of four years, Valeria. This achievement is a shared effort.

Finally, I would like to thank my family for their love and encouragement in cultivating my passions and enthusiasm.

Dedication

To my parents, grandparents, and brothers for their love and support.

Chapter 1

Introduction

1.1 Problem Motivation

Rotorcraft are difficult to fly due to their inherent unstable flight dynamics, high order dynamics, and inter-axis coupling. Because of their unstable flight dynamics, rotorcraft have no tendency to hold trim attitude at low and speeds so that the pilot must actively regulate all four control axes, effectively acting as a feedback control system. Further, rotocraft have a restrictive flight envelope due to complex power and structural limits that need to be monitored by the pilot, which greatly contributes to the pilot workload. This task is generally demanding and can be alleviated by the use of Automatic Flight Control Systems (AFCS), as shown in Fig. 1.1. The primary role of the flight control system is to improve the handling qualities of the aircraft, alleviate pilot workload, and to yield to a simple and predictable closed-loop dynamic response to a commanded output.

For a conventional single rotor helicopter pilots have four primary controls, as shown in Fig. 1.2 and described as follows. Lateral cyclic is a left/right displacement of the center stick that provides bank angle control through lateral rotor disk tilt. Longitudinal cyclic is a fore/aft displacement of the center stick that provides pitch control through longitudinal rotor disk tilt. Collective corresponds

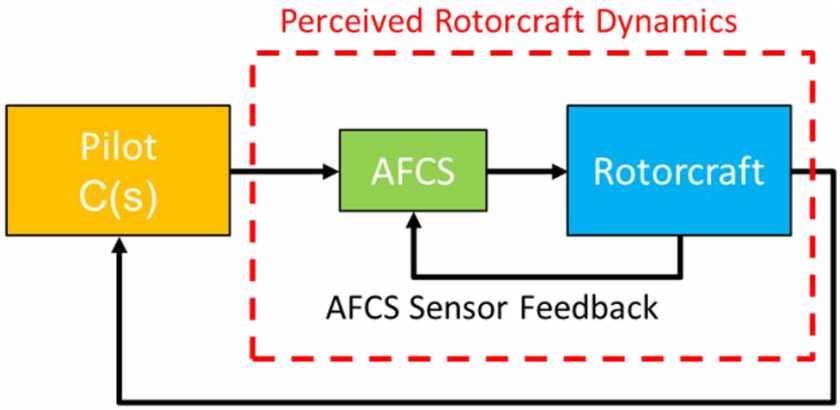

Figure 1.1: Automatic Flight Control System.

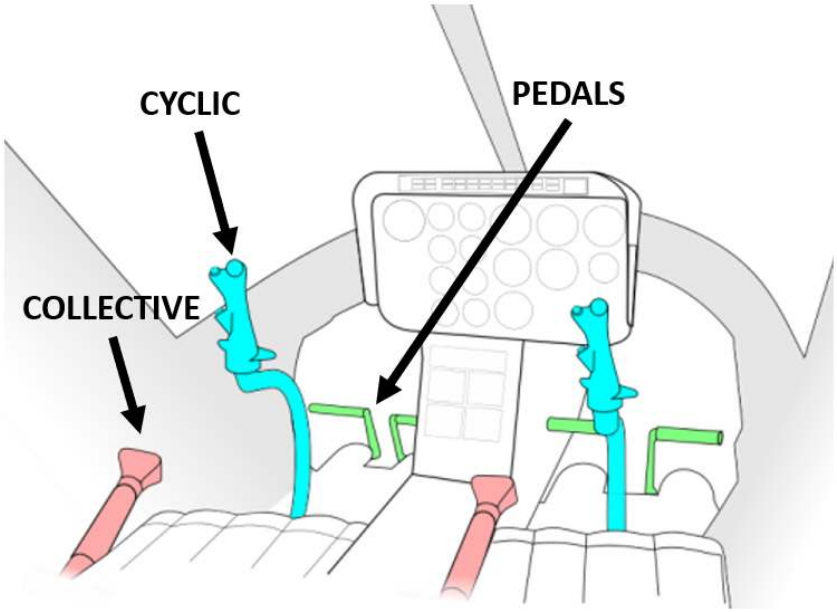

Figure 1.2: Helicopter primary controls (http://www.airliners.net).

to an up/down movement of the left hand lever that changes the main rotor thrust. Pedals provide yaw control through tail rotor collective pitch. Forward and lateral speed are indirectly controlled through the aircraft attitude. The same control axes are used for other rotorcraft configurations, but with different mechanisms to effect control (e.g. differential lateral cyclic on a tandem for yaw axis control). The response type of a helicopter is rate command, meaning that pilot inputs are directly proportional to angular rates response.

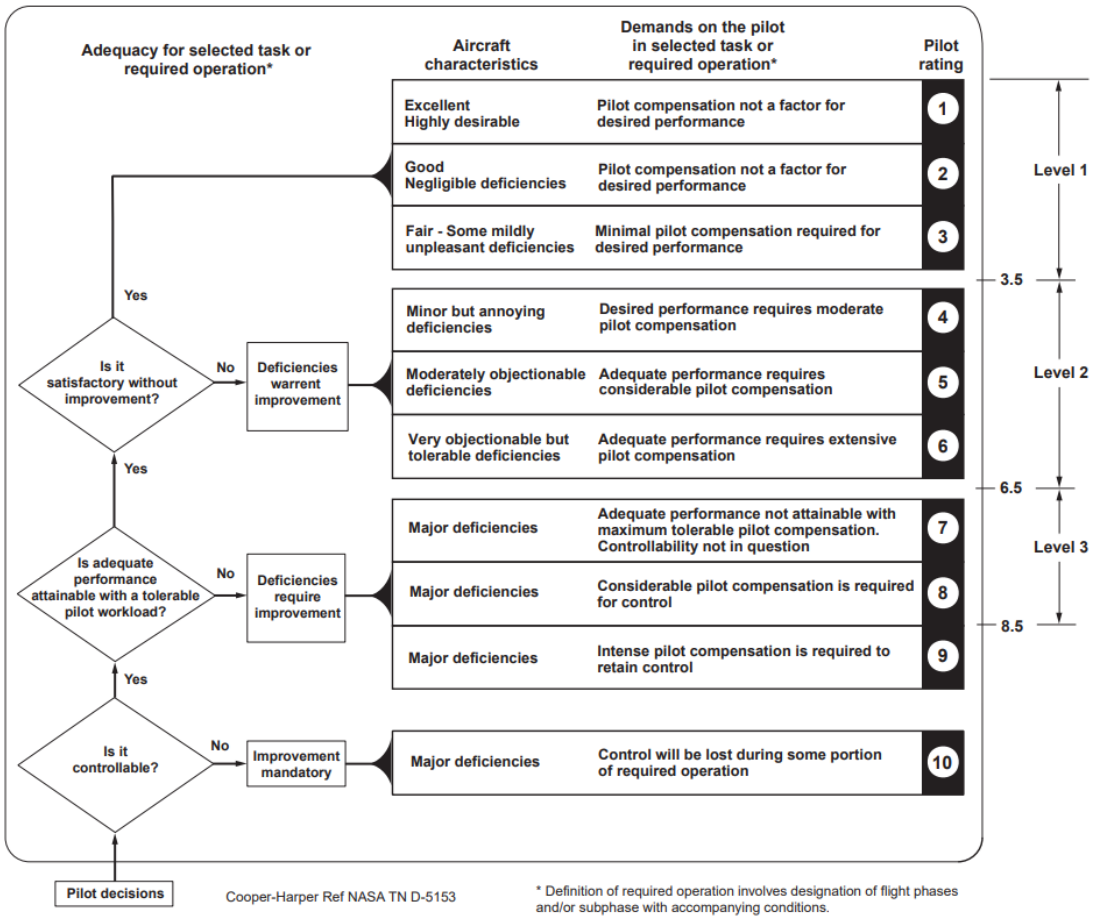

Figure 1.3: Cooper-Harper handling qualities rating scale [1].

Rotorcraft handling qualities describe the ease and precision with which a pilot can perform a rotorcraft mission. Handling qualities are evaluated both subjectively and objectively. The subjective measure is provided by the pilot's rating when performing a Mission Task Element (MTE). The rating is assigned on a scale from 1 ("Good") to 10 ("Very Bad"). Guidelines for pilot ratings are given by the Cooper-Harper handling qualities rating scale of Ref. [1], also shown in Fig. 1.3. The objective evaluation consists of a quantitative measure of the rotorcraft characteristics and stability that define the handling qualities "Level". The level ranges from 1 ("Good") to 3 ("Bad"). The handling qualities standards are defined in the Aeronautical Design Standards 33 (ADS-33) [2].

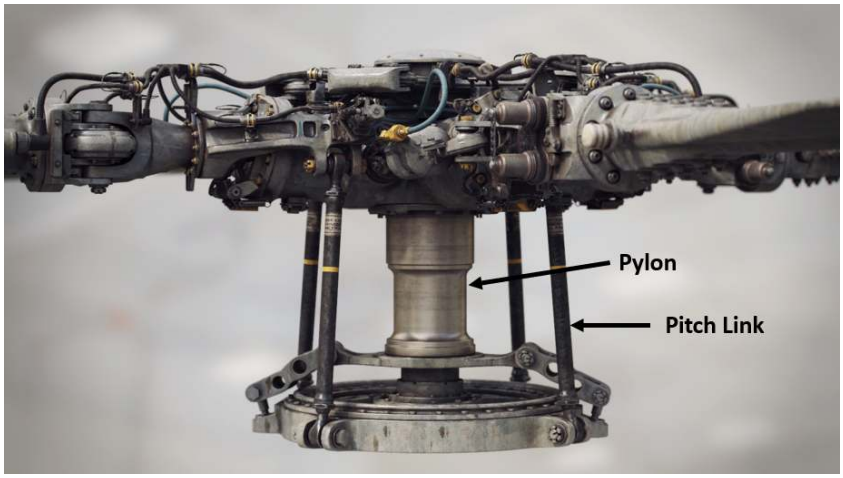

Figure 1.4: UH-60 Black Hawk Rotor Hub (www.artstation.com).

Previous research has shown direct correlation between commanded angular rates/accelerations and rotor loads [3]. The rotor loads are transmitted to the fuselage in two ways: through the main rotor shaft and through the pitch links (Fig. 1.4). The main rotor shaft transmits the loads to the transmission and thus to the fuselage, whereas the pitch links are the connection between the rotating and non-rotating frame of the helicopter and transmit the loads to the fuselage through the the control. The rotor loads, especially with increasing forward speed, are cyclic in nature and contribute to the fatigue of rotor components. Fatigue is directly related to the components life [3]. Reducing rotor loads, thus extending component life, can lead to reduced maintenance costs. Put in the perspective of a fleet of rotorcraft, this could lead to significant savings in maintenance cost.

Legacy rotorcraft use partial authority flight control systems that are mechanically linked with the pilot sticks. These Stability and Control Augmentation Systems (SCAS) typically provide limited feed-forward/feedback control authority, up to 10%. Newer rotorcraft employ full authority Fly-by-Wire (FBW) systems. Sensors measure the pilot inceptors and aircraft state and feed them to the flight control computer. The flight control computer then calculates the necessary compensation and directly controls the actuators. This gives to engineers the freedom

to tailor stability and control up to the limits of actuation and state observability. For this reason, there is increasing interest in recent years to alleviate the rotor loads by means of the flight control system. Specifically, the flight control system is designed to act on the commanded angular rates/accelerations such that the rotor loads are reduced. The research area that studies this problem is referred to as Load Alleviation Control (LAC).

The benefits of load alleviation control and envelope cueing have been demonstrated in numerous simulation studies [3–10]. The use of AFCS or active control sticks to help the pilot observe structural constraints can extend the life of critical dynamic components and reduce cost of operation. These technologies can also improve handling qualities by alleviating pilot workload associated with monitoring envelope limits. Load alleviating controls have been implemented on the V-22 tilt-rotor aircraft, using cyclic pitch control to reduce in-plane loads during forward flight maneuvers [11].

Many of the critical structural limits on rotorcraft are associated with vibratory loads and fatigue limits. These loads are strongly influenced by higher harmonic (greater than 1/rev) dynamics in the rotor systems. These dynamics are not modelled in the Linear Time-Invariant (LTI) dynamic models normally used for rotorcraft primary flight control design. Past work in the design of load limiting control laws has used proxy models of the vibratory loading. An example is the Equivalent Retreating Indicated Tip Speed (ERITS) parameter, which has been correlated with vibratory pitch link loads that occur with retreating blade stall onset [6]. Vibratory load limiting has also been demonstrated using basic correlations, curve fits, or neural network approximations of vibratory loads as a function of aircraft states (angular rates, accelerations, load factor, airspeed) [3–5].

Reliance on non-physics-based models and curve fits to approximate vibratory loads is a limitation of past work. On the other hand, Linear Time-Periodic (LTP) models are well-suited for representing vibratory loads on rotorcraft, including the

dominant N_b/rev vibratory forces and moments at the hub and associated dynamic components, and they can be derived directly from the physics-based models. Recently, methods have been developed for approximating LTP systems using high order LTI models [12,13]. The harmonic decomposition method transforms higher frequency harmonics into states of an LTI state space model. Harmonic decomposition methods have been used to model interactions between Higher-Harmonic Control (HHC) systems and the primary AFCS and to optimize the design of these systems to reduce vibration and provide stability and handling qualities augmentation, where the HHC is primary responsible for vibratory load reduction.

While the use of harmonic decomposition method for HHC/AFCS design has been well-studied, the method has not yet been applied towards design of load alleviation control and cueing methods that act solely through the primarily flight controls (1st harmonic swashplate control) and AFCS. Previous studies have shown that tailoring of response characteristics through limiting or modification of response bandwidth can significantly reduce vibratory loads, and could be significantly cheaper to implement on existing rotorcraft. The objective of this research is to extend the harmonic decomposition methodology to enable optimization of primary flight control laws that alleviate vibratory loads while meeting desired handling qualities. The use of high order LTI models is used to derive correlations of the controlled aircraft states to main rotor vibratory loads directly from the linearized physics model. In particular, the high order LTI models are reduced and used to design an EMF controller with LQR feedback optimized to reduce changes in vibratory loads.

1.2 Previous Research

This section provides a comprehensive summary of published research inherent to the topics touched by this thesis. The five main research topics include:

- *Linear Time-Invariant Approximations of Linear Time-Periodic Systems* - The vast majority of control system design is based on LTI theory and, although control design methodologies based on LTP systems exist, they are of difficult implementation. LTI approximations of LTP systems retain information on vibratory loads, as opposed to standard LTI systems normally used for primary flight control design. The relatively recent development of LTI approximations of LTP systems has enabled HHC design in maneuvering flight and the study of interactions between HHC and AFCS.

- *Carefree Maneuvering* (CFM) - Originally researched for fixed-wing aircraft, it was first seen in the rotorcraft community for applications to the V-22 Osprey tilt-rotor. It represents the ability of a pilot to fly throughout the operational flight envelope without concern for exceeding structural, aerodynamic, or control limits.

- *Load Alleviation Control* (LAC) - It minimize loads that reduce component life through tailoring of response and automatic control intervention.

- *Damage Mitigation Control* (DMC) - Assists pilots in observing structural load constraints through cueing or automatic control intervention. Often times DMC is achieved through LAC.

- *Compound Rotorcraft Vibration Reduction* - A small amount of studies focused on the optimization of redundant control allocation to minimize vibratory loads in trim. However, very little to none published research exists on redundant control allocation to minimize vibratory loads in maneuvering flight.

1.2.1 Linear Time-Invariant Approximations of Linear Time-Periodic Systems

The formulation of linear time periodic systems dates back to the late nineteenth century and it is attributed to Floquet [14]. This enabled the reduction of real-world systems that operate under a periodic regime with to an LTP formulation under the assumption of small perturbations. It was not until 1990 that a frequency response notion comparable to the classical LTI Bode gain and phase response was developed for LTP systems at MIT. Wereley and Hall [15–17] developed a comprehensive open loop analysis theory for LTP systems, including a characterization of poles, transmission zeros and their directional properties, a generalized Nyquist criterion, and a comprehensive frequency domain interpretation. The fundamental notion behind the development of LTI systems is that a sinusoidal input with a given frequency is mapped by the LTI transfer function operator into a sinusoidal output of the same frequency, but with possibly a different amplitude and phase. In contrast, if a sinusoid is fed to an LTP system, multiple sinusoids may appear in the output at the input frequency plus or minus multiples of the fundamental frequency of the LTP system, each with possibly different amplitude and phase. Further, an infinite number of sinusoids may appear in the output of an LTP system at steady state. The transfer function for LTP systems that was developed, also known as harmonic transfer function, maps geometrically periodic input signals to geometrically periodic output signals when the system is at steady state. Although this theory provides a comprehensive analysis of LTP systems, it is inconvenient when performing controller design.

The very first effort to approximate LTP systems with LTI models in the rotorcraft community is dated 1969 and is attributed to Crimi and Piarulli [18, 19]. The approximation consisted in expanding the LTP states into harmonic state coefficients and formulating the corresponding LTI model.

Successively, in the early 2000's, Cheng, Tischler, and Celi [20] developed a

numerical scheme to directly obtain a LTI approximation of a nonlinear system that captures the nonlinear system's periodic nature. This was accomplished by subjecting the nonlinear system to harmonic perturbations during the linearization procedure. Although the procedure was promising, it was only applied to a relatively simple helicopter model with rigid blades and a 3 state Pitt-Peters inflow model.

In the late 2000's Prasad and Olcer et al. [21–24] demonstrated how a high-order LTI model representative of the rotor periodic nature is obtained using a two-step procedure. First, a LTP model is extracted by linearizing the nonlinear dynamics of the helicopter about a periodic equilibrium at incremental azimuthal steps over one rotor revolution. Second, a harmonic decomposition is performed on the LTP system states to obtain an approximated high-order LTI model. The finite number of harmonics to retain in the LTI system is arbitrarily chosen. Although this numerical scheme has shown success and has seen to improve computational speed by an order of magnitude when compared to previous numerical schemes from the literature, it relies on a second order formulation of the original LTP system. This second order formulation can be problematic for degrees of freedom not explicitly represented in second order form. In particular, difficulties arise when applying harmonic decomposition to body and inflow states.

A more general formulation that accurately captures the higher harmonic dynamics relative to degrees of freedom not explicitly in second order form is proposed by Lopez and Prasad, starting from 2013 [12, 25, 26]. This formulation relies on a first-order representation of an LTP system. This technique has proven to accurately approximate nonlinear time periodic models by including the effects of coupling harmonic terms for body, inflow, and rotor degrees of freedom.

The origin of Higher Harmonic Control (HHC) where the swashplate is actuated at higher harmonic frequencies, On-Blade Control (OBC) where HHC inputs are fed to actuators on each blade, and Individual Blade Control (IBC) where each

blade input is actuated independently, can be traced as far back as 1967, when Shaw [27] first proposed different approaches to active vibration control on rotorcraft. A comprehensive survey of the different approaches and their history can be found in [28]. Before the formulation of LTI approximations to LTP systems, HHC, OBC, and IBC were only studied in trim flight. High-order LTI systems enabled to extend the different active vibration control techniques for rotorcraft to maneuvering flight.

The first look at interactions between HHC and AFCS in maneuvering flight was taken by Cheng and Abraham et al. [20, 29]. Observations showed that significant coupling between HHC and AFCS exists when the two are designed independently, resulting in a performance degradation. These studies concluded that to address the coupling between AFCS and active rotor control systems while retaining performance, an integrated flight and rotor control system is needed.

This direction in research was taken by Lopez and Padthe et al. [13,30,31] who respectively concentrated on HHC and OBC interactions with the flight control system. The studies focused on validating reduced-order models derived from high-order LTI systems for integrated HHC/OBC and AFCS control design. The reduced-order models proved to capture the relevant dynamics and to be suitable for closed-loop vibration control, as long as dynamic stall effects are not significant.

This study uses Prasad and Lopez's formulation [12, 25, 26] to obtain reduced order models that capture the influence of the 0^{th} harmonic of the rigid-body, rotor flapping states, and input on the rotor loads. These models are used to synthesize a controller that minimizes the rotor loads by only using the primary flight controls. In fact, this approach only considers a control input bandwidth significantly lower than the main rotor angular speed, differently to what is done in HHC. Although this is less powerful approach than HHC since it does not alleviate the (periodic) trim loads, it could readily be implemented on AFCS of existing aircraft as it does not require high bandwidth actuators. It could thus constitute a shorter term and

less expensive alternative to HHC.

Further, all the previously mentioned techniques concentrated on extracting a LTP systems from physics-based models via numerical schemes. However, very few studies focused on experimentally characterizing LTP systems. In 2004, Verdult, Lovera, and Verhaegen identified an LTP system of the rotor dynamics alone from simulated experiments [32]. Surprisingly, no studies actually concentrated on identifying an LTP systems of the coupled rotor and rigid body dynamics from flight-test data. This is a fundamental step toward the implementation of HHC/IBC/OBC in industry, where manufacturers design and validate their control systems using models obtained from flight-test data.

1.2.2 Carefree Maneuvering

A 1988 joint study between the British Defence Research Agnecy (DRA) and Westland Helicopters [33] revealed that following a 70 UK military helicopter pilots survey, 75 % estimated a large benefit on mission performance and workload if the need to monitor torque limits could be removed. Given the result of the survey DRA and Westland Helicopters conducted a simulation study to understand the pilots' preference over a possible carefree maneuvering system. Tactile warning were found to be the most promising solution to indirect carefree maneuvering as they were considered good "attention getters" by the pilots. Further, the study investigated direct carefree maneuvering in the form of a torque command response mode. Even though this proved to protect the limits well, the potential conflict between handling qualities performance and good limit protection required further investigation.

Howitt continued the investigations at DRA and in 1995 he proposed a carefree maneuvering system that acted on the heave axis [34]. An adaptive control system mode which blends between collective blade pitch command, torque command, and rotorspeed command as a function of collective position was implemented. The

control law effectively enabled the pilot to command the full range of available performance up to the maximum transient limits in a safe and predictable manner. Control modes designed specifically to protect flight envelope limits proved beneficial in reducing task time and pilot workload.

The complex limit envelopes that constrain helicopter operations called for more sophisticated and precise limit detection systems, focusing the interest on neural networks. The first attempt to a neural network-based limit detection system was carried on by Menon et al. [35] and published in 1996. The limit detection system generated rotorcraft limit avoidance data using on-board measurements and demonstrated the feasibility of synthesizing a limit detection neural network for rotorcraft. Even though the proposed neural network architecture proved to be highly effective in generating the limit data, the limit variables and neural network architecture needed to be further refined before being employed in manned simulations or flight tests.

A similar approach that used a hybrid neural network/fuzzy logic system was proposed by Mulgund et al. [36] in the same year. The fuzzy logic algorithms characterized the rotorcraft's flight condition with respect to the flight limits, and provided a continuous measure of limit exceedance. This approach offered more flexibility than a binary classification of limit exceedance, since a continuous measure of exceedance with a specific threshold can warn of impeding exceedance. Simulation results showed that the blending logic was able to effect protection on airspeed, load factor, and attitude limits, proving the feasibility of the hybrid approach.

In the successive years, the late 1990's, the use of neural networks as means to predict flight envelope limits and achieve carefree maneuvering was extensively studied by Horn, Calise, and Prasad at Georgia Institute of Technology [37–39]. Neural networks were used to control deflections which result in a flight envelope limit exceedance. This information was then used to provide tactile cueing through

variable force-feel controllers. The system was tested on XV-15 and V-22 real-time piloted simulations. The results showed the capability of the system to handle multiple envelope limits and enabling pilots to maneuver along limit boundaries without exceeding the limits, effectively expanding the safe maneuvering envelope of the aircraft.

Yavrucuk continued Horn's research and proposed a novel technique for predicting limit parameter values and calculating the corresponding rotorcraft control margins [40,41]. The approach used an observer-type adaptive neural network loop for the estimation of the correct rotorcraft model. The estimated model is then used in an adaptive neural network loop to predict the quasi-steady response of the limit parameters and the respective control margins. Advantages associated with this method lie in not having to train the neural network and only needing standard sensor measurements for the adaptation.

A 2002 cooperative project between Sikorsky Aircraft Corporation and Pennsylvania State University [42] resulted in the development of a collective axis cueing system that cued the pilot with a variety of envelope limits associated with the engine and drive systems. The collective cueing system led to a significant reduction in pilot workload, a decrease in time required to conduct a specific task, and improved task accuracy for aggressive maneuvers.

Sahani and Horn's continued research on rotorcraft limit detection and avoidance at Pennsylvania State University resulted in multiple publications over the 2000's [6, 7, 9]. An envelope protection system for rotorcraft was integrated with full-envelope guidance and control using an inner loop / outer loop architecture. This approach eliminated the problems associated with saturation limits in the feedback path.

The entirety of these past methods were based on proxy models, which are simplistic and not always accurate, or stochastic methods (neural networks, fuzzy logic systems), which are generally not accepted in the aircraft certification process. This

study shows how LTP systems constitute a viable and computationally-effective way to predict rotor loads, and thus structural limits. Linear Time-Periodic systems, unlike neural networks or fuzzy logic systems, benefit from a deterministic nature that makes them more suitable for an aircraft certification process. Further, this research shows how LTP systems can be readily derived from physics-based models via linearization schemes or identified from flight test data. This way, previous work limitations such as the reliance on non-physics-based models and curve fits to approximate rotor loads are lifted.

1.2.3 Load Alleviation Control

The late 1980's saw the first applications of load alleviation control toward rotorcraft, with Miller et al. [11, 43] proposing a structural load limiting control law for a V-22 Osprey. A weighted least-squares eigenstructure assignment technique and a balanced singular value Linear Quadratic Gaussian with Loop Transfer Recovery (LQG/LTR) technique were applied to alleviate rotor yoke chord loads. Load alleviation was effectively achieved by reducing the precession generated rotor aerodynamic moments while allowing the pilot exploit the maneuverability and agility of the tiltrotor configuration. The study concluded that load alleviation considerations impose additional criteria on the control system design process to the traditional handling qualities requirements.

The load limiting control law development for the V-22 tiltrotor was continued by King et al. [44] in the successive years. Control laws were extended to limit trim rotor flapping, transient flapping in helicopter mode, transient driveshaft torques, and nacelle conversion actuator and vertical downstop loads, while maintaining Level 1 handling qualities. It was shown that for a rotorcraft with isolated structural loads such as the V-22, load limiting control laws represented a feasible approach to providing full structural load protection.

In 2002 Horn first developed a rotor state feedback (RSF) to achieve structural

load limiting [45]. The RSF controller was found to be effective for constraining hub moments to ensure structural load limits are not violated when using high bandwidth control. Further, the RSF controller provided an improved tracking performance when compared to the baseline controller, contrary to other high bandwidth control techniques.

Ultimately, load alleviation control is used not only to ensure the rotorcraft and its components operate within their structural limits, but also to achieve damage mitigation and extend component life.

Although successful, the above techniques achieved load alleviation by means of standard linear system theory that does not account for the higher-harmonic content of the structural loads in the control design. This study extends the harmonic decomposition methodology to enable optimization of primary flight control laws based on high-order LTI systems representative of the higher-harmonics of the rotor loads. The use of high-order LTI models is used to derive correlations of the controlled aircraft states to main rotor vibratory loads directly from the linearized physics-based model.

1.2.4 Damage Mitigation Control

The birth of damage mitigation control is motivated by the need of an interdisciplinary research that considers the handling qualities performance of the rotorcraft as well as the life of its structural components.

In the early 1990's Rozak [46] takes a first step towards the development of a damage mitigation system that extends service life of critical components resulting in the reduction of overall maintenance and operational costs. Specifically, different robust control system structures were implemented and tested in simulations to understand which would provide the best handling qualities. The flexible blade model used in the simulations was then coupled with a continuous-time damage model to measure the changes in critical rotor component fatigue life as a function

of achievable control system bandwidth.

A decade later Bridges et al. [8,47] developed a DMC controller that regulates rotor speed, vertical speed, and pitch attitude on a military helicopter while minimizing damage to the main rotor transmission and maintaining Level 1 handling qualities. The controller effectively achieved damage mitigation by scheduling the LQR gains and command model of the longitudinal and vertical axes with a damage reduction parameter. The damage reduction parameter was represented by the length of a crack in the main bevel pinion of the helicopter transmission. The study showed that the handling qualities deteriorated with increasing damage mitigation. Although proving success in reducing crack growth rate when compared to the baseline controller, the damage mitigation controller showed a trade-off between damage mitigation and performance.

The advancements in probabilistic robust control of rotorcraft carried on by Horn and Tolani et al. [48,49] paved the way to a more sophisticated approach to DMC that used hierarchical control [50]. The control system that was proposed consisted of a two-tier hierarchical architecture. The upper-tier monitored the system for any anomalous behavior. The lower tier was designed using a combination of probabilistic robust control and damage mitigating control methodologies. By allowing different levels of risk under different flight conditions, the probabilistic robust control achieved the desired trade-off between stability, robustness, and nominal performance. Minimization of damage rate was achieved via DMC, improving health management and durability. Nonlinear simulations have demonstrated the benefit of the approach.

An in-the-loop structural model that provides feedback of component damage to the control system for gain adjustment was first proposed by Thaiss et al. [5]. The control system consisted of a dynamic inversion architecture coupled with an artificial neural network based damage model. Load limiting was accomplished by limiting the response of key parameters in the command model. Specifically,

constraints were imposed on the commanded values of parameters such as angular accelerations, angular rates, vertical acceleration, and vertical speed. All of these parameters were correlated with critical loads and damage rate. The method proved successful as the lifespan of specific rotor head structural components were substantially increased with minimal impact on the handling qualities.

A similar, quite simple, but nonetheless effective method was investigated by Caudle et al. [3, 51]. Using a dynamic inversion control architecture, damage reduction to certain main rotor components was achieved through state response limiting in the command filter. Limiters were implemented both in the roll and pitch axes command filters. Upper and lower bounds for the limiters were chosen by correlating the component loads and the state variables. The method proved to be of simple implementation and successful in extending the life of main rotor components. Here damage reduction was effectively achieved through load alleviation, limiting the load factor experienced by the rotorcraft.

The above techniques proved to mitigate structural loads but at the cost of a reduction in handling qualities. Further, the handling qualities that were considered were a small subset of the comprehensive set of handling qualities an aircraft needs to meet during the certification process. This study concentrates on reducing structural loads while guaranteeing that Level 1 handling qualities are preserved. A thorough analysis is conducted to better understand how both feed-forward and feedback compensation affect load alleviation and handling qualities.

1.2.5 Compound Rotorcraft Vibration Reduction

During initial flight test of the Lockheed AH-56A helicopter vibration level at high speeds were found to be totally unacceptable. Analytic and experimental efforts were undertaken to reduce vibration level to acceptable values. The methods incorporated to reduce such levels are published in [52] and constitute the first effort to alleviate vibratory loads on a compound helicopter. The study concluded

that control of vibrations around the pitch axis can be achieved by means of stabilizer settings. Further, test results showed an optimum collective blade angle for reduced vibrations. The blade angle was found to be relatively invariant at forward speed, making it possible for the plot to fly at one given collective angle. Finally, and most importantly, flight test showed that vibration levels changed with different trim settings.

Sekula et al. [53] analyzed how the introduction of auxiliary lift surfaces and and propulsion, individually, as well as in combination, affected the vibration levels in trim. The research effort showed that auxiliary lift alone produces relatively small reductions in vibrations; however, significant vibration reduction was achieved through auxiliary propulsion alone. It was concluded that a combination of lift and propulsion was most efficient and reduced vibration levels by over 90 %.

A study by Gandhi et al. [54] concentrated on reduction in helicopter rotor hub vibratory loads in trim by the introduction of auxiliary pitching and rolling moments in the fixed system. The auxiliary moments were generated by variation in pitch of the right and left halves of the horizontal stabilizer, allowing changes in vehicle attitude and rotor pitch control inputs, such that vibrations be minimized. Simulation studies that used a BO-105 type helicopter concluded that a nose-down auxiliary pitching moment and a roll-left auxiliary rolling moment reduced the in-plane vibratory hub loads by 20-30 % when used individually and by up to 90 % when combined.

Geiger was the first to consider the problem of flight control optimization on a compound rotorcraft with redundant control effectors both in trim and maneuvering flight [4]. A number of trim cases for all permutations of a discrete set of auxiliary controls were calculated and the optimal control selection that minimized vibratory loads and total power required was selected. The optimal trim schedule was then used in a full authority fly-by-wire flight controller. The compound rotorcraft flying with the optimal schedule showed reduced vibration and power levels

when compared to the baseline aircraft with no control redundancy. In particular, structural loads were reduced when pitch control is transferred from longitudinal cyclic to the moving horizontal stabilizer.

The above studies focused on the optimization of redundant control allocation to minimize vibratory loads in trim. However, very little to none published research exists on redundant control allocation to minimize vibratory loads in maneuvering flight. This study concentrates on exploiting the use of redundant control surfaces to actively reduce unsteady rotor loads. Further, the impact of redundant control allocation on handling qualities is assessed.

1.3 Contributions

The contributions of this study are summarized as follows:

1. This study uses Harmonic Decomposition to obtain reduced order models that capture the influence of the 0^{th} harmonic of the rigid-body, rotor flapping states, and input on the rotor loads. These models are used to synthesize a controller that minimizes the rotor loads by only using the primary flight controls. In fact, this approach only considers a control input bandwidth significantly lower than the main rotor angular speed, differently to what is done in HHC. Although this is less powerful approach than HHC since it does not alleviate the (periodic) trim loads, it could readily be implemented on AFCS of existing aircraft as it does not require high bandwidth actuators. It could thus constitute a shorter term and less expensive alternative to HHC.

2. Previous studies almost exclusively concentrated on extracting a LTP systems from physics-based models via numerical schemes. Very few studies focused on experimentally characterizing LTP systems representative of the rotor dynamics alone from simulated experiments. No studies actually concentrated on identifying an LTP systems of the coupled rotor and rigid body

dynamics from flight-test data. The identification of LTP systems representative of the coupled rotor and rigid body dynamics from flight-test data is a fundamental step toward the implementation of HHC/IBC/OBC in industry, where manufacturers design and validate their control systems using models obtained from flight-test data.

3. Past methods for Carefree Maneuvering were based on either proxy models or stochastic methods. This study shows how LTP systems constitute a viable and computationally-effective way to predict rotor loads, and thus structural limits. Linear Time-Periodic systems, unlike neural networks or fuzzy logic systems, benefit from a deterministic nature that makes them more suitable for an aircraft certification process. Further, this research shows how LTP systems can be readily derived from physics-based models via linearization schemes or identified from flight test data. This way, previous work limitations such as the reliance on non-physics-based models and curve fits to approximate rotor loads are lifted.

4. Load alleviation have historically been achieved by means of standard linear system theory that does not account for the higher-harmonic content of the structural loads in the control design. This study extends the harmonic decomposition methodology to enable optimization of primary flight control laws based on high-order LTI systems representative of the higher-harmonics of the rotor loads. The use of high-order LTI models is used to derive correlations of the controlled aircraft states to main rotor vibratory loads directly from the linearized physics-based model.

5. Previous damage mitigation control laws proved to mitigate structural loads but at the cost of a reduction in handling qualities. Further, the handling qualities that were considered were a small subset of the comprehensive set of handling qualities an aircraft needs to meet during the certification process.

This study concentrates on reducing structural loads while guaranteeing that Level 1 handling qualities are preserved. A thorough analysis is conducted to better understand how both feed-forward and feedback compensation affect load alleviation and handling qualities.

6. Past research on compound rotorcraft focused on the optimization of redundant control allocation to minimize vibratory loads in trim. However, very little to none published research exists on redundant control allocation to minimize vibratory loads in maneuvering flight. This study concentrates on exploiting the use of redundant control surfaces to actively reduce unsteady rotor loads. Further, the impact of redundant control allocation on handling qualities is assessed.

1.4 Objectives

The objective of this research is to extend the harmonic decomposition methodology to the design of load alleviation control laws that operate solely through primary flight control actuation while having no negative impact on the handling qualities. The methods will be applied to both conventional and compound rotorcraft. Further, since linear time-periodic systems were historically obtained from simulations through linearization schemes, their applications is confined to research studies. For this reason, linear time-periodic system derivation from flight test data is a fundamental step towards their application towards flight control system design in real-world applications. This adds to the objectives of the study. The expected results are summarized as follows:

1. Use the harmonic decomposition methodology to derive reduced-order models that accurately predict the higher-harmonics of the rotor loads and can be used towards control system design.

2. Use the reduced-order models that predict the higher-harmonics of the rotor loads to optimize flight control laws that operate solely through the primary flight, minimize rotor loads, and concurrently meet a comprehensive set of desired handling qualities.

3. In the context of a model-following control law, assess the impact that both the feed-forward and feedback paths have on load alleviation and handling qualities.

4. Analyze the use of redundant control surfaces for the case of a compound rotorcraft. Specifically, study how redundant control allocation techniques affect load alleviation and handling qualities.

5. Demonstrate the effectiveness of the load alleviation control strategies that are developed in simulation studies.

6. Develop a methodology to identify Linear Time-Periodic systems representative of the coupled rigid body / rotor dynamics of a rotorcraft from flight test data.

Chapter 2

Linear Models Extraction and Validation

2.1 Linear Models Extraction

2.1.1 FLIGHTLAB® Software

FLIGHTLAB® is an aircraft development and analysis program developed by Advance Rotorcraft Technologies, Inc. (ART) that allows users to produce highly detailed aircraft models from a library of modeling components using a graphical user interface [55]. Once the model is created, it can be analyzed using the built in Scope language. Analysis and simulation can be accomplished with predefined script files that are called through a point-and-click interface. FLIGHTLAB® has complex modeling capabilities for rotorcraft, making it particularly useful for rotorcraft analysis applications. The Control System Graphical Editor (CSGE), another package within FLIGHTLAB®, allows the user to create a block diagram controller for use with an aircraft model.

Figure 2.1: UH-60 Black Hawk (www.lockheedmartin.com).

2.1.2 Nonlinear Models

This investigation uses a FLIGHTLAB® model of a notional conventional helicopter representative of a UH-60, as shown in Fig. 2.1. To accurately model the rotor loads, the model includes flexible blades with representative in-plane, out-of-plane, and torsional bending modes, in addition to the rigid blade flap and lag dynamics. Complete nonlinear aerodynamic look-up tables are used for airframe and rotor blade aerodynamic coefficients. The inflow dynamics are described by a six-state Peters-He inflow model. Further details on the helicopter model are found in [3].

The second model is a notional compound rotorcraft representative of an H-60 with the addition of a wing with flaperons, and a moving horizontal tail (stabilator). The wing is similar to the X-49A wing shown in Fig. 2.2. The flaperons and stabilator are used as redundant control surfaces. The model is based on the notional conventional helicopter model.

One limitation of the FLIGHTLAB® models is the inability to predict dynamic stall and thus the typically strong vibratory loads associated to it. The onset of dynamic stall, however, occurs at very high speeds. TFor this reason, this research

Figure 2.2: X-49A Speed Hawk (www.airworld.tistory.com).

concentrates on moderately high speeds - 120 kts - where the N_b/rev component of the rotor loads is significant but the rotor loads induced by dynamic stall are negligible.

2.1.3 Linear Time-Periodic Model

The following procedure is similar to the one in Ref. [21] but focuses on a first order formulation of a Linear Time-Periodic (LTP) system. Consider a nonlinear system:

$$\dot{\mathbf{x}} = \mathbf{f}(\mathbf{x}, \dot{\mathbf{x}}, \mathbf{u}) \tag{2.1a}$$

$$\mathbf{y} = \mathbf{g}(\mathbf{x}, \dot{\mathbf{x}}, \mathbf{u}) \tag{2.1b}$$

where:

$\mathbf{x}$ is the state vector of dimension n,

$\mathbf{u}$ is the control vector of dimension m, and

$\mathbf{y}$ is the output vector of dimension l.

The unusual form of the nonlinear system is justified by the fact that the rotor state derivatives are dependent on the fuselage state derivatives. This causes f to be function not only of state and control vectors, but also of the state derivative

vector. Considering the case of small disturbances:

$$\mathbf{x} = \mathbf{x}_e(\psi) + \boldsymbol{\Delta}\mathbf{x} \tag{2.2a}$$

$$\mathbf{u} = \mathbf{u}_e(\psi) + \boldsymbol{\Delta}\mathbf{u} \tag{2.2b}$$

$$\mathbf{y} = \mathbf{y}_e(\psi) + \boldsymbol{\Delta}\mathbf{y} \tag{2.2c}$$

where ψ is the azimuth angle of a reference main rotor blade, and $\mathbf{x}_e(\psi)$, $\mathbf{y}_e(\psi)$, and $\mathbf{u}_e(\psi)$ define a periodic equilibrium condition:

$$\dot{\mathbf{x}}_e = \mathbf{f}\left(\mathbf{x}_e, \dot{\mathbf{x}}_e, \mathbf{u}_e\right) \tag{2.3a}$$

$$\mathbf{y}_e = \mathbf{g}\left(\mathbf{x}_e, \dot{\mathbf{x}}_e, \mathbf{u}_e\right) \tag{2.3b}$$

A Taylor series expansion is performed on the state vector time derivative. After neglecting the terms of second order and higher, the following equation is derived:

$$\begin{aligned}\mathbf{f}\left(\mathbf{x}_e + \boldsymbol{\Delta}\mathbf{x}, \dot{\mathbf{x}}_e + \boldsymbol{\Delta}\dot{\mathbf{x}}, \mathbf{u}_e + \boldsymbol{\Delta}\mathbf{u}\right) &= \mathbf{f}\left(\mathbf{x}_e, \dot{\mathbf{x}}_e, \mathbf{u}_e\right) \\ &\quad + \mathbf{F}(\psi)\boldsymbol{\Delta}\mathbf{x} + \mathbf{K}(\psi)\boldsymbol{\Delta}\dot{\mathbf{x}} + \mathbf{G}(\psi)\boldsymbol{\Delta}\mathbf{u}\end{aligned} \tag{2.4}$$

where

$$\mathbf{F}(\psi) = \left.\frac{\partial \mathbf{f}\left(\mathbf{x}, \dot{\mathbf{x}}, \mathbf{u}\right)}{\partial \mathbf{u}}\right|_{\mathbf{x}_e, \dot{\mathbf{x}}_e, \mathbf{u}_e} \tag{2.5a}$$

$$\mathbf{K}(\psi) = \left.\frac{\partial \mathbf{f}\left(\mathbf{x}, \dot{\mathbf{x}}, \mathbf{u}\right)}{\partial \dot{\mathbf{x}}}\right|_{\mathbf{x}_e, \dot{\mathbf{x}}_e, \mathbf{u}_e} \tag{2.5b}$$

$$\mathbf{G}(\psi) = \left.\frac{\partial \mathbf{f}\left(\mathbf{x}, \dot{\mathbf{x}}, \mathbf{u}\right)}{\partial \mathbf{u}}\right|_{\mathbf{x}_e, \dot{\mathbf{x}}_e, \mathbf{u}_e} \tag{2.5c}$$

With a few steps of algebraic manipulation, a differential equation for the state

perturbation from the periodic equilibrium is derived:

$$\boldsymbol{\Delta}\dot{\mathbf{x}} = \hat{\mathbf{F}}(\psi)\boldsymbol{\Delta}\mathbf{x} + \hat{\mathbf{G}}(\psi)\boldsymbol{\Delta}\mathbf{u} \tag{2.6}$$

where:

$$\hat{\mathbf{F}}(\psi) = (\mathbf{I} - \mathbf{K})^{-1}\,\mathbf{F} \tag{2.7a}$$

$$\hat{\mathbf{G}}(\psi) = (\mathbf{I} - \mathbf{K})^{-1}\,\mathbf{G} \tag{2.7b}$$

Similarly, a Taylor series expansion is performed on the output equation. After neglecting the terms of second order and higher, the following equation is derived:

$$\begin{aligned}\mathbf{g}\left(\mathbf{x}_e + \boldsymbol{\Delta}\mathbf{x}, \dot{\mathbf{x}}_e + \boldsymbol{\Delta}\dot{\mathbf{x}}, \mathbf{u}_e + \boldsymbol{\Delta}\mathbf{u}\right) = \mathbf{g}\left(\mathbf{x}_e, \dot{\mathbf{x}}_e, \mathbf{u}_e\right) \\ + \mathbf{P}(\psi)\boldsymbol{\Delta}\mathbf{x} + \mathbf{Q}(\psi)\boldsymbol{\Delta}\dot{\mathbf{x}} + \mathbf{R}(\psi)\boldsymbol{\Delta}\mathbf{u}\end{aligned} \tag{2.8}$$

where

$$\mathbf{P}(\psi) = \left.\frac{\partial \mathbf{g}\left(\mathbf{x}, \dot{\mathbf{x}}, \mathbf{u}\right)}{\partial \mathbf{u}}\right|_{\mathbf{x}_e, \dot{\mathbf{x}}_e, \mathbf{u}_e} \tag{2.9a}$$

$$\mathbf{Q}(\psi) = \left.\frac{\partial \mathbf{g}\left(\mathbf{x}, \dot{\mathbf{x}}, \mathbf{u}\right)}{\partial \dot{\mathbf{x}}}\right|_{\mathbf{x}_e, \dot{\mathbf{x}}_e, \mathbf{u}_e} \tag{2.9b}$$

$$\mathbf{R}(\psi) = \left.\frac{\partial \mathbf{g}\left(\mathbf{x}, \dot{\mathbf{x}}, \mathbf{u}\right)}{\partial \mathbf{u}}\right|_{\mathbf{x}_e, \dot{\mathbf{x}}_e, \mathbf{u}_e} \tag{2.9c}$$

After substituting Eq. 2.6 in Eq. 2.8 and carrying on the calculations, an equation for the output perturbation from the periodic equilibrium is derived:

$$\boldsymbol{\Delta}\mathbf{y} = \hat{\mathbf{P}}(\psi)\boldsymbol{\Delta}\mathbf{x} + \hat{\mathbf{R}}(\psi)\boldsymbol{\Delta}\mathbf{u} \tag{2.10}$$

where

$$\hat{\mathbf{P}}(\psi) = \mathbf{P} + \mathbf{Q}\hat{\mathbf{F}} \tag{2.11a}$$

$$\hat{\mathbf{R}}(\psi) = \mathbf{R} + \mathbf{Q}\hat{\mathbf{G}} \tag{2.11b}$$

Equations 2.6 and 2.10 constitute a first-order formulation of an LTP system representative of the periodic rotorcraft dynamics.

In practice, the nonlinear FLIGHTLAB® models are first trimmed at a desired flight condition (120 kts level flight). Then a nonlinear simulation is run until the azimuthal position of a reference blade reaches $\psi = 0°$. Finally, the model is linearized at incremental azimuth positions over one rotor revolution. The flight condition is 120 kts level flight and the time step is $\Delta\psi = 0.5°$, which gives a total of 720 azimuthal positions.

From now on, the notation is simplified by dropping the Δ in front of the linearized variables. The reader should remember, however, that the linear systems describe perturbations from a periodic equilibrium. The state and output vectors of the LTP system are:

$$\mathbf{x}^T = \begin{bmatrix} \mathbf{x}_{\mathrm{RB}}^T & \mathbf{x}_{\mathrm{R}}^T \end{bmatrix} \tag{2.12a}$$

$$\mathbf{y}^T = \begin{bmatrix} \mathbf{x}_{\mathrm{RB}}^T & \mathrm{PLL} \end{bmatrix} \tag{2.12b}$$

where:

$\mathbf{x}_{\mathrm{RB}}$ are the rigid-body states,

$\mathbf{x}_{\mathrm{R}}$ are the higher-order rotor states, and

PLL is the longitudinal load of a reference pitch link.

The rigid-body state vector is given by, in order, the body velocities u, v, w, the body angular rates p, q, r, and the Euler angles ϕ, θ, ψ (note that ψ here is the yaw attitude and not the main rotor azimuth). The rotor states include inflow, rigid flap, lag and torsion in multi-blade coordinates (MBC), the slowest 11 bending modes also in MBC, and the time derivatives of all the variables in MBC.

The input vector for the conventional helicopter model is:

$$\mathbf{u}^T = \begin{bmatrix} \delta_{\text{lat}} & \delta_{\text{lon}} & \delta_{\text{ped}} \end{bmatrix} \tag{2.13}$$

where:

δ_{lat} is the lateral stick,

δ_{lon} is the longitudinal stick, and

δ_{ped} is the pedal.

The collective stick is omitted as it is not used for the subsequent control design. For the conventional helicopter the system has a total of $n = 116$ states, $m = 10$ outputs, and $l = 3$ inputs. The input vector for the compound rotorcraft model is:

$$\mathbf{u}^T = \begin{bmatrix} \delta_{\text{lat}} & \delta_{\text{lon}} & \delta_{\text{ped}} & \delta_{\text{sym}} & \delta_{\text{dif}} & \delta_{\text{stb}} \end{bmatrix} \tag{2.14}$$

where:

δ_{sym} is the symmetric motion of the flaperons,

δ_{dif} is the differential motion of the flaperons, and

δ_{stb} is the motion of the stabilator.

For the compound rotorcraft the system has a total of $n = 120$ states, $m = 10$ outputs, and $l = 6$ inputs.

2.1.4 Linear Time-Invariant Model

Consider a general first-order formulation of an LTP system:

$$\dot{\mathbf{x}} = \mathbf{F}(\psi)\mathbf{x} + \mathbf{G}(\psi)\mathbf{u} \tag{2.15a}$$

$$\mathbf{y} = \mathbf{P}(\psi)\mathbf{x} + \mathbf{R}(\psi)\mathbf{u} \tag{2.15b}$$

It is convenient to note that ψ is equivalent to non-dimensional time, which can be related to dimensional time via the following relation: $\psi = \Omega t$, where Ω the main rotor angular speed in rad/s, and t is the dimensional time in seconds. Each coefficient matrix is periodic with a fundamental period of T seconds, which corresponds to 2π radians or one rotor revolution:

$$\mathbf{F}(\psi) = \mathbf{F}(\psi + \Omega_f T) \tag{2.16a}$$

$$\mathbf{G}(\psi) = \mathbf{G}(\psi + \Omega_f T) \tag{2.16b}$$

$$\mathbf{P}(\psi) = \mathbf{P}(\psi + \Omega_f T) \tag{2.16c}$$

$$\mathbf{R}(\psi) = \mathbf{R}(\psi + \Omega_f T) \tag{2.16d}$$

for all ψ. For rotorcraft, the fundamental frequency can be the main rotor angular speed $\Omega_f = \Omega$ (corresponds to 1/rev), or it can be any multiple of the number of blades times the rotor speed $\Omega_f = kN_b\Omega$, $k = 1, 2, 3, ...$ (corresponds to multiples of $\mathrm{N_b}$/rev).

When the fundamental frequency of oscillation Ω_f is known, the state, input, and output of the LTP system can be decomposed into a finite number of harmonics via Fourier analysis:

$$\mathbf{x} = \mathbf{x}_0 + \sum_{n=1}^{N} \left(\mathbf{x}_{nc} \cos n\psi + \mathbf{x}_{ns} \sin n\psi \right) \tag{2.17a}$$

$$\mathbf{u} = \mathbf{u}_0 \tag{2.17b}$$

$$\mathbf{y} = \mathbf{y}_0 + \sum_{l=1}^{L} \left(\mathbf{y}_{lc} \cos l\psi + \mathbf{y}_{ls} \sin l\psi \right) \tag{2.17c}$$

Note that only the 0^{th} harmonic of the input vector is retained. This is because the present study considers solely primary flight control actuation, thus disregarding any sort of higher-harmonic control. In fact, the desired bandwidth of the control

signal is significantly less than the main rotor angular speed.

Differentiating the state equation with respect to dimensional time leads to:

$$\dot{\mathbf{x}} = \dot{\mathbf{x}}_0 + \sum_{n=1}^{N} \left(\mathbf{x}'_{nc} \cos n\psi + \mathbf{x}'_{ns} \sin n\psi \right) \tag{2.18}$$

where:

$$\mathbf{x}'_{nc} = \dot{\mathbf{x}}_{nc} + n\Omega \mathbf{x}_{ns} \tag{2.19a}$$

$$\mathbf{x}'_{ns} = \dot{\mathbf{x}}_{ns} - n\Omega \mathbf{x}_{nc} \tag{2.19b}$$

By substituting Eqs. 2.50 and 2.18 into Eq. 2.6 results in:

$$\dot{\mathbf{x}}_0 + \sum_{n=1}^{N} \mathbf{x}'_{nc} \cos n\psi + \mathbf{x}'_{ns} \sin n\psi = \mathbf{F}(\psi) \left[\mathbf{x}_0 + \sum_{n=1}^{N} \left(\mathbf{x}_{nc} \cos n\psi + \mathbf{x}_{ns} \sin n\psi \right) \right] + \mathbf{G}(\psi)\mathbf{u}_0 \tag{2.20}$$

Equations for the individual harmonic components of $\mathbf{x}$ are found by multiplying Eq. 2.20 by $\cos i\psi$ or $\sin i\psi$ and by integrating over one rotor revolution:

$$\dot{\mathbf{x}}_0 = \frac{1}{2\pi} \int_0^{2\pi} \left\{ \mathbf{F}(\psi) \left[\mathbf{x}_0 + \sum_{n=1}^{N} \left(\mathbf{x}_{nc} \cos n\psi + \mathbf{x}_{ns} \sin n\psi \right) \right] + \mathbf{G}(\psi)\mathbf{u}_0 \right\} d\psi \tag{2.21}$$

$$\mathbf{x}'_{ic} = \frac{1}{\pi} \int_0^{2\pi} \left\{ \mathbf{F}(\psi) \left[\mathbf{x}_0 + \sum_{n=1}^{N} \left(\mathbf{x}_{nc} \cos n\psi + \mathbf{x}_{ns} \sin n\psi \right) \right] + \mathbf{G}(\psi)\mathbf{u}_0 \right\} \cos i\psi d\psi \tag{2.22}$$

$$\mathbf{x}'_{is} = \frac{1}{\pi}\int_0^{2\pi}\left\{\mathbf{F}(\psi)\left[\mathbf{x}_0 + \sum_{n=1}^{N}\left(\mathbf{x}_{nc}\cos n\psi + \mathbf{x}_{ns}\sin n\psi\right)\right] + \mathbf{G}(\psi)\mathbf{u}_0\right\}\sin i\psi d\psi \quad (2.23)$$

By introducing the following notation:

$$\mathbf{F}^{nc}(\psi) = \mathbf{F}(\psi)\cos n\psi \quad (2.24a)$$

$$\mathbf{F}^{ns}(\psi) = \mathbf{F}(\psi)\sin n\psi \quad (2.24b)$$

and by substituting in Eqs. 2.21, 2.22, 2.23, yields:

$$\dot{\mathbf{x}}_0 = \frac{1}{2\pi}\int_0^{2\pi}\left\{\left[\mathbf{F}(\psi)\mathbf{x}_0 + \sum_{n=1}^{N}\left(\mathbf{F}^{nc}(\psi)\mathbf{x}_{nc} + \mathbf{F}^{ns}(\psi)\mathbf{x}_{ns}\right)\right] + \mathbf{G}(\psi)\mathbf{u}_0\right\}d\psi \quad (2.25)$$

$$\dot{\mathbf{x}}_{ic} = -i\Omega\mathbf{x}_{1s}\frac{1}{\pi}\int_0^{2\pi}\left\{\left[\mathbf{F}(\psi)\mathbf{x}_0 + \sum_{n=1}^{N}\left(\mathbf{F}^{nc}(\psi)\mathbf{x}_{nc} + \mathbf{F}^{ns}(\psi)\mathbf{x}_{ns}\right)\right] + \mathbf{G}(\psi)\mathbf{u}_0\right\}\cos i\psi d\psi \quad (2.26)$$

$$\dot{\mathbf{x}}_{is} = i\Omega\mathbf{x}_{1c}\frac{1}{\pi}\int_0^{2\pi}\left\{\left[\mathbf{F}(\psi)\mathbf{x}_0 + \sum_{n=1}^{N}\left(\mathbf{F}^{nc}(\psi)\mathbf{x}_{nc} + \mathbf{F}^{ns}(\psi)\mathbf{x}_{ns}\right)\right] + \mathbf{G}(\psi)\mathbf{u}_0\right\}\sin i\psi d\psi \quad (2.27)$$

By defining the following operators:

$$\mathbf{H}_{0M} = \frac{1}{2\pi}\int_0^{2\pi}\mathbf{M}(\psi)d\psi \quad (2.28a)$$

$$\mathbf{H}_{icM} = \frac{1}{\pi}\int_0^{2\pi}\mathbf{M}(\psi)\cos i\psi d\psi \quad (2.28b)$$

$$\mathbf{H}_{isM} = \frac{1}{\pi}\int_0^{2\pi} \mathbf{M}(\psi)\sin i\psi d\psi \tag{2.28c}$$

$$\tag{2.28d}$$

one can re-write Eqs. 2.25, 2.26 and 2.27 as:

$$\dot{\mathbf{x}}_0 = \mathbf{H}_{0F}\mathbf{x}_0 + \sum_{n=1}^{N}\left(\mathbf{H}_{0F^{nc}}\mathbf{x}_{nc} + \mathbf{H}_{0F^{ns}}\mathbf{x}_{ns}\right) + \mathbf{H}_{0G}\mathbf{u}_0 \tag{2.29}$$

$$\dot{\mathbf{x}}_{ic} = \mathbf{H}_{icF}\mathbf{x}_0 + \sum_{n=1}^{N}\left(\mathbf{H}_{icF^{nc}}\mathbf{x}_{nc} + \mathbf{H}_{icF^{ns}}\mathbf{x}_{ns}\right) + \mathbf{H}_{icG}\mathbf{u}_0 - i\Omega\mathbf{x}_{is} \tag{2.30}$$

$$\dot{\mathbf{x}}_{is} = \mathbf{H}_{isF}\mathbf{x}_0 + \sum_{n=1}^{N}\left(\mathbf{H}_{isF^{nc}}\mathbf{x}_{nc} + \mathbf{H}_{isF^{ns}}\mathbf{x}_{ns}\right) + \mathbf{H}_{isG}\mathbf{u}_0 + i\Omega\mathbf{x}_{ic} \tag{2.31}$$

By substituting Eq. 2.50 into the output equation (Eq. 2.10) one obtains:

$$\mathbf{y}_0 + \sum_{l=1}^{L}\left(\mathbf{y}_{lc}\cos l\psi + \mathbf{y}_{ls}\sin l\psi\right) = \mathbf{P}(\psi)\left[\mathbf{x}_0 + \sum_{n=1}^{N}\left(\mathbf{x}_{nc}\cos n\psi + \mathbf{x}_{ns}\sin n\psi\right)\right] + \mathbf{R}(\psi)\mathbf{u}_0 \tag{2.32}$$

Equation 2.32 is multiplied by $\cos j\psi$ or $\sin j\psi$ and integrated over one rotor revolution, resulting in the following relations:

$$\mathbf{y}_0 = \frac{1}{2\pi}\int_0^{2\pi}\left\{\mathbf{P}(\psi)\left[\mathbf{x}_0 + \sum_{n=1}^{N}\left(\mathbf{x}_{nc}\cos n\psi + \mathbf{x}_{ns}\sin n\psi\right)\right] + \mathbf{R}(\psi)\mathbf{u}_0\right\}d\psi \tag{2.33}$$

$$\mathbf{y}_{lc} = \frac{1}{\pi}\int_0^{2\pi}\left\{\mathbf{P}(\psi)\left[\mathbf{x}_0 + \sum_{n=1}^{N}\left(\mathbf{x}_{nc}\cos n\psi + \mathbf{x}_{ns}\sin n\psi\right)\right] + \mathbf{R}(\psi)\mathbf{u}_0\right\}\cos l\psi d\psi \tag{2.34}$$

$$\mathbf{y}_{ls} = \frac{1}{\pi}\int_0^{2\pi} \left\{ \mathbf{P}(\psi) \left[\mathbf{x}_0 + \sum_{n=1}^{N} \left(\mathbf{x}_{nc} \cos n\psi + \mathbf{x}_{ns} \sin n\psi \right) \right] + \mathbf{G}(\psi)\mathbf{u}_0 \right\} \sin l\psi d\psi \quad (2.35)$$

By using a similar notation as before and the **H** operator, one obtains:

$$\mathbf{y}_0 = \mathbf{H}_{0P}\mathbf{x}_0 + \sum_{n=1}^{N} \left(\mathbf{H}_{0P^{nc}}\mathbf{x}_{nc} + \mathbf{H}_{0P^{ns}}\mathbf{x}_{ns} \right) + \mathbf{H}_{0R}\mathbf{u}_0 \quad (2.36)$$

$$\mathbf{y}_{lc} = \mathbf{H}_{lcP}\mathbf{x}_0 + \sum_{n=1}^{N} \left(\mathbf{H}_{lcP^{nc}}\mathbf{x}_{nc} + \mathbf{H}_{lcP^{ns}}\mathbf{x}_{ns} \right) + \mathbf{H}_{lcR}\mathbf{u}_0 \quad (2.37)$$

$$\mathbf{y}_{is} = \mathbf{H}_{lsP}\mathbf{x}_0 + \sum_{n=1}^{N} \left(\mathbf{H}_{lsP^{nc}}\mathbf{x}_{nc} + \mathbf{H}_{lsP^{ns}}\mathbf{x}_{ns} \right) + \mathbf{H}_{lsR}\mathbf{u}_0 \quad (2.38)$$

Similarly to Ref. [25], the LTP system is transformed into an approximate higher-order Linear Time Invariant (LTI) system:

$$\mathbf{X} = \mathbf{A}\mathbf{X} + \mathbf{B}\mathbf{U} \quad (2.39a)$$

$$\mathbf{Y} = \mathbf{C}\mathbf{X} + \mathbf{D}\mathbf{U} \quad (2.39b)$$

where:

$$\mathbf{X}^T = \begin{bmatrix} \mathbf{x}_0^T & \mathbf{x}_{1c}^T & \mathbf{x}_{1s}^T & \dots \mathbf{x}_{Nc}^T & \mathbf{x}_{Ns}^T \end{bmatrix} \quad (2.40a)$$

$$\mathbf{U} = \mathbf{u}_0 \quad (2.40b)$$

$$\mathbf{Y}^T = \begin{bmatrix} \mathbf{y}_0^T & \mathbf{y}_{1c}^T & \mathbf{y}_{1s}^T & \dots \mathbf{y}_{Lc}^T & \mathbf{y}_{Ls}^T \end{bmatrix} \quad (2.40c)$$

are respectively the augmented state, control, and output vectors. The augmented

coefficient matrices are:

$$\mathbf{A} = \begin{bmatrix} \mathbf{H}_{0F} & \mathbf{H}_{0F^{1c}} & \mathbf{H}_{0F^{1s}} & \cdots & \mathbf{H}_{0F^{Nc}} & \mathbf{H}_{0F^{Ns}} \\ \mathbf{H}_{1cF} & \mathbf{H}_{1cF^{1s}} & -\Omega + \mathbf{H}_{1cF^{1s}} & \cdots & \mathbf{H}_{1cF^{Nc}} & \mathbf{H}_{1cF^{Ns}} \\ \mathbf{H}_{1sF} & \Omega + \mathbf{H}_{1sF^{1s}} & \mathbf{H}_{1sF^{1s}} & \cdots & \mathbf{H}_{1sF^{Nc}} & \mathbf{H}_{1sF^{Ns}} \\ \vdots & \vdots & \vdots & \ddots & \vdots & \vdots \\ \mathbf{H}_{NcF} & \mathbf{H}_{NcF^{1s}} & \mathbf{H}_{NcF^{1s}} & \cdots & \mathbf{H}_{NcF^{Nc}} & -N\Omega + \mathbf{H}_{NcF^{Ns}} \\ \mathbf{H}_{NsF} & \mathbf{H}_{NsF^{1s}} & \mathbf{H}_{NsF^{1s}} & \cdots & N\Omega + \mathbf{H}_{NsF^{Nc}} & \mathbf{H}_{NsF^{Ns}} \end{bmatrix} \tag{2.41}$$

$$\mathbf{B} = \begin{bmatrix} \mathbf{H}_{0G} \\ \mathbf{H}_{1cG} \\ \mathbf{H}_{1sG} \\ \vdots \\ \mathbf{H}_{NcG} \\ \mathbf{H}_{NsG} \end{bmatrix} \tag{2.42}$$

$$\mathbf{C} = \begin{bmatrix} \mathbf{H}_{0P} & \mathbf{H}_{0P^{1c}} & \mathbf{H}_{0P^{1s}} & \cdots & \mathbf{H}_{0F^{Nc}} & \mathbf{H}_{0F^{Ns}} \\ \mathbf{H}_{1cP} & \mathbf{H}_{1cP^{1c}} & \mathbf{H}_{1cP^{1s}} & \cdots & \mathbf{H}_{1cP^{Nc}} & \mathbf{H}_{1cP^{Ns}} \\ \mathbf{H}_{1sP} & \mathbf{H}_{1sP^{1c}} & \mathbf{H}_{1sP^{1s}} & \cdots & \mathbf{H}_{1sP^{Nc}} & \mathbf{H}_{1sP^{Ns}} \\ \vdots & \vdots & \vdots & \ddots & \vdots & \vdots \\ \mathbf{H}_{LcP} & \mathbf{H}_{LcF^{1c}} & \mathbf{H}_{LcF^{1s}} & \cdots & \mathbf{H}_{LcF^{Nc}} & \mathbf{H}_{LcF^{Ns}} \\ \mathbf{H}_{LsP} & \mathbf{H}_{LsF^{1c}} & \mathbf{H}_{LsF^{1s}} & \cdots & \mathbf{H}_{LsF^{Nc}} & \mathbf{H}_{LsF^{Ns}} \end{bmatrix} \tag{2.43}$$

$$\mathbf{D} = \begin{bmatrix} \mathbf{H}_{0R} \\ \mathbf{H}_{1cR} \\ \mathbf{H}_{1sR} \\ \vdots \\ \mathbf{H}_{LcR} \\ \mathbf{H}_{LsR} \end{bmatrix} \tag{2.44}$$

the state space matrices. The higher-order LTI model has $n(2N+1)$ states and

$l(2L+1)$ outputs.

2.1.5 Minimum Number of Harmonics to Retain

Consider an LTP system representative of the rotor flapping dynamics:

$$\dot{\mathbf{x}} = \mathbf{F}(\psi)\mathbf{x} \tag{2.45}$$

where the state matrix is periodic with respect to the main rotor azimuth angle ψ:

$$\mathbf{F}(\psi) = \mathbf{F}(\psi + 2\pi) \tag{2.46}$$

The state vector is composed by the Multi-Blade Coordinates (MBC) of a 4-bladed rotor:

$$\mathbf{x}^T = \begin{bmatrix} \beta_0 & \beta_{0d} & \beta_{1c} & \beta_{1s} \end{bmatrix} \tag{2.47}$$

where:

β_0 is the coning angle,

β_{0d} is differential coning,

β_{1c} is longitudinal cyclic flapping, and

β_{1c} is lateral cyclic flapping.

The corresponding Individual Blade Coordinates (IBC) are obtained using the following relation:

$$\beta^{(m)} = \beta_0 + \beta_{0d}(-1)^m + \beta_{1c}\cos\psi_m + \beta_{1s}\sin\psi_m \tag{2.48}$$

where:

$$\psi_m = \psi - (m-1)\frac{\pi}{2}, \quad m = 1, 2, 3, 4 \tag{2.49}$$

and m identifies the blade number. The LTP system can be approximated by a higher-order LTI system by the means of Harmonic Decomposition [25]. In order to

extract an approximate LTI model, each state is decomposed into a finite number of harmonics:

$$\mathbf{x} = \mathbf{x}_0 + \sum_{n=1}^{N} \left[\mathbf{x}_{nc} \cos n\psi + \mathbf{x}_{ns} \sin n\psi\right] \tag{2.50}$$

The resulting approximate LTI system is given by:

$$\dot{\mathbf{X}} = \mathbf{A}\mathbf{X} \tag{2.51}$$

where the augmented state vector is:

$$\mathbf{X}^T = \begin{bmatrix}\mathbf{x}_0 & \mathbf{x}_{1c} & \mathbf{x}_{1s} & \cdots & \mathbf{x}_{Nc} & \mathbf{x}_{Ns}\end{bmatrix} \tag{2.52}$$

By substituting the harmonic decomposition of each state from Eq. 2.50 into Eq. 2.48, and by collecting the coefficients contributing to each harmonic for each blade, one obtains the following equations relating the harmonics of the IBC states with the MBC states:

$$\beta_0^{(m)} = \beta_{0_0} + \beta_{0d_0}(-1)^m + \frac{1}{2}\left[f_1\left(\beta_{1c_{1c}} + \beta_{1s_{1s}}\right) + f_2\left(\beta_{1c_{1s}} - \beta_{1s_{1c}}\right)\right] \tag{2.53a}$$

$$\beta_{1c}^{(m)} = \beta_{0_{1c}} + \beta_{0d_{1c}}(-1)^m + \frac{1}{2}\left\{f_1\left[2\beta_{1c_0} + \beta_{1c_{2c}} + \beta_{1s_{2s}}\right] + f_2\left[-2\beta_{1s_0} + \beta_{1c_{2s}} - \beta_{1s_{2c}}\right]\right\} \tag{2.53b}$$

$$\beta_{1s}^{(m)} = \beta_{0_{1s}} + \beta_{0D_{1s}}(-1)^m + \frac{1}{2}\left\{f_1\left[2\beta_{1s_0} + \beta_{1c_{2s}} - \beta_{1s_{2c}}\right] + f_2\left[2\beta_{1c_0} - \beta_{1c_{2c}} - \beta_{1s_{2s}}\right]\right\} \tag{2.53c}$$

$$\beta_{nc}^{(m)} = \beta_{0_{nc}} + \beta_{0D_{nc}}(-1)^m + \frac{1}{2}\left\{f_1\left[\beta_{1c_{(n-1)c}} - \beta_{1s_{(n-1)s}} + \beta_{1c_{(n+1)c}} + \beta_{1s_{(n+1)s}}\right] + f_2\left[-\beta_{1c_{(n-1)s}} - \beta_{1s_{(n-1)c}} + \beta_{1c_{(n+1)s}} - \beta_{1s_{(n+1)c}}\right], \quad n \geq 2 \tag{2.53d}$$

$$\beta_{ns}^{(m)} = \beta_{0_{ns}} + \beta_{0D_{ns}}(-1)^m + \frac{1}{2}\left\{f_1\left[\beta_{1c_{(n-1)s}} + \beta_{1s_{(n-1)c}} + \beta_{1c_{(n+1)s}} - \beta_{1s_{(n+1)c}}\right] +$$

$$f_2\left[\beta_{1c_{(n-1)s}} - \beta_{1s_{(n-1)c}} - \beta_{1c_{(n+1)s}} - \beta_{1s_{(n+1)c}}\right], \quad n \geq 2 \quad (2.53e)$$

where:

$$f_1 = \begin{cases} 1 & m = 1 \\ 0 & m = 2, 4 \\ -1 & m = 3 \end{cases} \quad (2.54a)$$

$$f_2 = \begin{cases} 0 & m = 1, 3 \\ 1 & m = 2 \\ -1 & m = 4 \end{cases} \quad (2.54b)$$

It appears that each harmonic of the IBC states is influenced by the same, and a lower and a higher harmonic of the MBC states. This means that for high-order LTI systems to capture the behavior of IBC states up to the N^{th} harmonic, one has to retain up to the $(N+1)^{\text{th}}$ harmonic when performing harmonic decomposition on LTP systems with MBC states. Vice versa, if one retains up to the N^{th} harmonic when performing harmonic decomposition on LTP systems with MBC states, the IBC states will be reconstructed accurately only up to the $(N-1)^{\text{th}}$ harmonic.

In light of these results, the number of harmonics retained for the state and the output are $N = 5$ and $L = 4$, respectively. The resulting number of states for the high-order LTI model relative to the conventional helicopter and compound rotorcraft is 1276 and 1320, respectively. The high-order LTI model has 90 outputs for both aircraft. This way the approximate LTI model captures harmonics up to 4/rev.

2.1.6 Singular Perturbation Theory Overview

The measurement or estimation of states associated with the higher-order flap, lead-lag, torsion and inflow dynamics is impractical in real applications. For this

reasons, reduced-order models are derived from the high-order LTI model. To do so, singular perturbation theory is used. Consider a set of differential equations:

$$\dot{\mathbf{x}} = \mathbf{f}(\mathbf{x}, \mathbf{z}, \mathbf{u}, t, \mu) \tag{2.55a}$$

$$\mu\dot{\mathbf{z}} = \mathbf{g}(\mathbf{x}, \mathbf{z}, \mathbf{u}, t, \mu) \tag{2.55b}$$

where:

$\mu > 0$ is a scalar,

$\mathbf{x}$ is a subset of the state vector of dimension n,

$\mathbf{z}$ is a subset of the state vector of dimension m, and

$\mathbf{u}$ is the input vector of dimension r.

For $0 < \mu \ll 1$ the dynamics of the second set of differential equations is substantially faster than the first set. Under this condition, one can assume that the dynamics of the second set of differential equations reach steady-state more quickly than the first set. Formally:

$$0 = \mathbf{g}(\bar{\mathbf{x}}, \bar{\mathbf{z}}, \bar{\mathbf{u}}, t, 0) \tag{2.56}$$

The substitution of a root of Eq. 2.56:

$$\bar{\mathbf{z}} = \phi(\bar{\mathbf{x}}, \bar{\mathbf{z}}, t) \tag{2.57}$$

into Eq. 2.55a yields to a reduced-order model of order n:

$$\bar{\mathbf{x}} = \mathbf{f}\left[\bar{\mathbf{x}}, \phi(\bar{\mathbf{x}}, \bar{\mathbf{z}}, t), \bar{\mathbf{u}}, t, \mu\right] \equiv \bar{\mathbf{f}}(\bar{\mathbf{x}}, \bar{\mathbf{u}}, t) \tag{2.58}$$

The reduced-order model represents slow and neglects fast phenomena of the system in Eq. 2.55. A more detailed derivation is found in Ref. [56].

In light of this result, the state of the high-order LTI system is divided in slow

and fast components:

$$\mathbf{X} = \begin{bmatrix} \mathbf{X}_s \\ \mathbf{X}_f \end{bmatrix} \tag{2.59a}$$

The high-order LTI system is re-written as:

$$\begin{bmatrix} \dot{\mathbf{X}}_s \\ \dot{\mathbf{X}}_f \end{bmatrix} = \begin{bmatrix} \mathbf{A}_s & \mathbf{A}_{sf} \\ \mathbf{A}_{fs} & \mathbf{A}_f \end{bmatrix} \begin{bmatrix} \mathbf{X}_s \\ \mathbf{X}_f \end{bmatrix} + \begin{bmatrix} \mathbf{B}_s \\ \mathbf{B}_f \end{bmatrix} \mathbf{U} \tag{2.59b}$$

$$\mathbf{Y} = \begin{bmatrix} \mathbf{C}_s & \mathbf{C}_f \end{bmatrix} \begin{bmatrix} \mathbf{X}_s \\ \mathbf{X}_f \end{bmatrix} + \mathbf{D}\mathbf{u} \tag{2.59c}$$

Similarly to before, because the fast and stable states reach steady state more quickly than the slow states, the algebraic constraint $\dot{\mathbf{x}}_f = 0$ is imposed. It follows that:

$$\mathbf{A}_{fs}\mathbf{X}_s + \mathbf{A}_{fs}\mathbf{X}_f + \mathbf{B}_f\mathbf{U} = 0 \tag{2.60}$$

Solving for the fast states leads to:

$$\mathbf{X}_f = {\mathbf{A}_f}^{-1}(-\mathbf{A}_{fs}\mathbf{X}_s - \mathbf{B}_f\mathbf{U}) \tag{2.61}$$

By substituting the Eq. 2.61 result into Eq. 2.59b, the state equation for the reduced-order model is obtained:

$$\dot{\mathbf{X}}_s = \hat{\mathbf{A}}\mathbf{X}_s + \hat{\mathbf{B}}\mathbf{U} \tag{2.62}$$

where:

$$\hat{\mathbf{A}} = \mathbf{A}_s - \mathbf{A}_{sf}{\mathbf{A}_f}^{-1}\mathbf{A}_{fs} \tag{2.63a}$$

$$\hat{\mathbf{B}} = \mathbf{B}_s - \mathbf{A}_{sf}{\mathbf{A}_f}^{-1}\mathbf{B}_f \tag{2.63b}$$

By substituting Eq. 2.61 into Eq. 2.59c, the output equation for the reduced-order

model is obtained:

$$\mathbf{Y}_s = \hat{\mathbf{C}}\mathbf{X}_s + \hat{\mathbf{D}}\mathbf{U} \tag{2.64}$$

where:

$$\hat{\mathbf{C}} = \mathbf{C}_s - \mathbf{C}_f {\mathbf{A}_f}^{-1}\mathbf{A}_{fs} \tag{2.65a}$$

$$\hat{\mathbf{D}} = \mathbf{D} - \mathbf{C}_f {\mathbf{A}_f}^{-1}\mathbf{B}_f \tag{2.65b}$$

2.1.7 9-State Model

Singular perturbation theory is used to derive a 9-state model that is meant to be used for control system design. The 9-state model retains the 0^{th} harmonic of the rigid-body dynamics but neglects the higher-order dynamics. The state vector of the high-order LTI system is divided as follows:

$$\mathbf{X}_s = \left[\mathbf{x}_{\text{RB}_0}\right] \tag{2.66}$$

$$\mathbf{X}_f^T = \left[\mathbf{x}_{\text{R}_0}^T \ \mathbf{x}_{\text{RB}_{1c}}^T \ \mathbf{x}_{\text{R}_{1c}}^T \ \cdots \ \mathbf{x}_{\text{RB}_{Ns}}^T \ \mathbf{x}_{\text{R}_{Ns}}^T\right] \tag{2.67}$$

The higher-harmonics of the rigid-body states are truncated from the output because they are impractical to observe and of negligible amplitude when compared to their respective 0^{th} harmonic. The output reduces to:

$$\mathbf{Y}_s^T = \left[\mathbf{x}_{\text{RB}_0}^T \ \text{PLL}_0 \ \text{PLL}_{1c} \ \text{PLL}_{1s} \ \cdots \ \text{PLL}_{Lc} \ \text{PLL}_{Ls}\right] \tag{2.68}$$

Note that all of the higher harmonics of the pitch link loads are kept in the output to capture the influence of the rigid body states and controls on the rotor loads. Since state vector of the reduced-order model is constituted only by the 0^{th} harmonic of the rigid-body states, a controller that uses full-state feedback will only need the rigid-body states as feedback. This is generally the case for Automatic Flight Control Systems (AFCS) on contemporary rotorcraft.

2.1.8 15-State Model

Singular perturbation theory is used to derive a second reduced-order model that includes the 0^{th} harmonic of both rigid-body states and rotor flapping in the state vector. Specifically, the longitudinal and lateral flapping states are retained to model the regressive flap mode, the slowest rotor flapping mode (as compared to the progressive flapping mode). This is done to increase the spectrum of frequencies that the reduced-order model is a valid approximation for. The state vector of the high-order LTI system is divided as follows:

$$\mathbf{X}_s^T = \begin{bmatrix} \mathbf{x}_{\text{RB}_0}^T & \beta_{1c_0} & \beta_{1s_0} & \beta_{0_{1c}} & \beta_{0d_{1c}} & \beta_{0_{1s}} & \beta_{0d_{1s}} \end{bmatrix} \tag{2.69a}$$

$$\mathbf{X}_f^T = \begin{bmatrix} \hat{\mathbf{x}}_{\text{R}0}^T & \mathbf{x}_{\text{RB}_{1c}}^T & \hat{\mathbf{x}}_{\text{R}1c}^T & \cdots & \mathbf{x}_{\text{RB}_{Ns}}^T & \mathbf{x}_{\text{R}_{Ns}}^T \end{bmatrix} \tag{2.69b}$$

where $\hat{(.)}$ denotes the 0^{th} and 1^{st} harmonic rotor states deprived of the longitudinal and lateral flapping states. Note that $\beta_{0_{1c}}$, $\beta_{0d_{1c}}$, $\beta_{0_{1s}}$ and $\beta_{0d_{1s}}$ are retained in the slow component of the state as they are redundant states arising from harmonic decomposition; failure to retain them all may cause problems in the application of singular perturbation theory. Although the redundancy of the flapping states is not immediately apparent, it is illustrated in the Section 2.2.

The higher-harmonics of the rigid-body states and rotor flapping are truncated from the output because they are impractical to observe and of negligible amplitude when compared to their respective 0^{th} harmonic. The output reduces to:

$$\mathbf{Y}_s^T = \begin{bmatrix} \mathbf{x}_{\text{RB}_0}^T & \beta_{1c_0} & \beta_{1s_0} & \beta_{0_{1c}} & \beta_{0d_{1c}} & \beta_{0_{1s}} & \beta_{0d_{1s}} & \text{PLL}_0 & \text{PLL}_{1c} & \text{PLL}_{1s} & \cdots & \text{PLL}_{Lc} & \text{PLL}_{Ls} \end{bmatrix} \tag{2.70}$$

Note that all of the higher harmonics of the pitch link loads are kept in the output to capture the influence of the rigid body, rotor flapping states, and controls on the rotor loads. Since state vector of the reduced-order model is constituted by the 0^{th} harmonic of the rigid-body states and rotor flapping, a controller that uses

full-state feedback will need both rigid-body states and rotor flapping states as feedback.

2.1.9 Algebraic Constraints Removal

Consider the full state-space representation of an LTI system, exemplifying a harmonic decomposition model:

$$\dot{\mathbf{X}} = \mathbf{A}\mathbf{X} + \mathbf{B}\mathbf{U} \tag{2.71a}$$

$$\mathbf{Y} = \mathbf{C}\mathbf{X} + \mathbf{D}\mathbf{U} \tag{2.71b}$$

where $\mathbf{X} \in \Re^L$, $\mathbf{U} \in \Re^M$, and $\mathbf{Y} \in \Re^P$. Consider the state vector:

$$\mathbf{X}^T = \begin{bmatrix} X_1 & \dots & X_i & \dots & X_j & \dots & X_L \end{bmatrix} \tag{2.72}$$

Suppose that two states are linearly dependent:

$$X_j = kX_i \tag{2.73}$$

Then, a reduced-order state-space system can be defined:

$$\dot{\hat{\mathbf{X}}} = \hat{\mathbf{A}}\hat{\mathbf{X}} + \hat{\mathbf{B}}\mathbf{U} \tag{2.74a}$$

$$\mathbf{Y} = \hat{\mathbf{C}}\hat{\mathbf{X}} + \mathbf{D}\mathbf{U} \tag{2.74b}$$

where $\hat{\mathbf{X}} \in \Re^{L-1}$ since the state X_j is removed from the new state vector. The reduced-order model state and output matrices are:

$$\hat{\mathbf{A}} = \begin{bmatrix} a_{1,1} & \dots & a_{1,i} + ka_{1,j} & \dots & a_{1,L-1} \\ \vdots & \ddots & \vdots & \ddots & \vdots \\ a_{L-1,1} & \dots & a_{L-1,i} + ka_{L-1,j} & \dots & a_{L-1,L-1} \end{bmatrix} \tag{2.75a}$$

$$\hat{\mathbf{C}} = \begin{bmatrix} c_{1,1} & \dots & c_{1,i} + kc_{1,j} & \dots & c_{1,L-1} \\ \vdots & \ddots & \vdots & \ddots & \vdots \\ c_{P,1} & \dots & c_{P,i} + kc_{P,j} & \dots & c_{P,L-1} \end{bmatrix} \tag{2.75b}$$

The input matrix $\hat{\mathbf{B}}$ is obtained by removing the L^{th} row from $\mathbf{B}$. This methodology can be used towards the removal on redundant states in harmonic decomposition models.

2.1.10 11-State Model

Consider the following relations between the flapping states:

$$\beta_{1c_0} = \beta_{0_{1c}} = -\beta_{0d_{1c}} \tag{2.76a}$$

$$\beta_{1s_0} = \beta_{0_{1s}} = -\beta_{0d_{1s}} \tag{2.76b}$$

An 11-state model is derived from the 15-state model by applying algebraic constraint removal. The state vector of the 11-state is:

$$\hat{\mathbf{X}}_s^T = \begin{bmatrix} \mathbf{x}_{B_0}^T & \beta_{1c_0} & \beta_{1s_0} \end{bmatrix} \tag{2.77}$$

The output reduces to:

$$\mathbf{Y}_s^T = \begin{bmatrix} \mathbf{x}_{\mathrm{RB}_0}^T & \beta_{1c_0} & \beta_{1s_0} & \mathrm{PLL}_0 & \mathrm{PLL}_{1c} & \mathrm{PLL}_{1s} & \cdots & \mathrm{PLL}_{4s} \end{bmatrix} \tag{2.78}$$

2.2 Linear Models Validation

2.2.1 Conventional Helicopter

The first step of the validation is to compare the high-order linear system with flight test data. Specifically, the high-order LTI model for the conventional heli-

copter is compared to JUH-60A Black Hawk flight test data at a 80 kts level flight. The comparison is done at 80 kts since flight test data is available only at such condition for forward flight. The flight test data was originally collected for the Army/NASA Rotorcraft Aircrew Systems Concepts Airborne Laboratory (RASCAL) program. This is done to ensure that the simulation model is representative of an H-60 aircraft. Figure 2.3 shows a comparison between the on-axis frequency responses obtained from flight test data and from the high-order LTI model. For high coherence values (greater than 0.6) the frequency responses generally match fairly well. However, lateral and longitudinal flapping responses for the high-order LTI model show slightly decreased magnitude when compared to the flight test data.

For frequencies corresponding to high coherence values, the magnitude and phase relative errors for each on-axis frequency response are plotted to provide further insight on the similarities/discrepancies between the linearized simulation model and the model identified from JUH-60A flight test data (Fig. 2.4). The plot also includes the mismatch boundaries defined in MIL-STD-1797 [57]. These boundaries represent the Maximum Unnoticeable Added Dynamics (MUAD) limits. When these limits are exceeded, a pilot can typically detect discrepancies between two aircraft modes being compared [58]. The roll rate response to the lateral stick, the yaw rate response to the pedals, and the collective flap angle due to the collective stick are well between the MUAD boundaries for the frequencies in consideration. The pitch rate response to longitudinal cyclic is inaccurate in the phase especially at low frequencies. Both the lateral flapping response to the lateral stick and the longitudinal flapping response to a longitudinal stick show a mismatch in the magnitude, whereas the phase error is well within the MUAD boundaries. This may be because for the high-order LTI system what is actually calculated is the frequency response from the lateral and longitudinal sticks to the 0^{th} harmonics of the lateral and longitudinal flapping angles, respectively. The

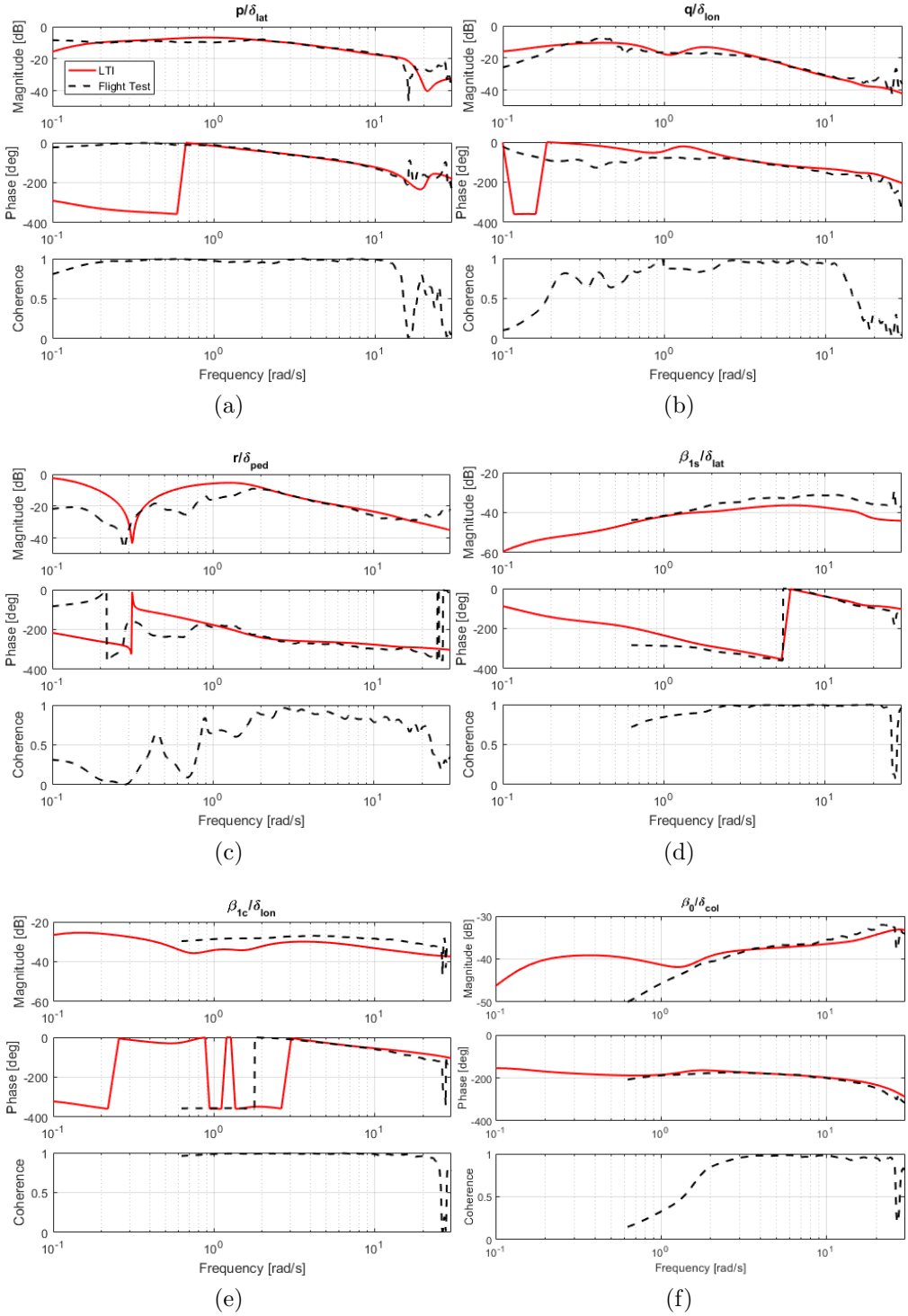

Figure 2.3: On-axis frequency response: flight data vs. high-order LTI system.

higher-harmonics of lateral and longitudinal flapping could contribute to the overall flapping response to the pilot inputs significantly and could compensate for the reduced magnitude in the 0^{th} harmonic response.

Consider a cost function that quantifies the error between two frequency responses [58]:

$$J = \frac{20}{n_\omega} \sum_{\omega_1}^{\omega_{n_\omega}} W_\gamma [W_g(|T_1| - |T_2|)^2 + W_p(\angle T_1 - \angle T_2)^2] \tag{2.79}$$

where:

n_ω is the number of frequency points,

ω_1 and ω_{n_ω} are the upper and lower frequencies of fit,

T_1 and T_2 are the two frequency responses, and

W_γ, W_g, and W_p are weighting functions.

Specifically, W_γ is a weighting function dependent on the value of the coherence function at each frequency point $\omega_1, \omega_2, ..., \omega_{n_\omega}$ and for each frequency response pair T_l:

$$W_\gamma(\omega) = \left[1.58\left(1 - e^{-\gamma_{xy}^2}\right)\right]^2 \tag{2.80}$$

where γ_{xy}^2 is the coherence function, thereby emphasizing the most reliable data. W_g and W_p are the relative weights for magnitude and phase squared errors:

$$W_g = 1.0 \tag{2.81a}$$

$$W_p = 0.01745 \tag{2.81b}$$

This cost function is used to quantify the relative error between each on-axis frequency response of the two models in consideration. An average cost function across all cost functions for each individual frequency response of $J \leq 100$ generally reflects an acceptable level of accuracy for flight dynamics modeling, whereas a cost function of $J \leq 50$ can be expected to produce a model that is nearly indis-

Table 2.1: On-axis frequency responses individual cost functions.

Frequency Response	Frequency Range [rad/s]	Cost
p/δ_{lat}	0.3-10	61.93
q/δ_{lon}	0.4-10	342.27
r/δ_{ped}	2-20	61.73
$\beta_{1s}/\delta_{\text{lat}}$	1-20	482.09
$\beta_{1c}/\delta_{\text{lon}}$	0.7-20	434.51
$\beta_0/\delta_{\text{col}}$	1-20	24.78

tinguishable from the original in the frequency and time domain. However, some of the individual cost functions can reach $J \leq 200$ without resulting in a noticeable loss of overall predictive accuracy [58]. The individual cost functions are reported in Table 2.1 and substantiate the previous observations. It is concluded that the simulation model for the conventional helicopter is generally a good representation of an H-60 aircraft. It should be noted that the FLIGHTLAB® model is reflective of a general H-60 helicopter and was not tuned to be representative of a JUH-60A configuration.

Once the fidelity of the high-order LTI model is established, the validity of the reduced-order models is assessed. The on-axis frequency responses of the of the reduced-order models are compared to the high-order LTI system, as shown in Fig. 2.5. The frequency responses of the reduced-order models match closely the high-order LTI model in the low frequency range. The 9-state model shows good accuracy up to about 4 rad/s. The 11-state model shows good accuracy up to about 10 rad/s. This is because the 11-state model incorporates the flapping states and therefore is able to predict the dynamics of the regressive flap mode. Both reduced-order models have reduced phase delay when compare to the high-order LTI model. This is due to the absence of the actuator states in the reduced order models. Further, the 9-state model has reduced phase delay when compared to the 11-state model. This is because the 9-state model lacks the rotor dynamics and is unable to predict the delay in the response caused by rotor flapping. Further

Table 2.2: On-axis frequency responses individual cost functions for a frequency range of 0.3 to 4 rad/s and coherence equal to 1.

Frequency Response	Cost (LTI - LTI 9)	Cost (LTI - LTI 11)
p/δ_{lat}	13.43	6.43
q/δ_{lon}	42.85	21.32
r/δ_{ped}	24.34	31.80

Table 2.3: On-axis frequency responses individual cost functions for a frequency range of 0.3 to 10 rad/s and coherence equal to 1.

Frequency Response	Cost (LTI - LTI 9)	Cost (LTI - LTI 11)
p/δ_{lat}	82.14	9.01
q/δ_{lon}	164.02	19.30
r/δ_{ped}	28.92	36.78

validation is conducted by computing the relative error between the frequency responses of the high order LTI model and the 9-state model, and between the high-order LTI model and the 11-state model, as shown in Fig. 2.6. It is clear that for both the roll rate response to the lateral stick and for the pitch rate response to the longitudinal stick the frequency response of the error between the high-order LTI and the 9-state model exceeds the MUAD boundaries starting at about 4 rad/s. For the same on-axis responses, the error between the high-order LTI and the 11-state model exceeds the MUAD boundaries for frequencies in excess of 10 rad/s. This substantiates the previous observations. The relative errors of the yaw rate response to the pedal never exceed the MUAD boundaries for the frequencies in consideration. Tables 2.2 and 2.3 shows the cost function for the relative error between high-order LTI and the reduced-order models for different frequency ranges. It is apparent that the 9-state model is nearly indistinguishable from the high-order LTI for frequencies up to 4 rad/s, whereas the 11-state model is nearly indistinguishable from the high-order LTI for frequencies up to 10 rad/s.

The fidelity of the reduced-order models is also assessed by comparing their

eigenvalues to the eigenvalues of the high-order LTI system. Figure 2.7 shows an enlarged eigenvalue plot. It is apparent that the high-order LTI system has many high frequency eigenvalues, a large number of which are very lightly damped. Figure 2.8 shows how the rigid-body eigenvalues of the reduced-order models match closely to the eigenvalues of the high-order LTI system. Further, the eigenvalues associated to the regressive flap mode of the 11-state model are close to the ones of the high-order LTI model. Finally, Fig. 2.9 shows the existence of unstable eigenvalues at very low frequencies (< 0.1 rad/s). These low frequency eigenvalues match closely between the high-order LTI model and the reduced-order model. It is concluded that that the model order reduction that is performed is robust and does not cause the migration of low-frequency eigenvalues to the right-half plane.

The ability of the reduced-order models to predict the pitch link loads is assessed. Figure 2.10 shows the frequency response of different harmonics of the pitch link loads to a lateral stick input. As for the rigid-body states, the 9-state model matches the high-order model up to about 4 rad/s, whereas the 11-state model up to about 10 rad/s. This is further substantiated by Fig. 2.11, where the error between the high-order LTI and reduced-order models is shown along the MUAD boundaries.

Further validation is conducted in the time domain. The open-loop response to a moderate lateral stick doublet is shown for the nonlinear FLIGHTLAB® model and the reduced-order models in Fig. 2.12. Both on-axis and off-axis responses for the reduced-order models match closely the nonlinear model response. Also the pitch link loads seem to be captured fairly accurately by the reduced-order models. The open-loop response to a more aggressive lateral stick doublet is shown in Fig. 2.13. While the angular rate response of the linear models is very similar to the one of the nonlinear model, some differences arise in the pitch link loads. This is justified by the fact that under such an aggressive maneuver, the helicopter may diverge from the trim condition at which the linear models were obtained.

Further, nonlinearities may become significant in the response. It is concluded that the reduced-order models are a close representation of the overall rotorcraft dynamics in low and medium frequency ranges. Further, the reduced-order models, by retaining the pitch link load higher-harmonics in the output, are able to predict the higher-harmonic component of the rotor loads.

2.2.2 Compound Rotorcraft

The on-axis frequency responses of the of the reduced-order models are compared to the high-order LTI system, as shown in Fig. 2.14. Most notably, the on-axis frequency responses to the redundant control surfaces are generally accurate up to up to about 10 rad/s for both 9-state and 11-state models. This is because the redundant control surfaces are aerodynamic devices without higher-order dynamics associated to them. Conversely, the primary flight controls act on the rotor which has plenty higher-order dynamics associated to it (i.e. flap, lead-lag, torsion, etc.).

The fidelity of the reduced-order model is also assessed by comparing its eigenvalues to the eigenvalues of the high-order LTI system, as shown in Fig. 2.15. As expected, the rigid-body eigenvalues of the reduced-order models match closely to the eigenvalues of the high-order LTI system. Further, the eigenvalues associated to the regressive flap mode of the 11-state model are fairly close to the ones of the high-order LTI model.

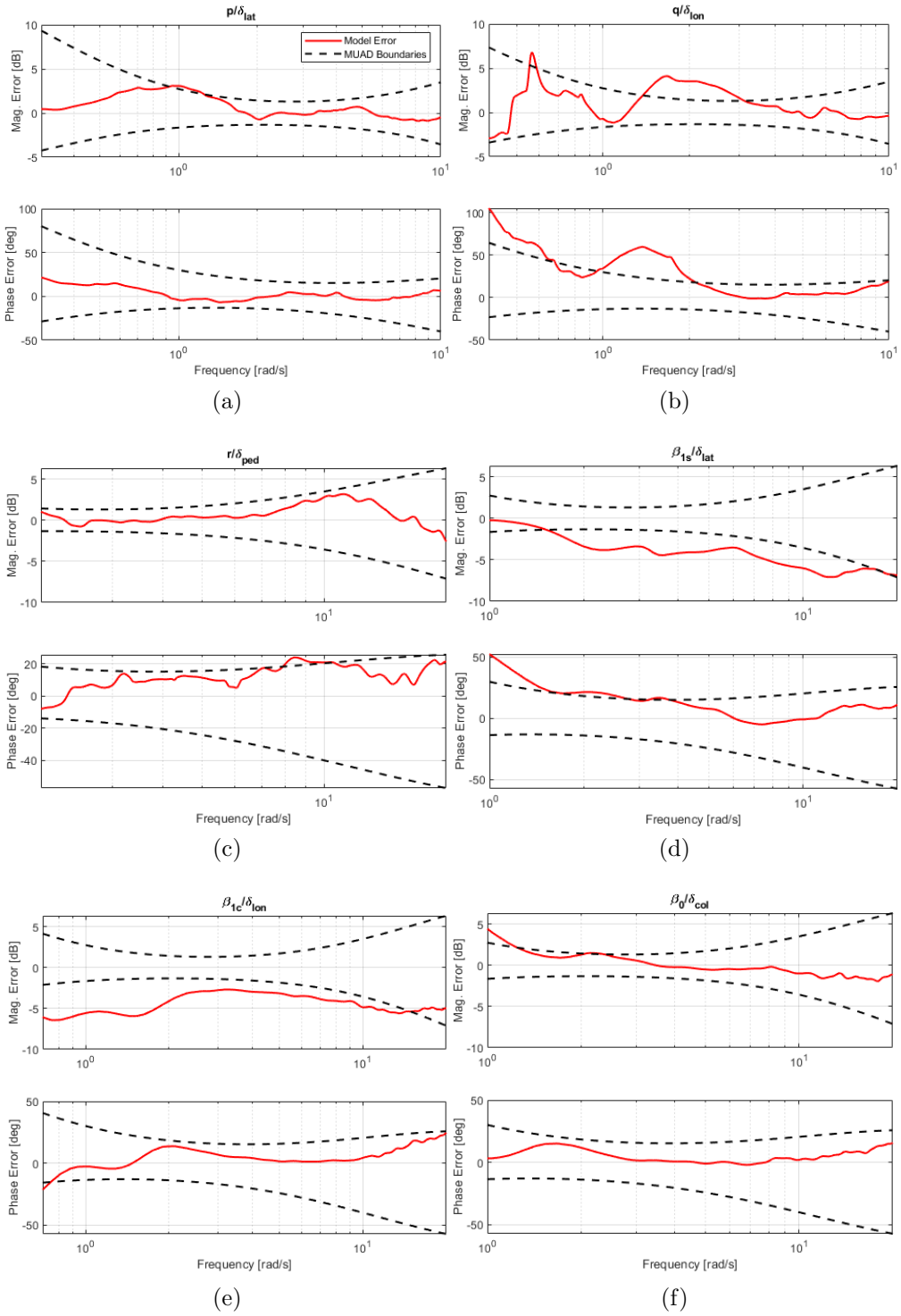

Figure 2.4: On-axis frequency response: error between flight data and high-order LTI system.

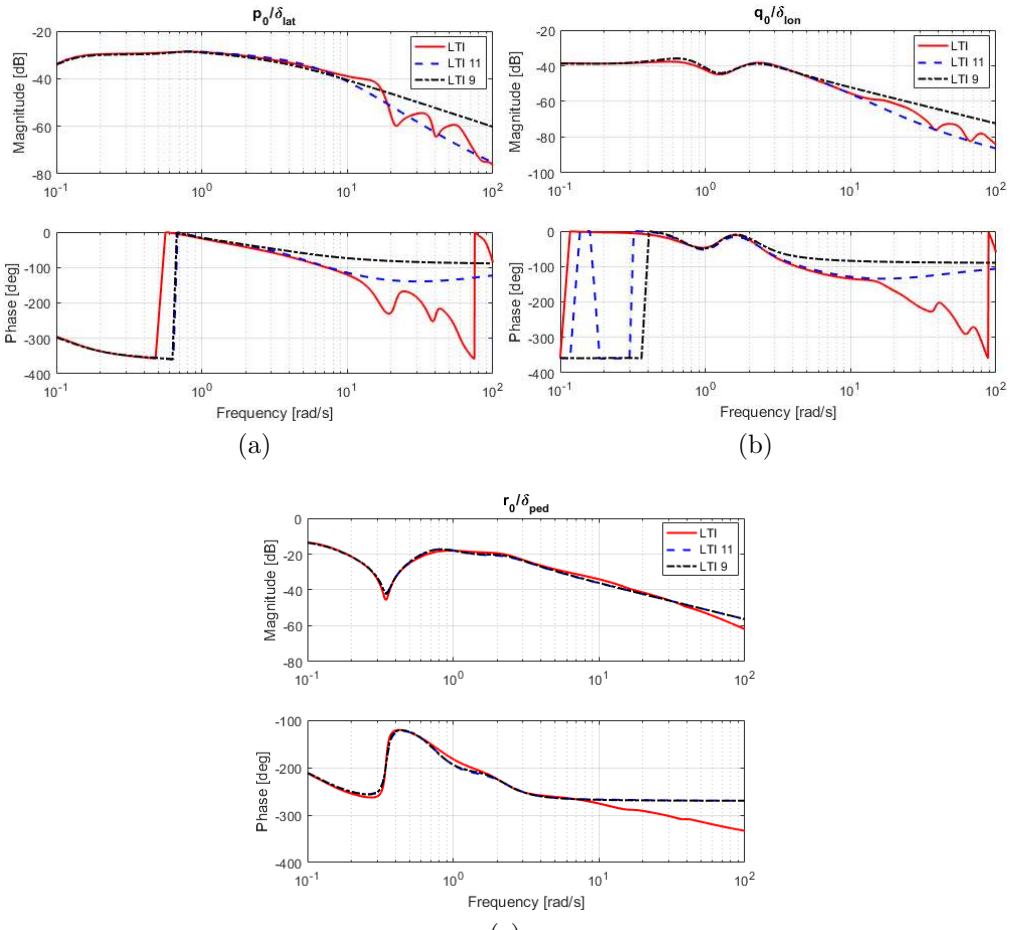

Figure 2.5: On-axis frequency responses: high-order LTI model vs. reduced-order models.

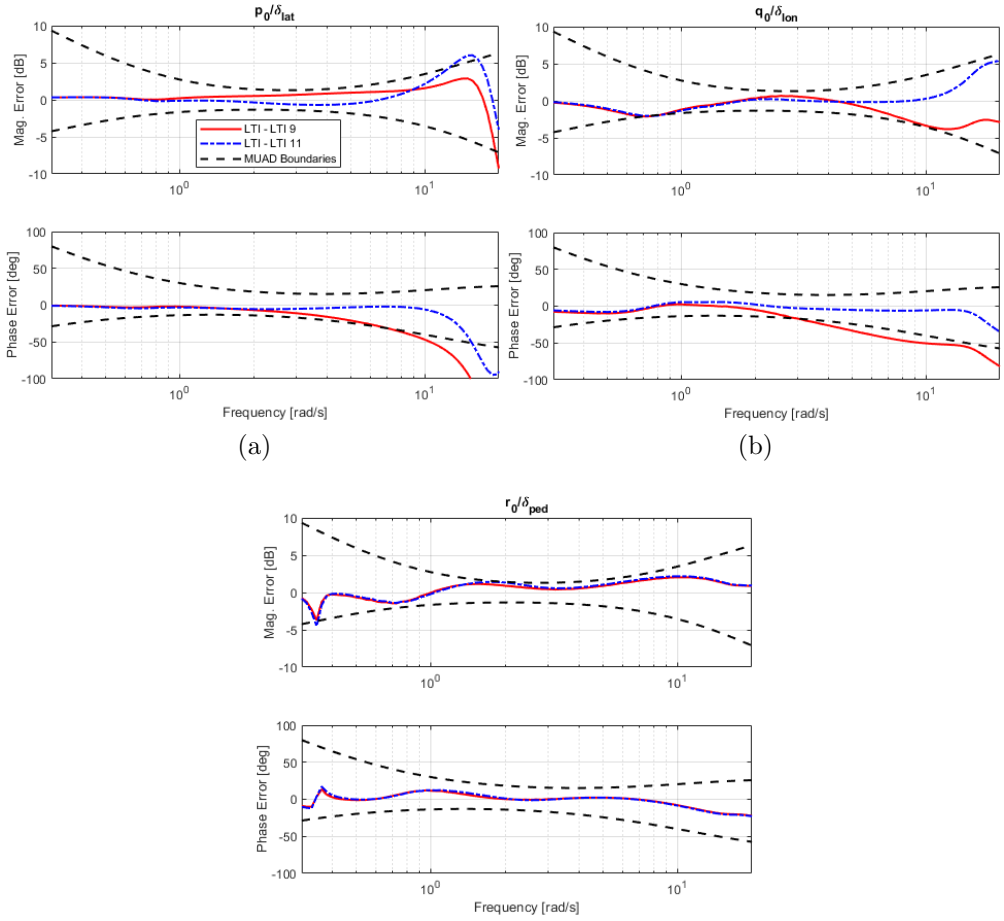

Figure 2.6: On-axis frequency responses: error between high-order LTI model and reduced-order models.

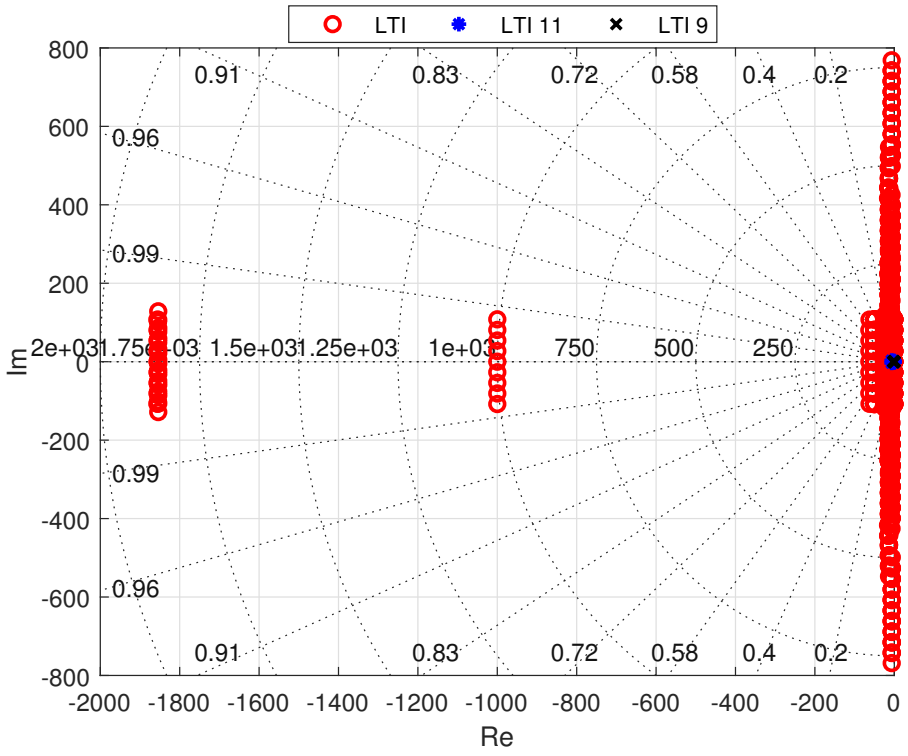

Figure 2.7: Eigenvalues: comparison between reduced-order models and high-order LTI model.

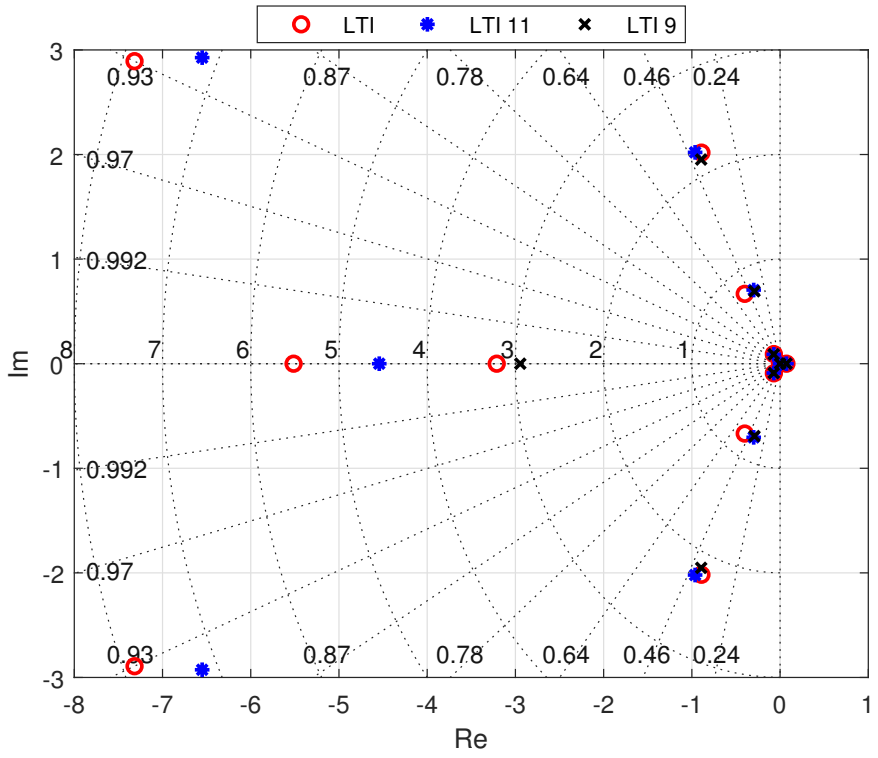

Figure 2.8: Eigenvalues: comparison between reduced-order models and high-order LTI model.

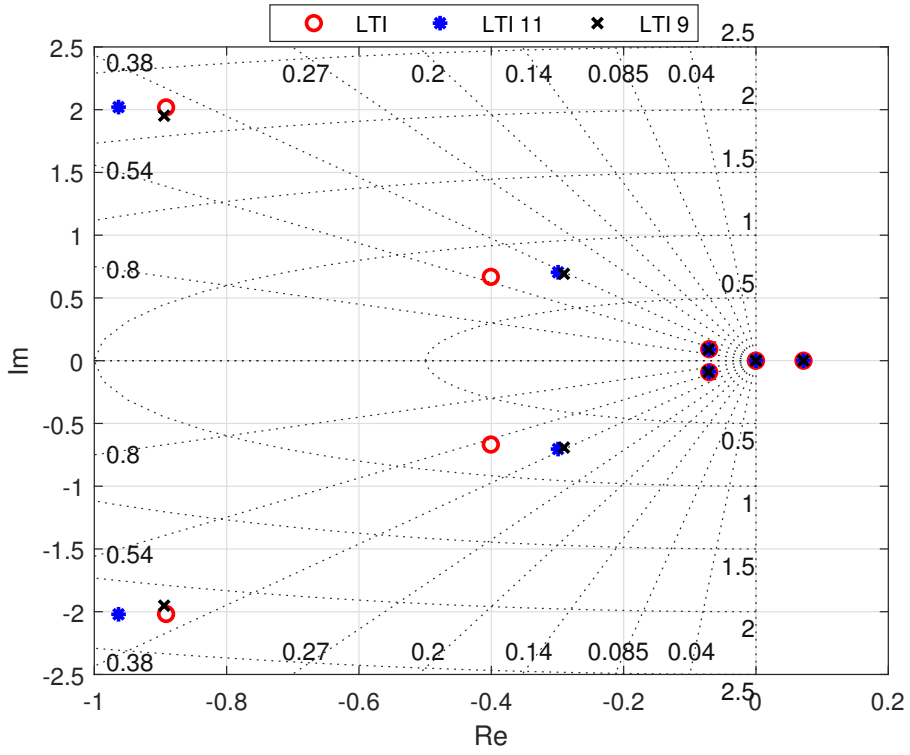

Figure 2.9: Eigenvalues: comparison between reduced-order models and high-order LTI model.

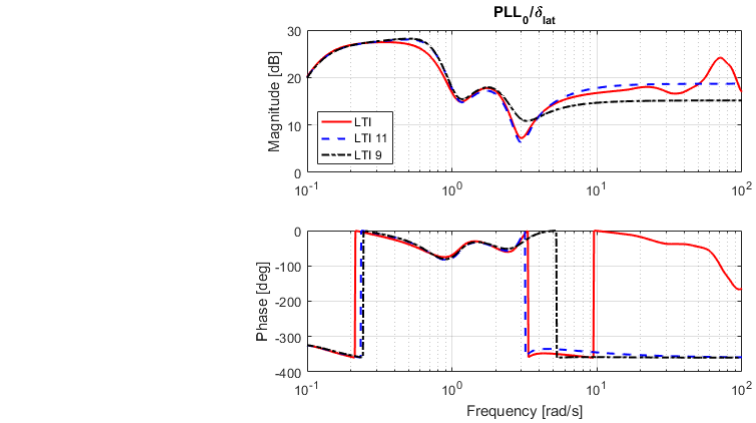

(a)

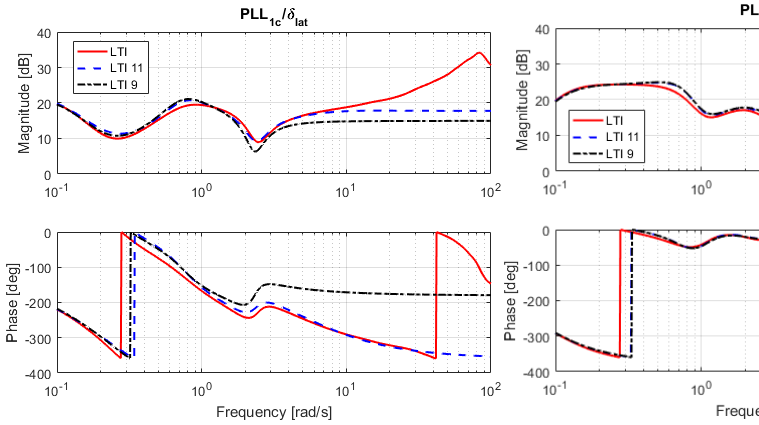

(b)

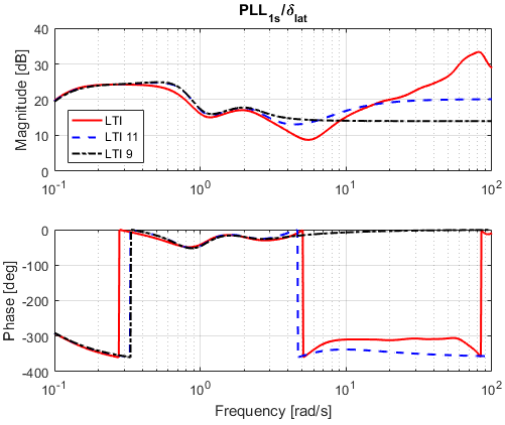

(c)

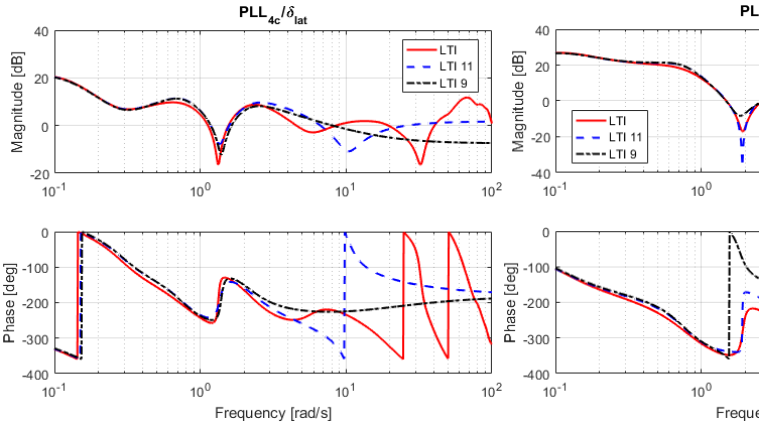

(d)

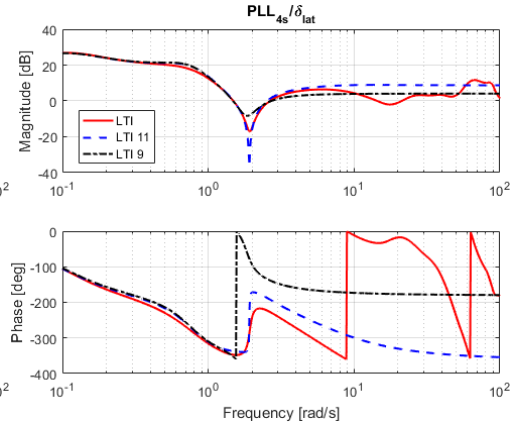

(e)

Figure 2.10: Pitch link load frequency response to a lateral stick input.

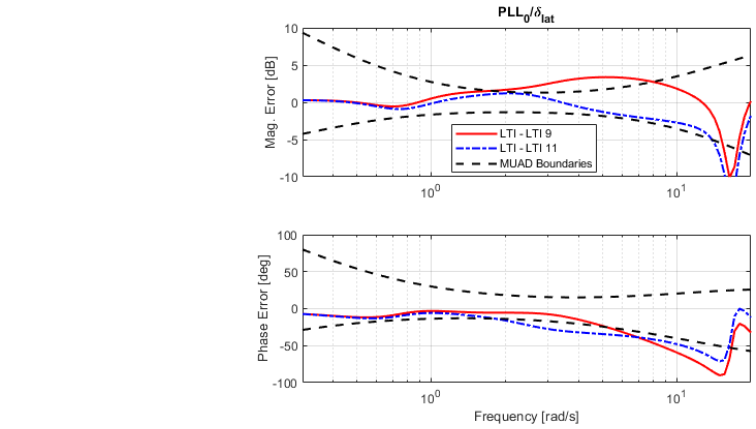

(a)

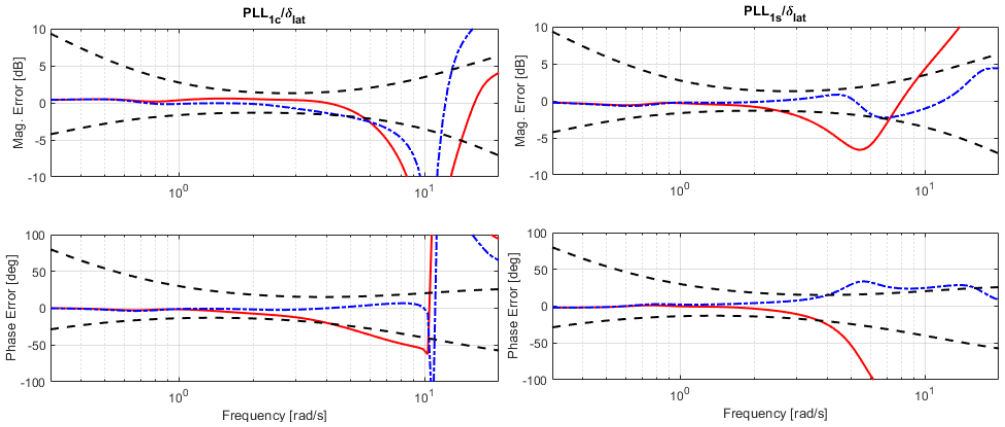

(b) (c)

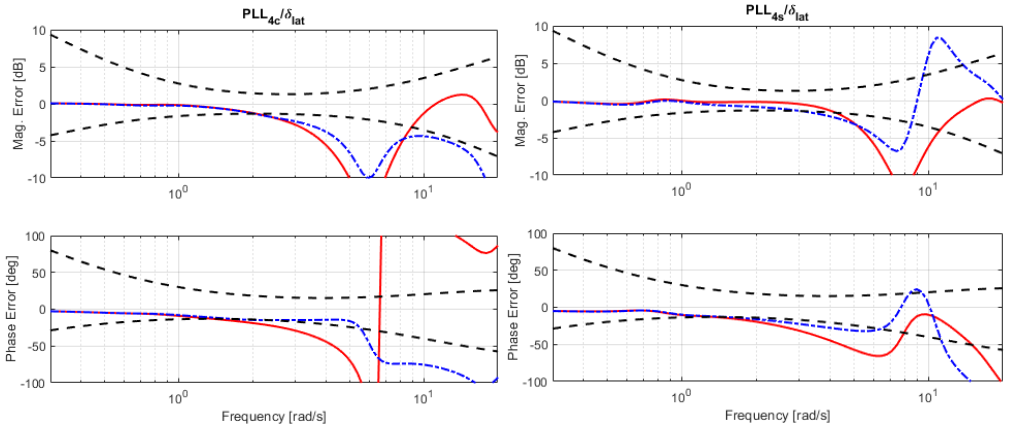

(d) (e)

Figure 2.11: Pitch link load frequency response to a lateral stick input: relative error between high-order LTI and reduced-order models.

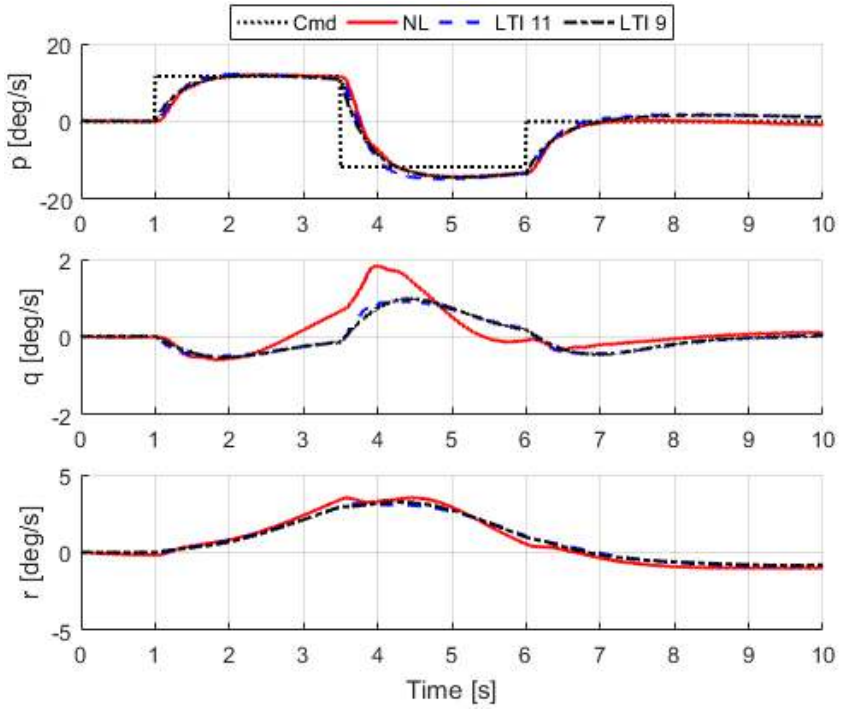

(a)

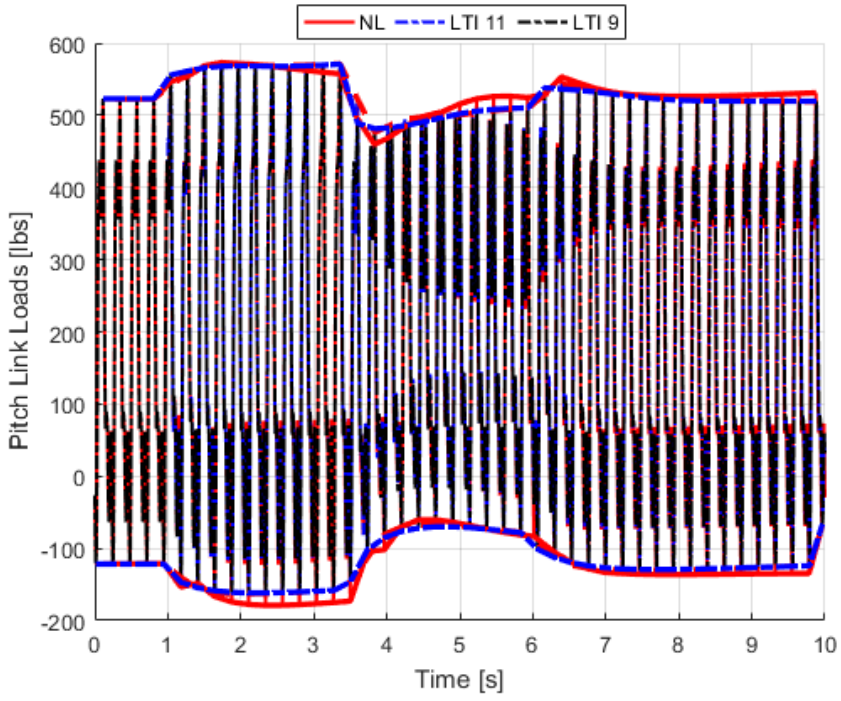

(b)

Figure 2.12: Open-loop time response to a moderate lateral stick doublet.

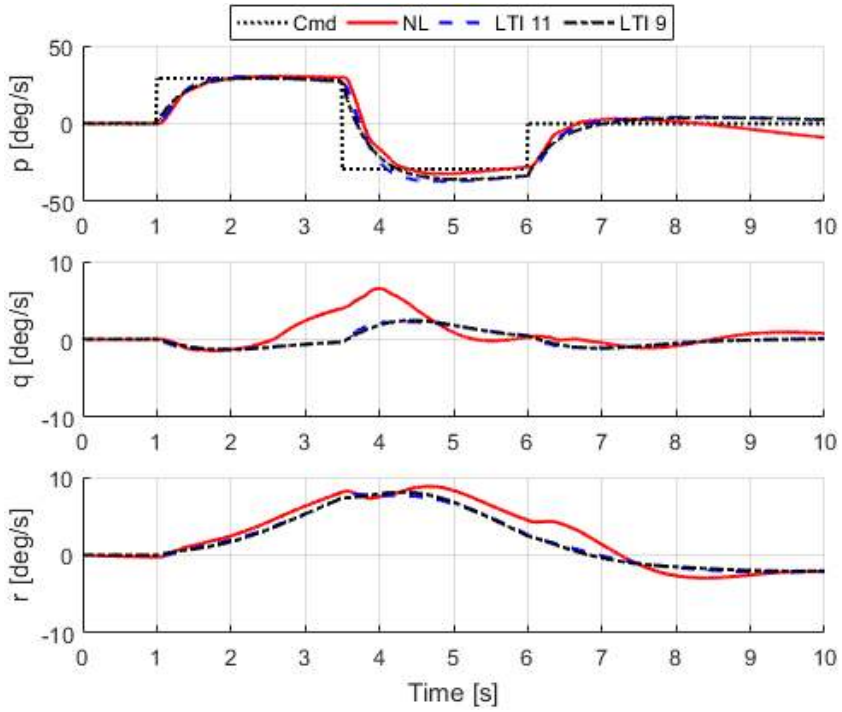

(a)

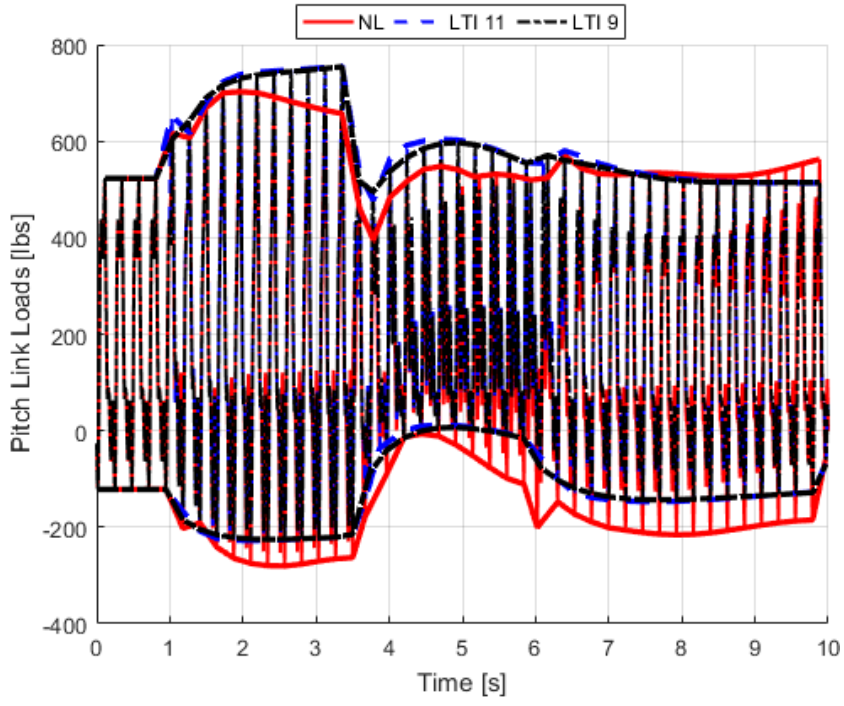

(b)

Figure 2.13: Open-loop time response to an aggressive lateral stick doublet.

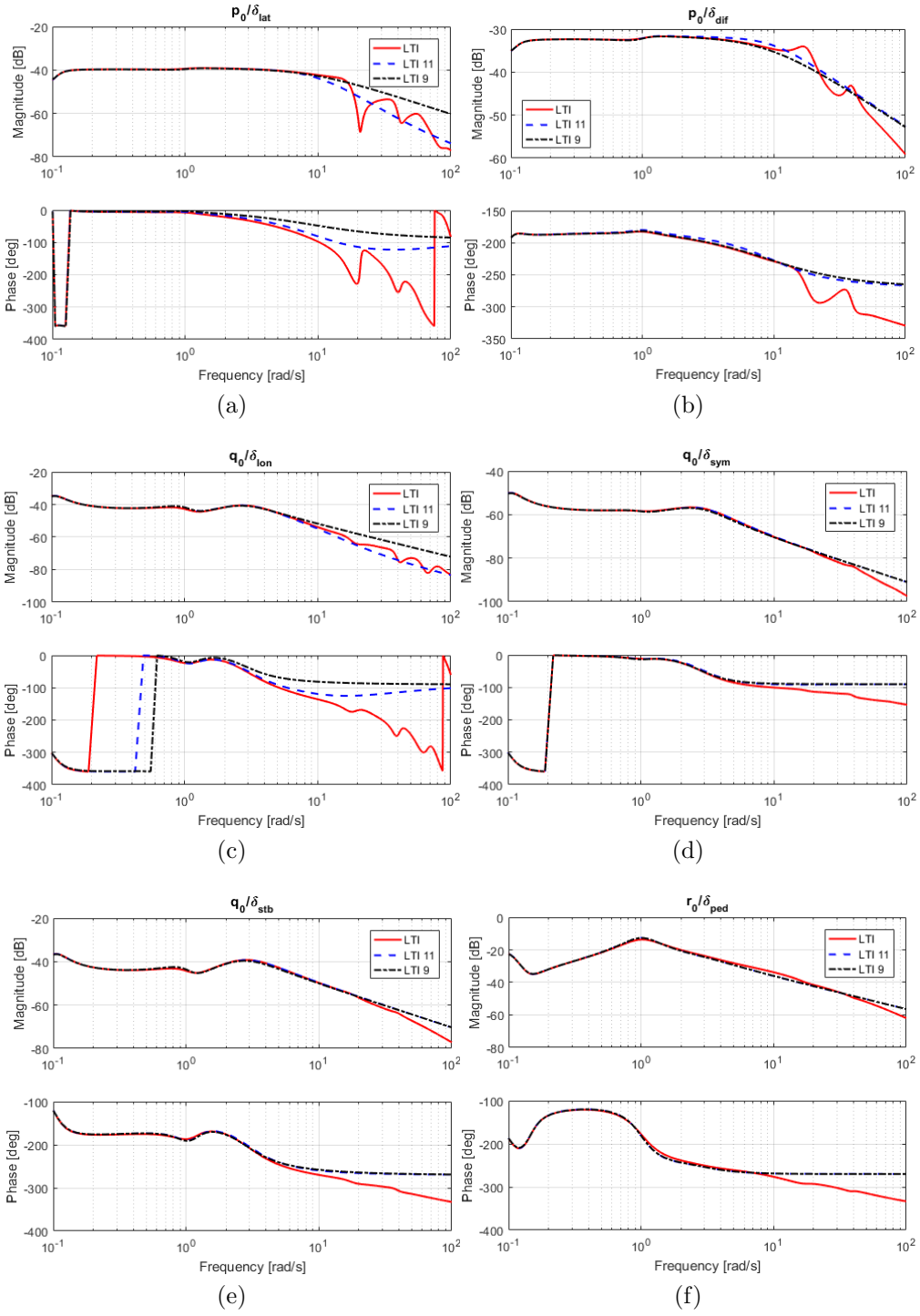

Figure 2.14: On-axis frequency response: flight data vs. high-order LTI system.

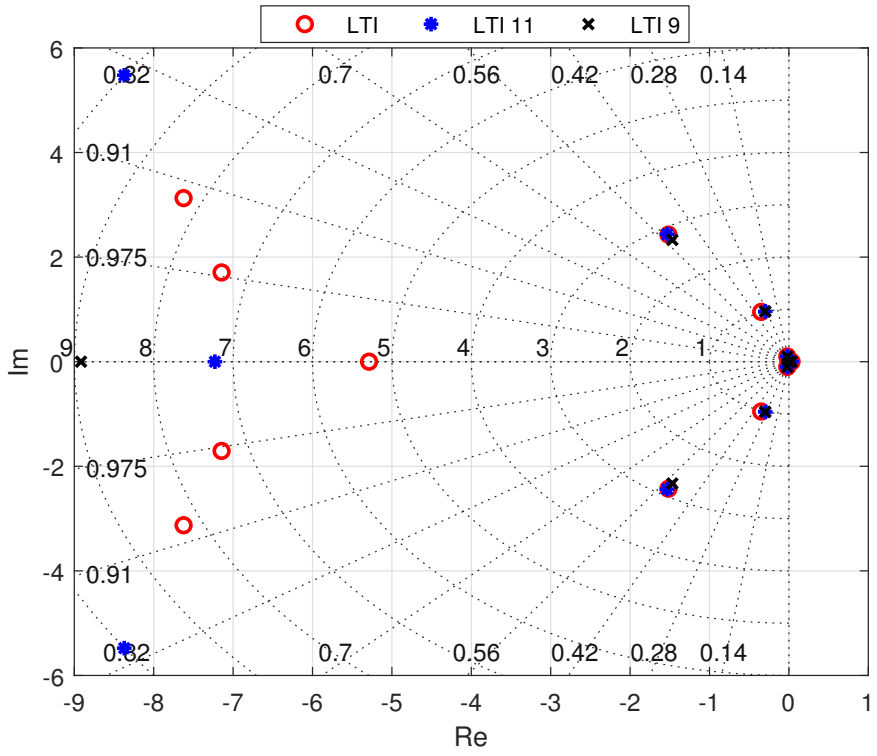

Figure 2.15: Eigenvalues: comparison between reduced-order models and high-order LTI model.

Chapter 3

Flight Control Design

3.1 Model Following Architecture

The chosen control strategy is Explicit Model Following (EMF). This choice is motivated by the fact that EMF is a largely adopted across aerospace manufacturers, and possibly the most common control architecture in the helicopter community. EMF naturally partitions the controller in a feed-forward and a feedback part. This allows the designer to easily tailor feed-forward compensation and have flexibility in the implementation of different feedback control strategies. A general Explicit Model Following scheme for a SISO system is shown in Fig. 3.1. The command model sets the desired dynamics of the closed-loop system. The inverse plant generates the feed-forward actuator inputs which command the aircraft to approximately follow the command-model responses. Feedback compensation is used to minimize the error between the commanded response and actual aircraft response. Equivalent command delays are used to synchronize the commanded and measured responses in time.

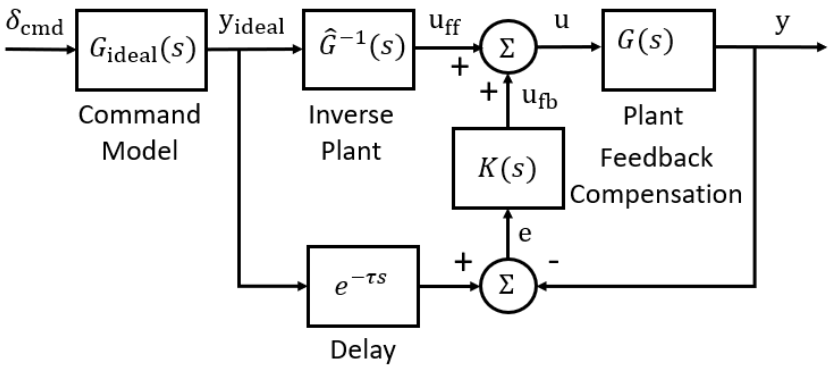

Figure 3.1: Explicit model following block diagram.

3.2 Conventional Helicopter Controller

The controller is designed to achieve stability and desired rate-command/attitude-hold (RCAH) response around the roll, pitch and yaw axes. The controller acts solely through primary flight controls. This restricts the maximum desired bandwidth of the input to be considerably less than the main rotor angular speed. This way, higher-harmonic control is excluded. Note that the collective stick is left open-loop. This is because in high-speed forward flight the pilot regulates altitude by using the cyclic stick rather than the collective stick.

3.2.1 Feed-forward Compensation

The command models (or filters) for the roll, pitch, and yaw axes are 1st order linear models:

$$\frac{p_{\text{cmd}}}{\delta_{\text{lat}}}(s) = \frac{k_{\delta_{\text{lat}}}}{\tau_p s + 1} \tag{3.1a}$$

$$\frac{q_{\text{cmd}}}{\delta_{\text{lon}}}(s) = \frac{k_{\delta_{\text{lon}}}}{\tau_q s + 1} \tag{3.1b}$$

$$\frac{r_{\text{cmd}}}{\delta_{\text{ped}}}(s) = \frac{k_{\delta_{\text{ped}}}}{\tau_r s + 1} \tag{3.1c}$$

$$\tag{3.1d}$$

where $k_{\delta_{\text{lat}}}$, $k_{\delta_{\text{lon}}}$, and $k_{\delta_{\text{ped}}}$ are the conversion constants from pilot commands to commanded angular rates, and τ_p, τ_q, and τ_r are the command filter time constants. To each command filter time constant corresponds a break frequency that is the inverse of the time constant. This means that $\omega_p = 1/\tau_p$, $\omega_q = 1/\tau_q$, and $\omega_r = 1/\tau_r$. The parameters of the command filters are tuned to the pilot response criteria, such as piloted bandwidth, phase delay, and sensitivity requirements. Generally, these parameters can be optimized as design parameters.

The inverse plant dynamics is based on approximate on-axis bare-airframe responses in the frequency range around crossover [59]. For this specific case, the inverse plant is based on the inverses of the following set of decoupled 1st order transfer functions:

$$\frac{p_{\text{cmd}}}{\delta_{\text{lat}_{\text{ff}}}}(s) = \frac{L_{\delta_{\text{lat}}}}{s - L_p} \tag{3.2a}$$

$$\frac{q_{\text{cmd}}}{\delta_{\text{lon}_{\text{ff}}}}(s) = \frac{M_{\delta_{\text{lon}}}}{s - M_q} \tag{3.2b}$$

$$\frac{r_{\text{cmd}}}{\delta_{\text{ped}_{\text{ff}}}}(s) = \frac{N_{\delta_{\text{ped}}}}{s - N_r} \tag{3.2c}$$

where the stability and control derivatives are pulled from the 9-state model. The commanded responses in each axis are delayed by τ_ϕ, τ_θ, and τ_ψ, respectively, for synchronization with the (higher-order) measured responses. These higher-order dynamics include the computational delays, actuators, rotor flapping lag, and sensors which cannot be included in the inverse model without causing actuator saturation. The time delays are calculated following the methods of Ref. [59]. The stability and control derivatives used for the inverse plants are found in Table 3.1. The equivalent delays are shown in Table 3.2.

In forward flight, the centrifugal forces arising from turns are compensated by banking the helicopter - and thus the thrust vector - towards the center of the turn. This is effectively achieved by relating the commanded yaw rate to the absolute

Table 3.1: Stability and control derivatives.

Parameter	Units	Value
L_p	1/s	-2.9560
M_q	1/s	-1.3061
N_r	1/s	-0.3855
$L_{\delta_{\text{lat}}}$	rad/(s^2-%)	0.0976
$M_{\delta_{\text{lon}}}$	rad/(s^2-%)	0.0242
$N_{\delta_{\text{ped}}}$	rad/(s^2-%)	-0.1526

Table 3.2: Equivalent delays.

Parameter	Units	Value
τ_ϕ	s	0.055
τ_θ	s	0.136
τ_ψ	s	0.025

speed and bank angle of the rotorcraft. The turn coordination law is:

$$r'_{\text{cmd}} = \frac{g}{V}\sin\psi + r_{\text{cmd}} \tag{3.3}$$

and is implemented in the feed-forward path of the controller. Since the heave axis is left open loop, feedback compensation does not provide adjustments to potential losses in altitude during turns causes by rotating the thrust vector around the roll axis. This is why turn compensation is added to the feed-forward path of the controller. The turn compensation law relates the pitch rate with yaw rate and bank angle of the rotorcraf, and is given by:

$$q'_{\text{cmd}} = r\sin\phi + q_{\text{cmd}} \tag{3.4}$$

More information on the derivation of turn compensation and turn coordination are found in Ref. [60].

3.2.2 Feedback Compensation

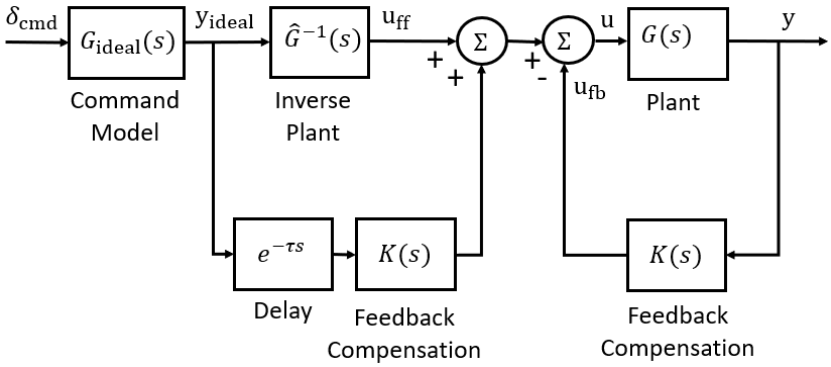

Figure 3.2: Explicit model following block diagram.

Since the loop on the right hand side of Fig. 3.1 is independent from the the feed-forward part of the controller, as shown in Fig. 3.2, feedback compensation can be obtained with standard techniques. The chosen strategy for feedback compensation is a linear Quadratic Regulator (LQR). The LQR gains are determined by using the reduced-order models previously derived. The cost function that is minimized is:

$$J = \int_0^t \left[\mathbf{X}_s^T \mathbf{Q} \mathbf{X}_s + \mathbf{U}^T \mathbf{R} \mathbf{U}\right] d\tau \tag{3.5}$$

The state weighting matrix $\mathbf{Q}$ and control weighting matrix $\mathbf{R}$ are obtained by directly constraining the output through the following relations:

$$\mathbf{Q} = \hat{\mathbf{C}}^T \hat{\mathbf{Q}} \hat{\mathbf{C}} \tag{3.6a}$$

$$\mathbf{R} = \hat{\mathbf{R}} + \hat{\mathbf{D}}^T \hat{\mathbf{Q}} \hat{\mathbf{D}} \tag{3.6b}$$

where $\hat{\mathbf{Q}}$ and $\hat{\mathbf{R}}$ are diagonal matrices. The diagonal elements of $\hat{\mathbf{Q}}$ and $\hat{\mathbf{R}}$ are formed by the penalties on the outputs and inputs, respectively:

$$\hat{\mathbf{Q}} = \text{diag}\left(\mathbf{w}_{\text{RB}}^T \ \mathbf{w}_{\text{PLL}}^T\right) \tag{3.7a}$$

$$\hat{\mathbf{R}} = \text{diag}\left(\mathbf{w}_U\right) \tag{3.7b}$$

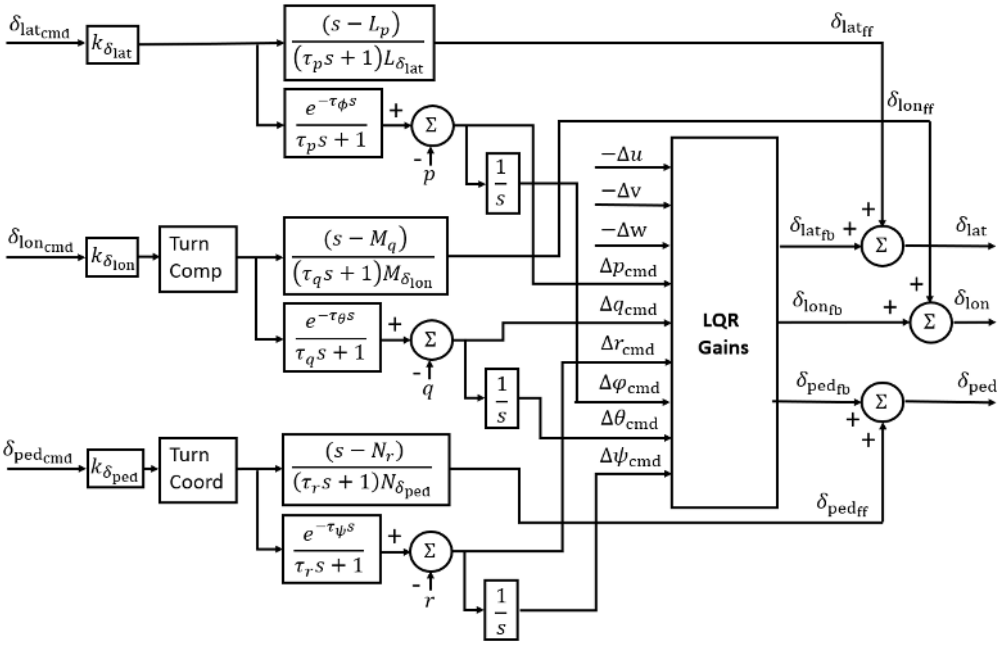

Figure 3.3: Block diagram for the rigid-body feedback controller (conventional helicopter).

where:

$\mathbf{w}_{\text{RB}}$ is the penalty vector on the rigid-body stetes,

$\mathbf{w}_{\text{PLL}}$ is the penalty vector on the pitch link load harmonics, and

$\mathbf{w}_U$ is the penalty vector on the controls.

Two feedback methods are used: rigid-body feedback and rotor state feedback. The rigid-body feedback employs the 9-state reduced-order model to derive the LQR gains. The LQR gains are, in this case, a 3-by-9 matrix. The method described allows to transfer the constraints on each harmonic of the pitch link load response to the rigid-body, effectively providing a load limiting control action based on the feedback of the 0^{th} harmonic rigid-body states. The block diagram for the rigid-body feedback controller is shown in Fig. 3.3.

The rotor state feedback employs the 11-state reduced-order model to derive the LQR gains. The LQR gains, in this case, are a 3-by-11 matrix. This method allows to transfer the constraints on each harmonic of the pitch link load response

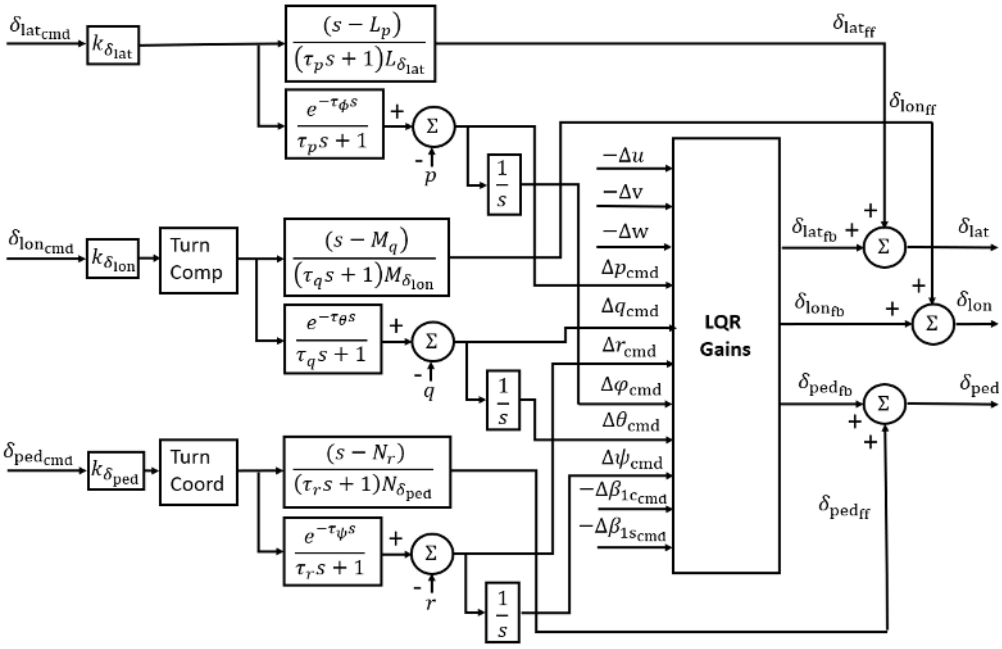

Figure 3.4: Block diagram for the rotor state feedback controller (conventional helicopter).

to the rigid-body and rotor states, effectively providing a load limiting control action based on the feedback of the 0^{th} harmonic rigid-body states and the longitudinal and lateral flapping states. The block diagram for the rotor state feedback controller is shown in Fig. 3.4.

Most notably, the controller minimizes rotor loads perturbations from their periodic equilibrium. It follows that this methodology is well suited for alleviating unsteady loads. However, it does not affect stationary (trim) loads.

3.2.3 Baseline Controller

3.2.4 CONDUIT® Overview

Given the multi-objective trade-offs associated with the handling qualities/flight control design specifications and performance metrics, flight control optimization can be very complex. Specifically, flight control design presents a highly non-

orthogonal and non-convex problem in numerical optimization. For this reason, automated optimization tools can play an important role. The Control Designer's Unified Interface (CONDUIT®) [59] was developed to provide a comprehensive analysis and optimization environment tool for flight control design and is built on top on the highly flexible MATLAB®/Simulink® system modeling and analysis environment [61]. It is jointly developed and supported by the U.S. Army Aviation Development Directorate (ADD) and Universities Space Research Association (USRA), both at Moffett Field, CA.

CONDUIT® uses feasible sequential programming (FSQP) to solve a min-max optimization of the vector of multiple objective functions (specifications). The FSQP algorithm is achieved by dividing the problem into three phases of optimization:

Phase 1 - Satisfying the hard constraints.

Phase 2 - Satisfying the soft constraints while not violating any hard constraints.

Phase 3 - Selecting the best solution from among the feasible sets that satisfy all of the hard and soft constraints.

The converged solution, at the completion of Phase 3, is the pareto optimum design that meets all the requirements with minimum control usage. The central requirement for automated design optimization is a capability to return numerical scores of system performance for a given set of design parameter values. The handling qualities/flight control specification boundaries that separate the Level 1 handling qualities region from the Level 2 handling qualities region, and the Level 2 handling qualities region from the Level 3 handling qualities region provide for a natural scoring system. With this scoring approach, there is no need for user-defined scaling beyond what is already provided by the Level 1/ Level 2 and Level 2/ Level 3 boundaries of the handling qualities criteria.

3.2.4.1 Rigid-Body Feedback

The LQR weights are optimized using the Control Designer's Unified Interface (CONDUIT®) and design methods of Ref. [59] to meet a comprehensive set of stability, handling qualities, and performance specifications. The specifications are drawn mostly from ADS-33E [2] handling qualities requirements for military rotorcraft, SAE-AS94900 [62] flight control system requirements for military aircraft, a set of other requirements developed at the U.S. Army Aviation Development Directorate (ADD) [59], and from some general well known control law requirements and logical objective functions. The various specifications that are used as constraints in the flight control optimization, and their origin, are listed below.

- *Eigenvalues* (generic) - Ensures that all closed-loop eigenvalues are in the left-hand side of the complex plane. For piloted rotorcraft, very low frequency poles in the right-hand side of the plane are allowed within a specified tolerance because the pilot can easily correct slow instabilities. The phugoid mode is typically associated with low-frequency unstable eigenvalues.

- *Damping Ratio* (ADS-33E) - Based on time response evaluation of damping characteristic for a pilot input in the roll, pitch, and yaw axes.

- *Model Following Accuracy* (ADD) - Mismatch cost function based on comparison of frequency responses for the command model and rotorcraft to ensure that satisfying model following is achieved.

- *Stability Robustness* (Ref. [63]) - Off-nominal conditions must maintain a stability margin in terms of Nichols margin exclusion zone.

- *Stability Margins* (SAE-AS94900) - Gain and phase margin requirements are imposed on the broken-loop frequency response.

- *Bandwidth and Phase Delay* (ADS-33E) - Short-term small-amplitude criterion that addresses the initial delay and the speed of the on-axis attitude

response to pilot stick inputs.

- *Disturbance Rejection Bandwidth and Peak* (ADD) - The disturbance rejection bandwidth (DRB) is analogous to the bandwidth of the controller but for a disturbance input in the attitude of the aircraft. The disturbance rejection peak (DRP) measures the maximum amplification of a disturbance input in the attitude of the aircraft.

- *Minimum Crossover Frequency* (generic) - Sets the minimum crossover frequency for the broken-loop response. It is desirable to minimize this quantity to reduce actuator activity. However, a lower boundary is set to guarantee satisfactory feedback system bandwidth.

- *Actuator Root Mean Square* (ADD) - The actuator Root Mean Square (RMS) for the closed-loop system is minimized for both pilot and disturbance inputs to the actuators.

The weights on the rigid-body states and controls are optimized whereas the weights on the pitch link load harmonics are set to zero and frozen during the optimization. The linear model used as the plant model for the optimization is the high-order LTI model previously derived. The controller thus obtained is referred to as the "Baseline Rigid-Body Feedback" controller, or "Baseline RBFB". The command filters properties for the baseline controller are found in Tables 3.3 and 3.4. The state and control penalties are reported in Tables 4.1 and 3.7, respectively. The comprehensive set of stability, handling qualities, and performance specifications for the baseline controller is shown in Fig. 3.5, along with its legend in Fig. 3.6. A definition of all specifications is provided in Table 3.5

3.2.4.2 Rotor State Feedback

Similarly to rigid-body feedback case, an optimization is run so that the controller with rotor state feedback meets the comprehensive set of stability, handling qual-

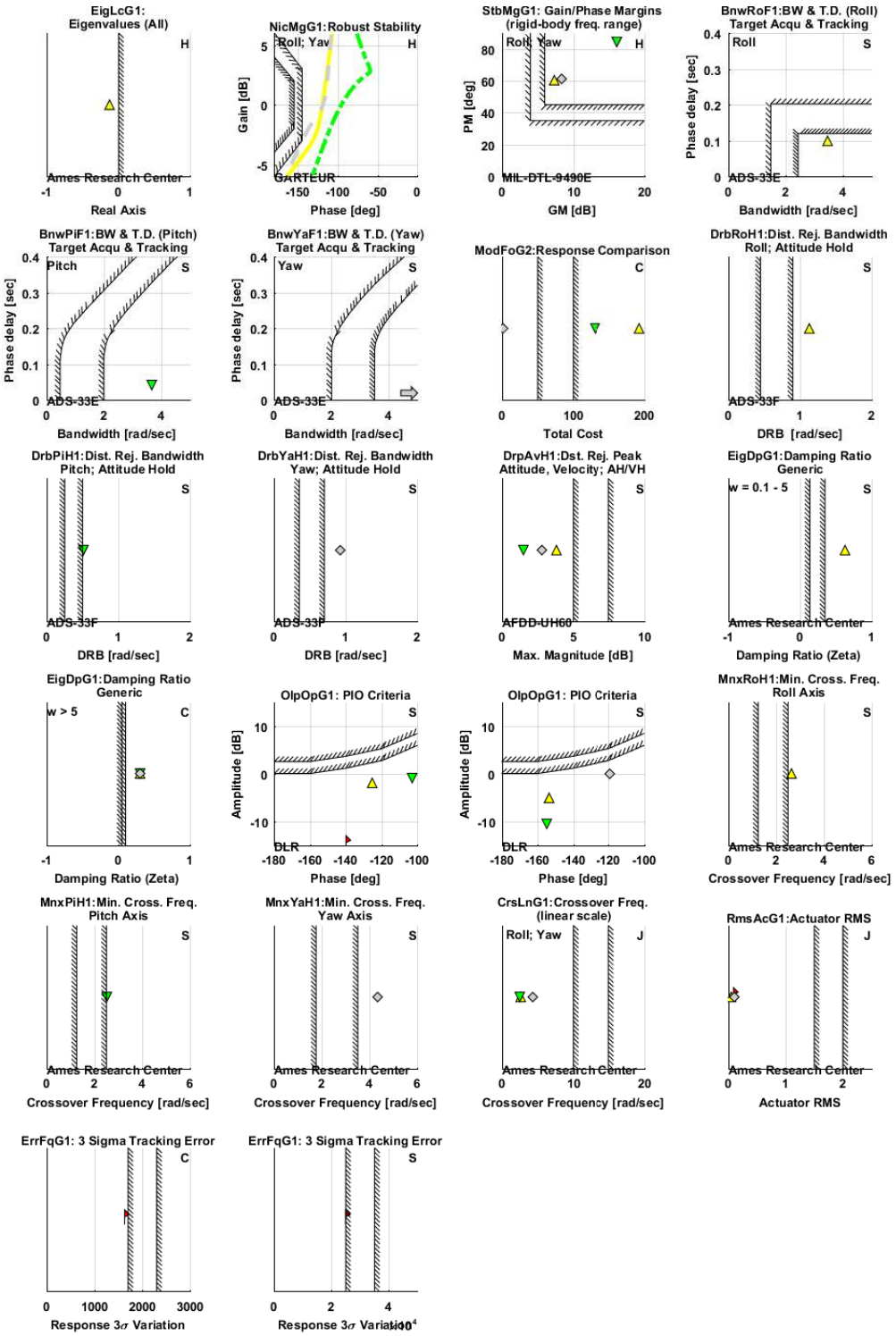

Figure 3.5: Set of stability, handling qualities, and performance specifications for the conventional helicopter employing the baseline RBFB controller.

Table 3.3: Command filter gains.

Parameter	Units	Value
$k_{\delta_{\text{lat}}}$	deg/(s-%)	0.90
$k_{\delta_{\text{lon}}}$	deg/(s-%)	0.45
$k_{\delta_{\text{ped}}}$	deg/(s-%)	36.9

Table 3.4: Baseline controller command filters break frequencies.

Parameter	Units	Value
ω_p	rad/s	3
ω_q	rad/s	4.5
ω_r	rad/s	2

ities, and performance specifications. The weights on the rigid-body states, rotor states, and controls are optimized, whereas the weights on the pitch link load harmonics are set to zero and frozen during the optimization. The linear model used as the plant model for the optimization is the high-order LTI model previously derived. The controller thus obtained is referred to as the "Baseline Rotor State Feedback" controller, or "Baseline RSFB". The command filters are the same as for the rigid-body state controller. The state and control penalties are reported in Tables 4.1 and 3.7, respectively. The comprehensive set of stability, handling qualities, and performance specifications for the baseline RSFB controller is shown in Fig. 3.7.

3.3 Compound Rotorcraft Controller

3.3.1 Feed-Forward Compensation

The controller for the compound rotorcraft is designed to achieve stability and desired rate-command/attitude-hold (RCAH) response around the roll, pitch and yaw axes. The heave axis is left open-loop. Since the axes that are being con-

Table 3.5: Control system optimization specifications.

Spec Name	Description	Axis	Source
	Hard Constraints (Stability Requirements)		
EigLcG1	Eigenvalues in left half-plane (L.H.P.)	All	Generic
StbMgG1	Gain Phase Margin broken at actuator	All	AS94900
NicMgG1	Nichols Margins broken at actuator	All	GARTEUR
	Soft Constraints (Handling Qualities Requirements)		
BnwRoF1	Roll attitude bandwidth and phase delay	Roll	ADS-33E
BnwPiF1	Pitch attitude bandwidth and phase delay	Pitch	ADS-33E
BnwYaF1	Yaw attitude bandwidth and phase delay	Yaw	ADS-33E
DrbRoH1	Roll attitude disturbance rejection bandwidth	Roll	ADD
DrbPiH1	Pitch attitude disturbance rejection bandwidth	Pitch	ADD
DrbYaH1	Yaw attitude disturbance rejection bandwidth	Yaw	ADD
BrpAvH1	Roll/Pitch/Yaw attitude disturbance rejection peak	All	ADD
EigDpG1	Eigenvalue damping ($0.1 < \omega < 0.5$ rad/s)	All	Generic
EigDpG1	Eigenvalue damping ($\omega > 0.5$ rad/s)	All	Generic
OlpOpG1	Open loop onset point, pilot input	All	DLR
OlpOpG1	Open loop onset point, disturbance input	All	DLR
MnxRoH1	Minimum crossover frequency of roll broken loop response	Roll	ADD
MnxPiH1	Minimum crossover frequency of pitch broken loop response	Pitch	ADD
MnxYaH1	Minimum crossover frequency of yaw broken loop response	Yaw	ADD
	Summed Objectives (Performance Requirements)		
CrsLnG1	Crossover frequency	All	Generic
RmsAcG1	Actuator root mean square (RMS)	All	Generic
	Check Only		
ModFoG2	Command model following cost	All	Generic
ErrFqG1	3σ tracking error of pitch link load, roll rate disturbance input	Roll	Generic
ErrFqG1	3σ tracking error of pitch link load, pitch rate disturbance input	Pitch	Generic

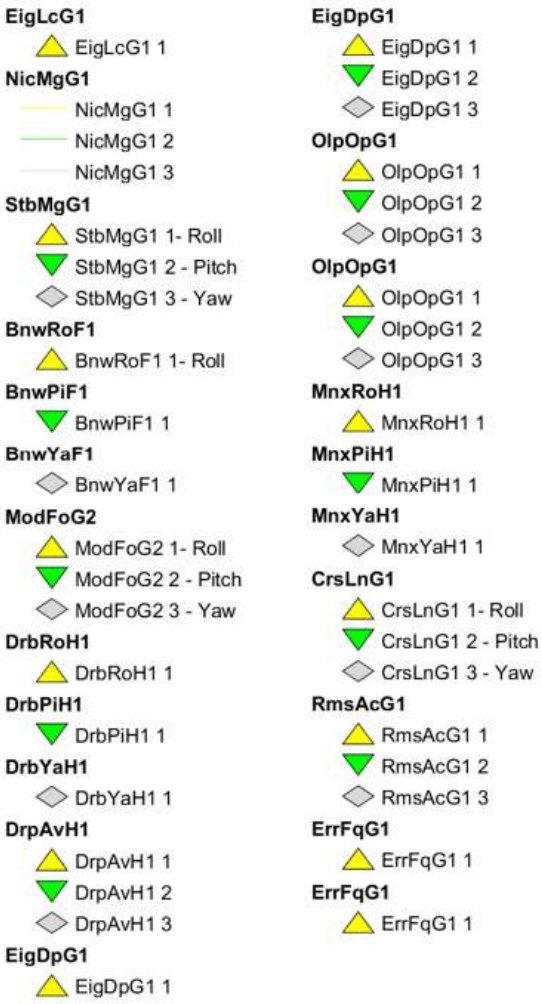

Figure 3.6: Legend for the set of stability, handling qualities, and performance specifications (arrows indicate points that are off the scale of the chart).

trolled are three but the total control effectors are six, the system is over-actuated. Consider the compound model input vector:

$$\mathbf{U} = \left[\delta_{\text{lat}}\ \delta_{\text{lon}}\ \delta_{\text{ped}}\ \delta_{\text{sym}}\ \delta_{\text{dif}}\ \delta_{\text{stb}}\right] \tag{3.8}$$

Allocation of the feed-forward control action to the redundant control effectors is obtained by a pseudo-inverse strategy, as described in [64]. The state equation is

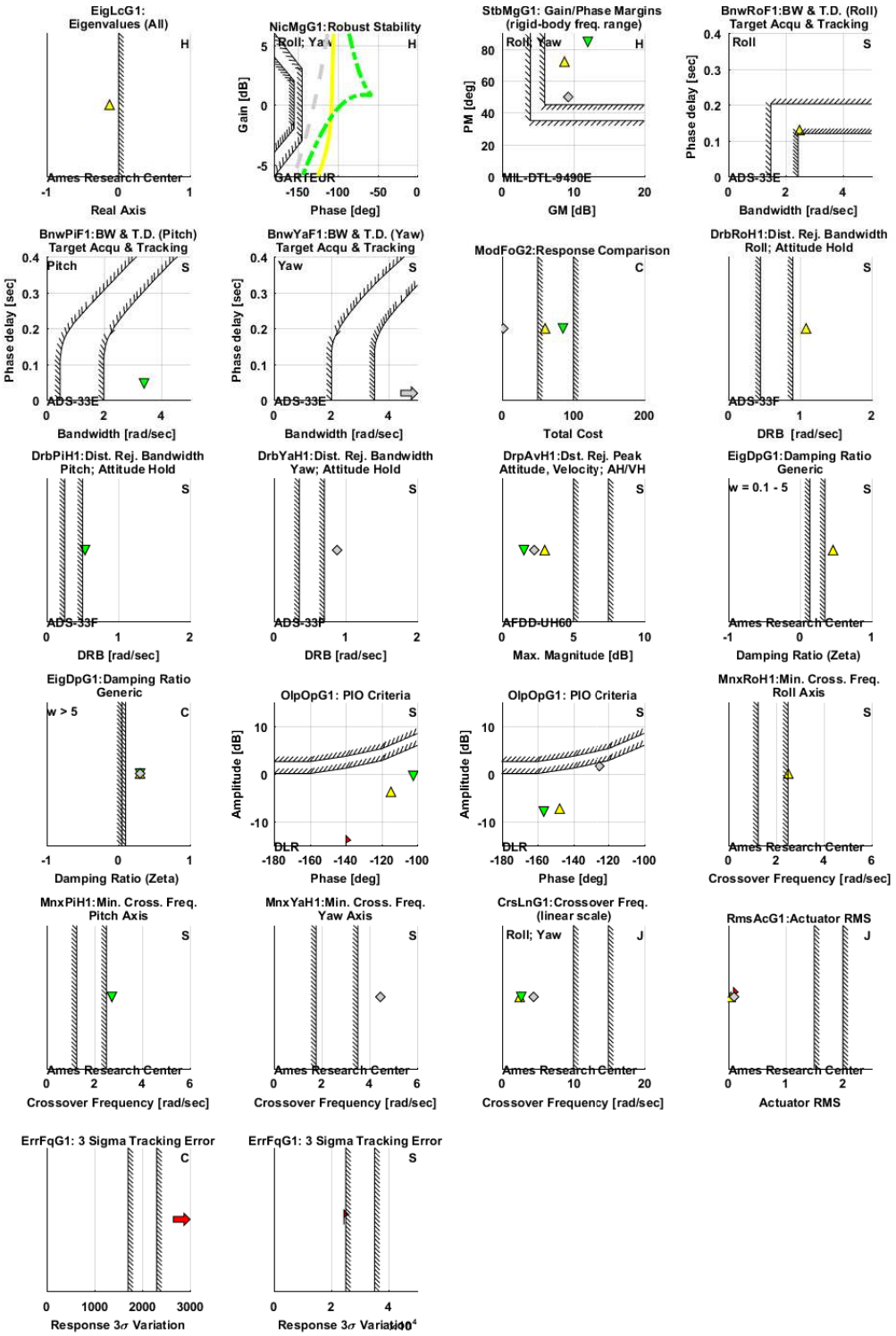

Figure 3.7: Set of stability, handling qualities, and performance specifications for the conventional helicopter employing the baseline RSFB controller.

Table 3.6: Conventional helicopter baseline controller weights on the diagonal elements of $\hat{\mathbf{Q}}$.

Parameter	Units	RBFB	RSFB
u	ft/s	0	0
v	ft/s	0	0
w	ft/s	0	0
p	rad/s	1.0828e+2	7.2244e+1
q	rad/s	3.8252e+2	3.8028e+2
r	rad/s	2.0207e+1	4.6778e+1
ϕ	rad	6.2138e+2	6.3637e+2
θ	rad	1.9255e+2	1.9195e+2
ψ	rad	2.9349e+2	3.0897e+2
β_{1c}	rad	-	1.2958e−4
β_{1s}	rad	-	1.2823e−4
PLL_0	lbs	0	0
PLL_{1c}	lbs	0	0
PLL_{1s}	lbs	0	0
PLL_{2c}	lbs	0	0
PLL_{2c}	lbs	0	0
PLL_{3c}	lbs	0	0
PLL_{3s}	lbs	0	0
PLL_{4c}	lbs	0	0
PLL_{4s}	lbs	0	0

Table 3.7: Conventional helicopter baseline controller weights on the diagonal elements of $\hat{\mathbf{R}}$.

Parameter	Units	RBFB	RSFB
δ_{lat}	%	7.6736e−2	7.4672e−2
δ_{lon}	%	3.7561e−2	3.7876e−2
δ_{ped}	%	3.0299e−1	3.0314e−1

re-written as:

$$\begin{aligned}\dot{\hat{\mathbf{X}}}_s &= \hat{\mathbf{A}}\hat{\mathbf{X}}_s + \hat{\mathbf{B}}\mathbf{U} \\ &= \hat{\mathbf{A}}\hat{\mathbf{X}}_s + \hat{\mathbf{B}}\mathbf{G}\mathbf{d} \\ &= \hat{\mathbf{A}}\hat{\mathbf{X}}_s + \tilde{\mathbf{B}}\mathbf{d}\end{aligned} \tag{3.9}$$

where $\mathbf{d}$ is the pseudo control vector, with one control per controlled axis, and $\mathbf{G}$ is the ganging matrix. The pseudo control vector is:

$$\mathbf{d}^T = \begin{bmatrix} \delta_{\text{lat}} & \delta_{\text{lon}} & \delta_{\text{ped}} \end{bmatrix} \tag{3.10}$$

The ganging matrix a 6-by-3 matrix and is defined by:

$$\mathbf{G} = \mathbf{W}^{-1}\mathbf{B}_r^T(\mathbf{B}_r\mathbf{W}^{-1}\mathbf{B}_r^T)^{-1} \tag{3.11}$$

where $\mathbf{B}_r$ is a 3-by-6 matrix of which the rows corresponding to the axes that are being controlled, $\dot{p}$, $\dot{q}$, and $\dot{r}$, are pulled from $\hat{\mathbf{B}}$, and $\mathbf{W}$ is a weighting matrix used to place different cost weightings on certain effectors. Note that $\mathbf{W}$ is a diagonal a 6-by-6 identity matrix. In case all the control effectors are expressed using the same units, and all the control effectors are given the same importance, the gangin matrix will be an identity matrix. Further, the feed-forward is now designed pulling the control derivatives from $\tilde{\mathbf{B}}$, rather than from $\hat{\mathbf{B}}$. For this reason, the inverse plant changes and is approximated by the following set of decoupled 1^{st} order transfer functions:

$$\frac{p_{\text{cmd}}}{\delta_{\text{lat}_{\text{ff}}}}(s) = \frac{1}{s - L_p} \tag{3.12a}$$

$$\frac{q_{\text{cmd}}}{\delta_{\text{lon}_{\text{ff}}}}(s) = \frac{1}{s - M_q} \tag{3.12b}$$

$$\frac{r_{\text{cmd}}}{\delta_{\text{ped}_{\text{ff}}}}(s) = \frac{1}{s - N_r} \tag{3.12c}$$

3.3.2 Feedback Compensation

The linear quadratic regulator is used to re-allocate the control signal to the redundant control effectors in the feedback path. Similarly to the conventional helicopter

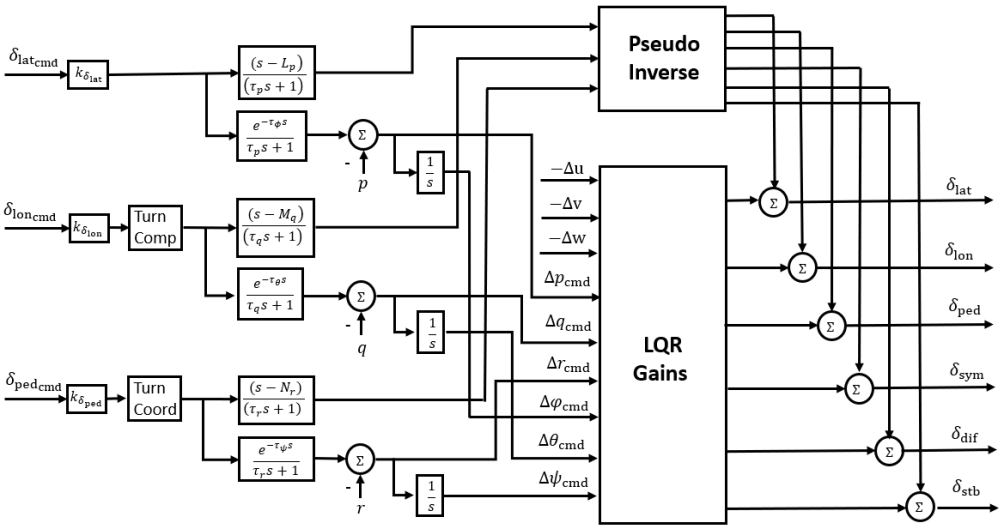

Figure 3.8: Block diagram for the rigid-body feedback controller (compound rotorcraft).

case, the cost function that is minimized is:

$$J = \int_0^t \left[\mathbf{X}_s^T \mathbf{Q} \mathbf{X}_s + \mathbf{U}^T \mathbf{R} \mathbf{U}\right] d\tau \tag{3.13}$$

but the control vector utilized is:

$$\mathbf{U} = \left[\delta_{\text{lat}} \ \delta_{\text{lon}} \ \delta_{\text{ped}} \ \delta_{\text{sym}} \ \delta_{\text{dif}} \ \delta_{\text{stb}}\right] \tag{3.14}$$

The LQR gains are a 6-by-9 matrix for the rigid-body feedback case, and a 6-by-11 matrix for the rotor state feedback case. The block diagram for the rigid-body feedback controller is shown in Fig. 3.8. The block diagram for the rotor state feedback controller is shown in Fig. 3.9.

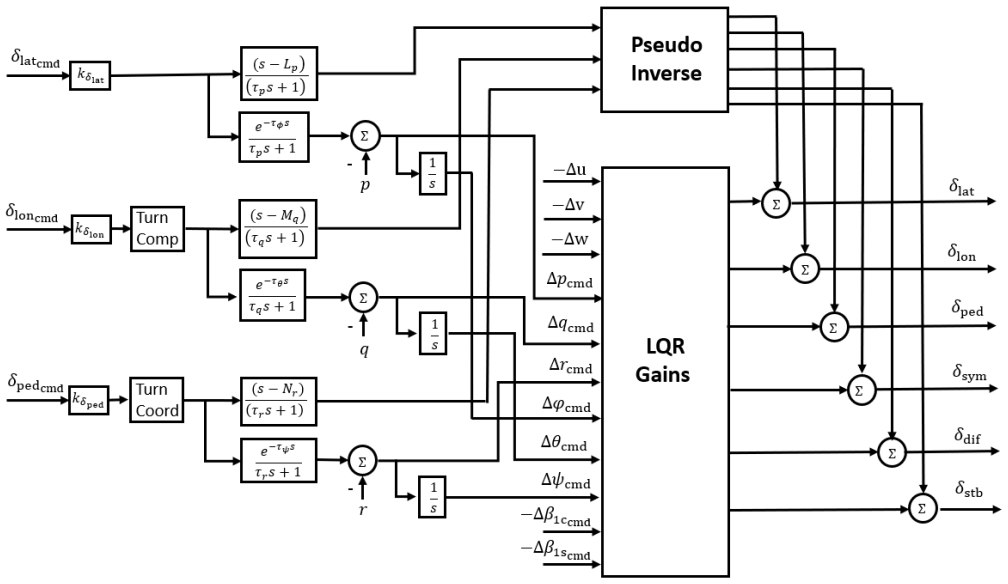

Figure 3.9: Block diagram for the rotor state feedback controller (compound rotorcraft).

3.3.3 Baseline Controller

3.3.3.1 Rigid-Body Feedback

An optimization is run so that the controller with rigid-body feedback meets the comprehensive set of stability, handling qualities, and performance specifications. The weights on the rigid-body states and redundant controls are optimized, whereas the weights on the pitch link load harmonics are set to zero and frozen during the optimization. The linear model used as the plant model for the optimization is the high-order LTI model previously derived. The controller thus obtained is referred to as the "Baseline Compound Rigid-Body Feedback" controller, or "Baseline Compound RBFB". The command filters are the same as for the conventional helicopter. The state and control penalties are reported in Tables 3.8 and 3.9, respectively. The comprehensive set of stability, handling qualities, and performance specifications for the baseline compound RBFB controller is shown in Fig. 3.11.

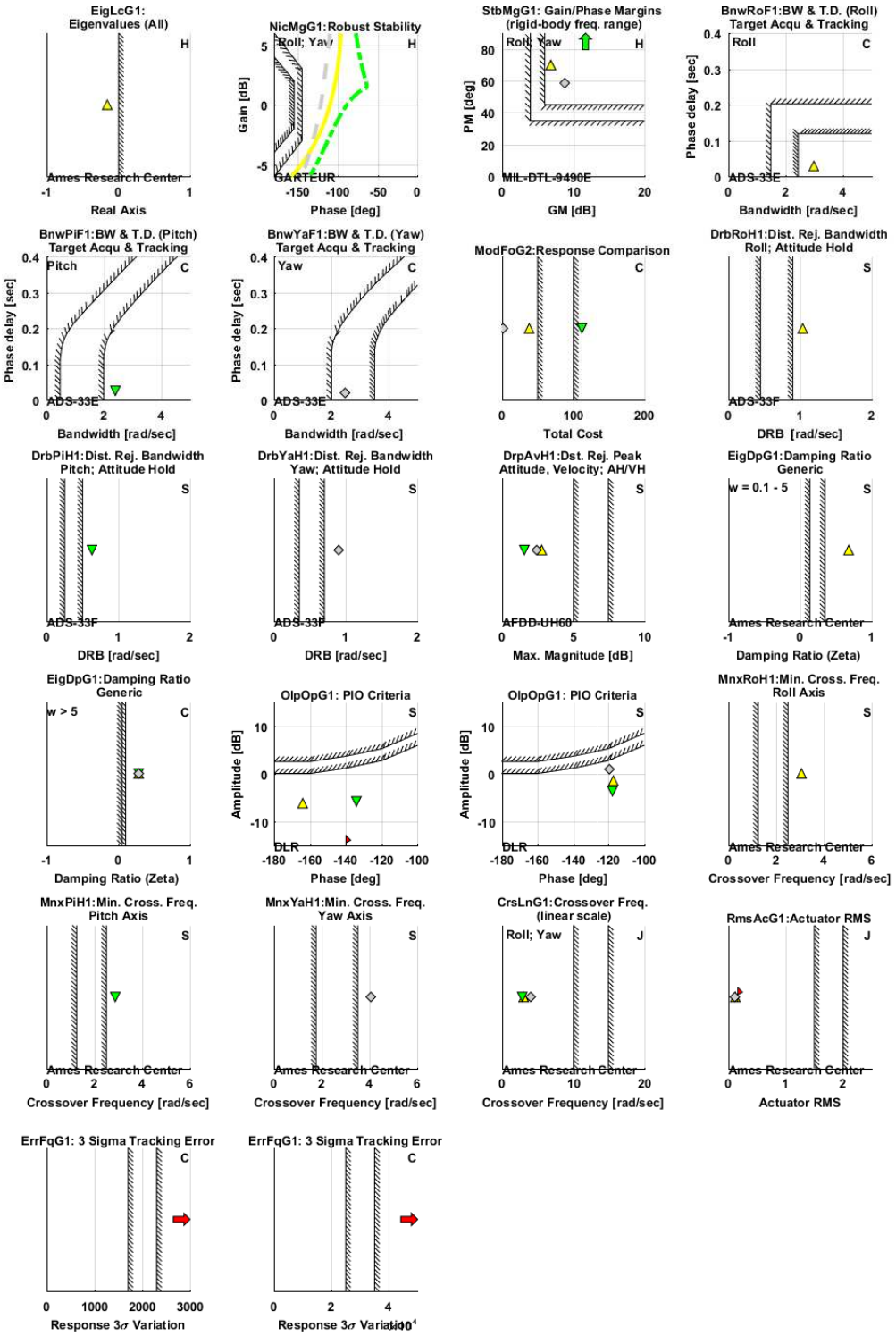

Figure 3.10: Set of stability, handling qualities, and performance specifications for the compound rotorcraft employing the baseline RBFB controller.

3.3.3.2 Rotor State Feedback

An optimization is run so that the controller with rotor state feedback meets the comprehensive set of stability, handling qualities, and performance specifications. The weights on the rigid-body states, rotor states, and redundant controls are optimized, whereas the weights on the pitch link load harmonics are set to zero and frozen during the optimization. The linear model used as the plant model for the optimization is the high-order LTI model previously derived. The controller thus obtained is referred to as the "Baseline Compound Rotor State Feedback" controller, or "Baseline Compound RSFB". The command filters are the same as for the conventional helicopter. The state and control penalties are reported in Tables 3.8 and 3.9, respectively. The comprehensive set of stability, handling qualities, and performance specifications for the baseline compound RSFB controller is shown in Fig. 3.11.

Table 3.8: Compound rotorcraft baseline controller weights on the diagonal elements of $\hat{\mathbf{Q}}$.

Parameter	Units	RBFB	RSFB
u	ft/s	0	0
v	ft/s	0	0
w	ft/s	0	0
p	rad/s	3.9309e+2	3.1491e+2
q	rad/s	5.0699e+2	5.2283e+2
r	rad/s	7.4052e+1	2.6814e+1
ϕ	rad	1.1361e+3	1.1628e+3
θ	rad	5.1839e+2	5.2619e+2
ψ	rad	2.7528e+2	2.6349e+2
β_{1c}	rad	-	0
β_{1s}	rad	-	0
PLL_0	lbs	0	0
PLL_{1c}	lbs	0	0
PLL_{1s}	lbs	0	0
PLL_{2c}	lbs	0	0
PLL_{2c}	lbs	0	0
PLL_{3c}	lbs	0	0
PLL_{3s}	lbs	0	0
PLL_{4c}	lbs	0	0
PLL_{4s}	lbs	0	0

Table 3.9: Compound rotorcraft baseline controller weights on the diagonal elements of $\hat{\mathbf{R}}$.

Parameter	Units	RBFB	RSFB
δ_{lat}	%	2.4624e−2	2.8239e−2
δ_{lon}	%	2.1000e−2	1.7117e−2
δ_{ped}	%	3.0161e−1	3.0182e−1
δ_{sym}	%	1.0001e+2	1.0001e+2
δ_{dif}	%	1.1309e+2	1.1233e+2
δ_{stb}	%	1.0064e+2	1.0068e+1

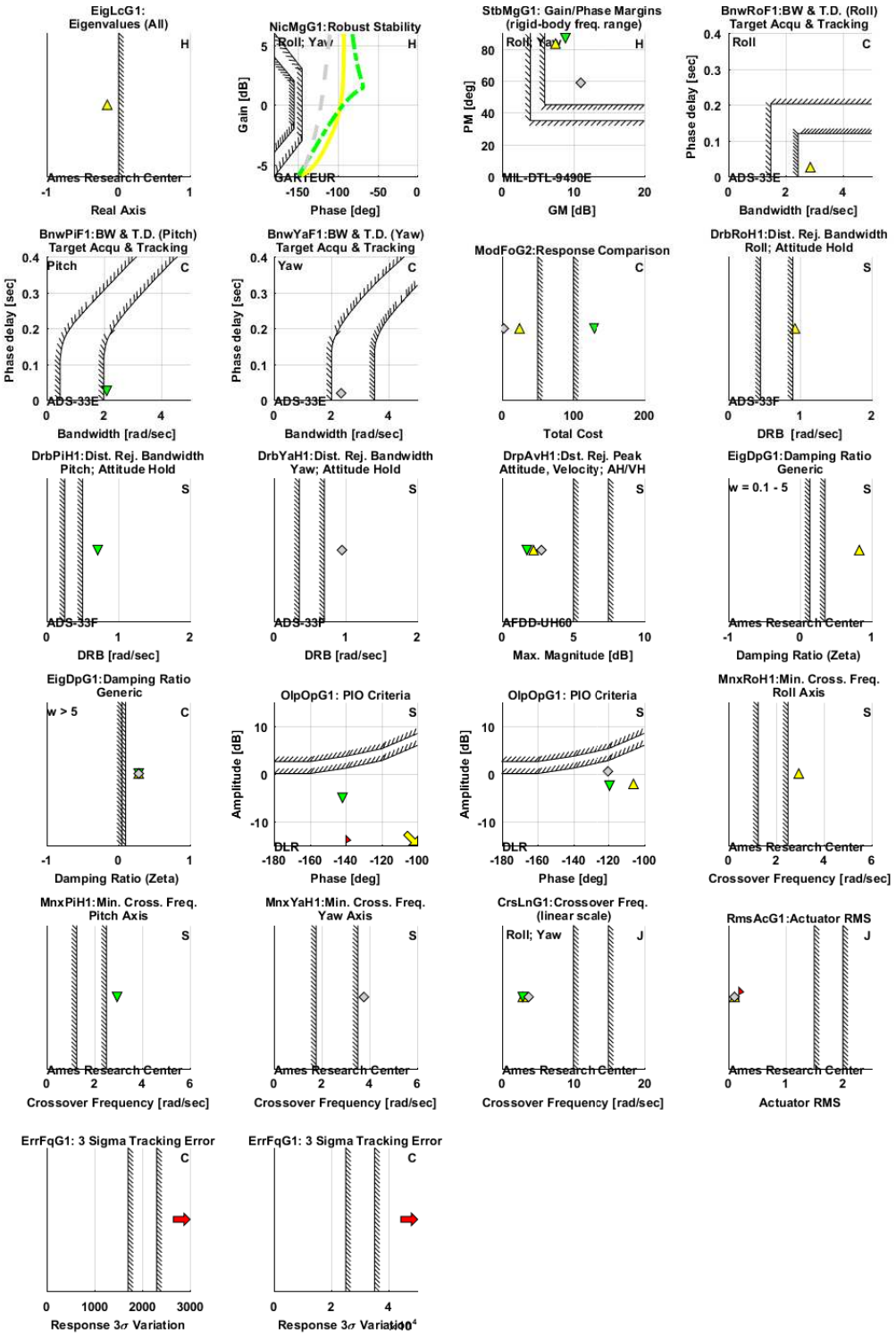

Figure 3.11: Set of stability, handling qualities, and performance specifications for the compound rotorcraft employing the baseline RSFB controller.

Chapter 4

Alleviation of Unsteady Rotor Loads

4.1 Parametric Study

This section analyzes how the feed-forward and feedback paths of the controller can be used towards load alleviation. Specifically, command model tailoring is examined for the feed-forward path, whereas tailoring of the LQR weights on the pitch link load harmonics is explored for the feedback path. The impact of these two strategies on the handling qualities is also studied.

Next, the closed-loop frequency responses of the pitch link load to the commanded angular rates are computed, as shown in Fig. 4.1. This is done to understand the sensitivity of the rotor loads to pilot commands. Commanded angular rates are chosen in favor of pilot stick commands as they share common units (rad/s). Results are presented to cover the typical frequency range of operation for flight control systems (1-60 rad/s). It appears that the rotor loads are mostly affected by the pitch rate command in this particular flight condition (dashed blue line in Fig. 4.1). Commanded roll rate is shown to impact the rotor loads more than the commanded yaw rate, especially at frequencies higher than 10 rad/s. The parametric study that follows will therefore concentrate on the roll and pitch axes.

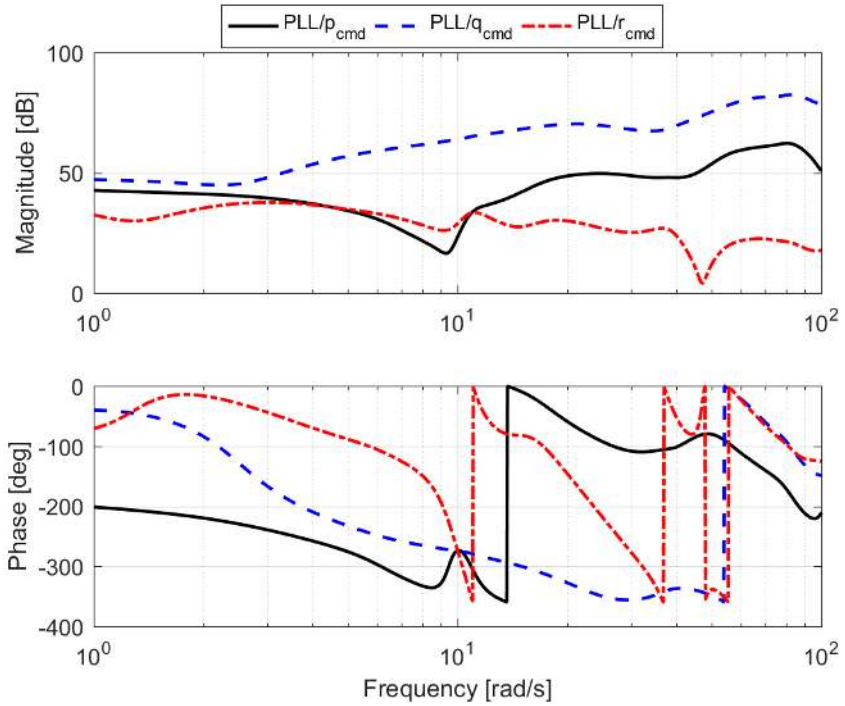

Figure 4.1: Closed-loop frequency response of the the pitch link load to the commanded angular rates.

4.1.1 Command Model Tailoring

Command filter break frequencies of the baseline controller are varied separately for the roll and pitch axes. Figure 4.2 shows the closed-loop pitch rate and pitch attitude responses to a longitudinal stick doublet for varying command filter break frequencies. Decreasing command filter break frequencies correspond to decreasing pitch accelerations. Decreasing pitch accelerations result in decreasing peak-to-peak pitch link loads, as shown in Fig. 4.3. A running mean is obtained by taking the sum of each pair of maximum and minimum peaks for each cycle (revolution) and dividing by two. The curves that are plotted are the maximum and minimum peaks minus the median. It is concluded that command model tailoring effectively provides load alleviation by limiting the commanded angular acceleration.

Figure 4.4 shows the bandwidth and phase delay for varying command filter break frequencies. The bandwidth and phase delay specifications for forward flight

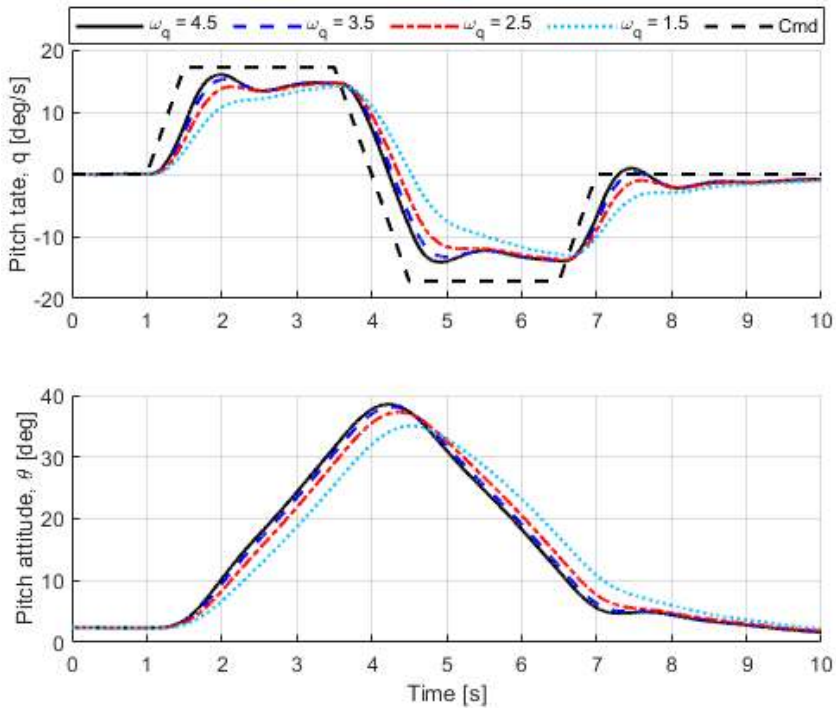

Figure 4.2: Closed-loop pitch rate and pitch attitude responses to a longitudinal stick doublet for varying command filter break frequencies.

(target acquisition and tracking) are also reported on the plot [2]. For the roll axis, decreasing command filter break frequencies result in decreasing bandwidth. For the pitch axis, decreasing command filter break frequencies result in decreasing bandwidth and increasing phase delay. In general, decreasing command filter break frequencies appear to negatively impact the handling qualities. It is concluded that load alleviation through feed-forward compensation is effective in providing alleviation of the rotor loads. However, it comes at the cost of a degradation in the handling qualities.

4.1.2 LQR Weighting Tailoring

4.1.2.1 Rigid-Body Feedback

Starting from the Baseline RBFB controller, the LQR weights on the rigid-body states and controls are frozen while the weights on the pitch link load harmonics

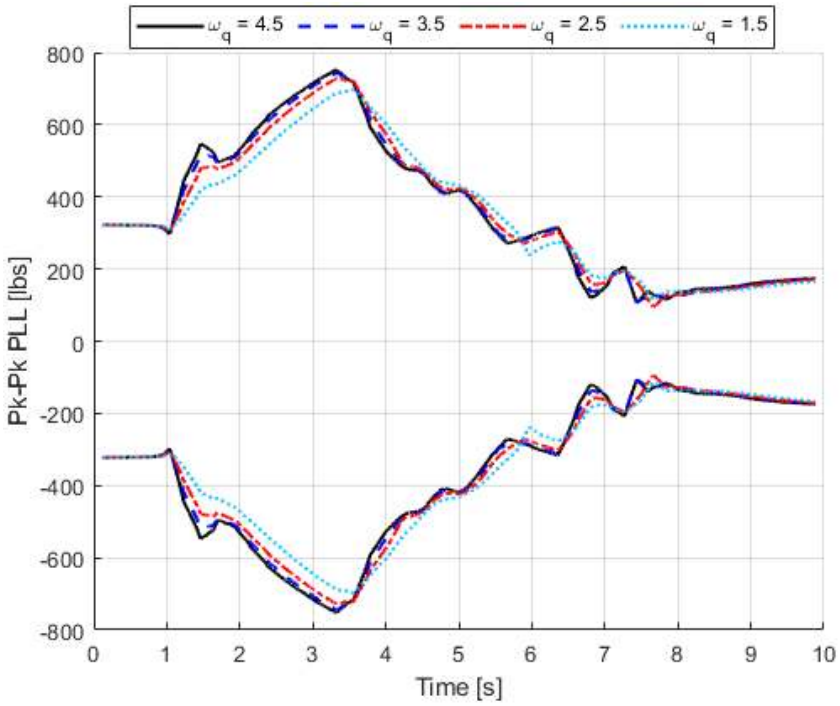

Figure 4.3: Closed-loop peak-to-peak pitch link load response to a longitudinal stick doublet for varying command filter break frequencies.

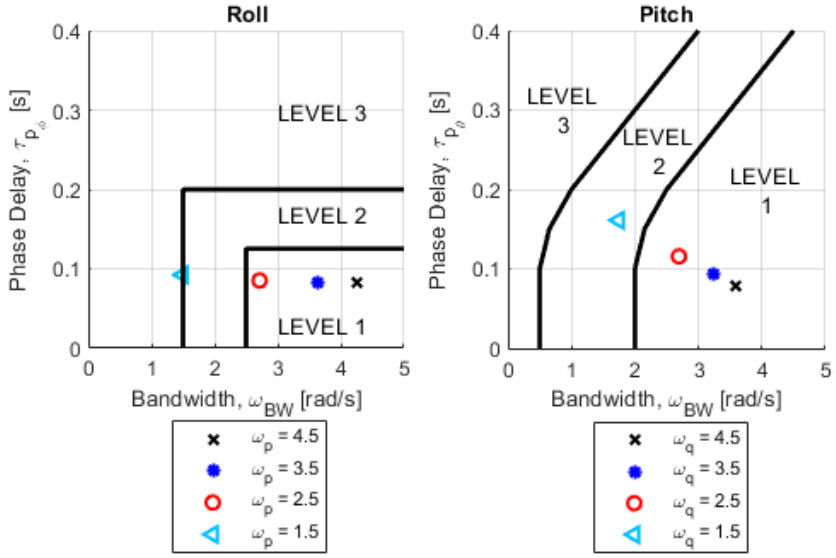

Figure 4.4: Bandwidth and phase delay specifications for varying command filter break frequencies.

are varied to generate a set of LQR feedback gain matrices. Figure 4.5 provides an insight on how the weights on the pitch link load harmonics $\mathbf{w}_{\mathrm{PLL}}$ affect the rigid-body weights in the state penalty matrix $\mathbf{Q}$. Only the diagonal terms of the state penalty matrix are shown. It is evident that constraining the pitch link load harmonics leads to increased constraints on the roll and pitch rates. The pitch rate is most affected by the 1^{st} and 2^{nd} cosine harmonics. The roll rate is most affected by the 1^{st}, 2^{nd}, and 4^{th} sine harmonics. In general, the pitch rate is affected more severely than the roll rate. This is expected and is due to the increased sensitivity of pitch link load to pitch rate, as compared to pitch link load to roll rate (Fig. 4.1). Both weights on the body velocities and the Euler angles are unaffected. Figure 4.6 provides an insight on how the weights on the pitch link load harmonics in the output penalty matrix $\mathbf{w}_{\mathrm{PLL}}$ affect the weights on the controls in the controls penalty matrix $\mathbf{R}$. Only the diagonal terms of the controls penalty matrix are shown. Constraining the pitch link load harmonics leads to increased penalties mostly on the longitudinal stick. The 0^{th} and 1^{st} harmonics are the major contributors.

Figure 4.7 provides insight on how the weights on the pitch link load harmonics in the output penalty matrix $\mathbf{w}_{\mathrm{PLL}}$ affect the LQR feedback gains. Only the on-axis gains are shown. Increasing penalties on the pitch link load harmonics leads to decreasing LQR on-axis gains. This is particularly evident for the gains relating the longitudinal stick with pitch attitude and pitch rate. Although not shown in the plot, the gains relating the body velocities with the controls are largely unaffected. These findings indicate that increasing load alleviation leads to decreasing pitch axis performance.

Controllers with increasing weights on the pitch link load harmonics are compared to assess the impact on handling qualities and controller performance. Figure 4.8 shows the gain and phase margins of the broken-loop response for increasing LQR weights on the pitch link load harmonics. The stability margin requirements

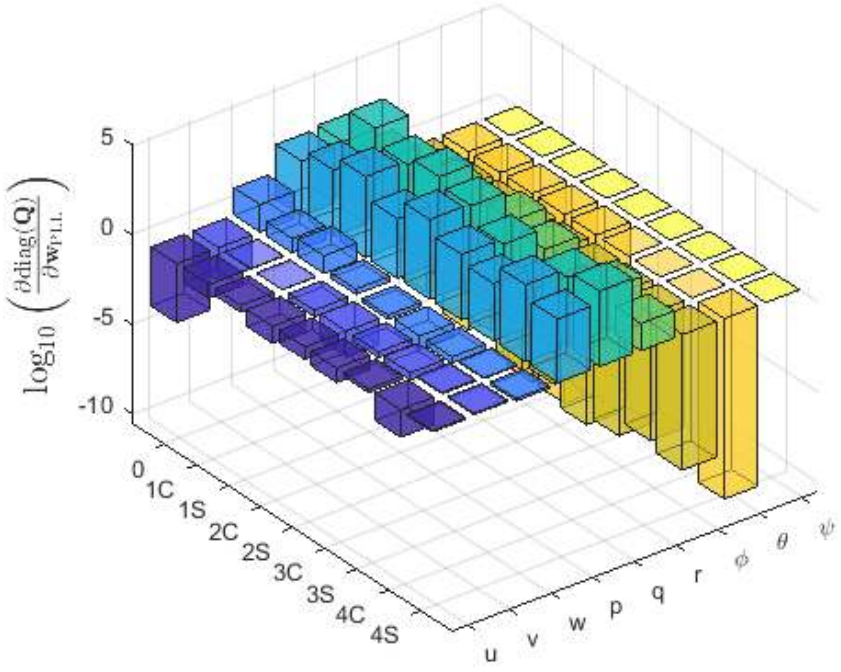

Figure 4.5: Gradient of the diagonal terms of the states penalty matrix with respect to the weights on the pitch link load harmonics.

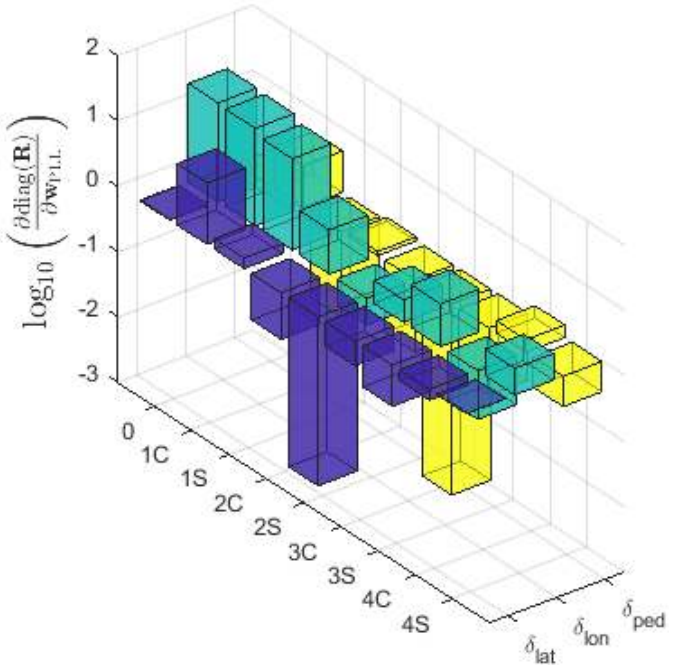

Figure 4.6: Gradient of the diagonal terms of the of the controls penalty matrix with respect to the weights on the pitch link load harmonics.

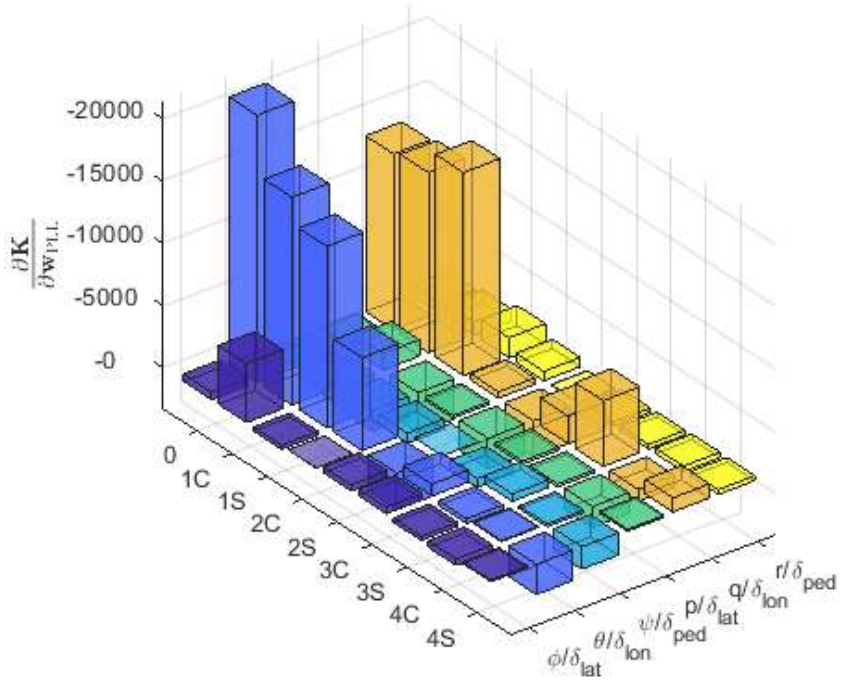

Figure 4.7: Gradient of the on-axis LQR gains with respect to the weights on the pitch link load harmonics.

defined in SAE-AS94900 are reproduced in the plot [62]. Most notably, the roll axis gain and phase margins appear nearly unaffected; however, the pitch axis gain margin increases with increasing weights. This is better explained by looking at the crossover frequency, shown in Fig. 4.9. The pitch axis crossover frequency rapidly decreases with increasing weights. Although this leads to a higher gain margin, it effectively results in an unsatisfactory minimum crossover frequency [59]. The high sensitivity of the crossover frequency to increasing LQR weights on the pitch link load harmonics constitutes a severe limitation in the achievable load alleviation.

Next, bandwidth and phase delay for increasing weights on the pitch link load harmonics are shown in Fig. 4.10. The bandwidth and phase delay specifications for forward flight (target acquisition and tracking) are also reported on the plot [2]. The roll axis bandwidth and phase delay do not appear to be particularly affected. However, the pitch axis phase delay decreases with increasing weights.

Figure 4.11 show the disturbance rejection bandwidth (DRB) and peak (DRP)

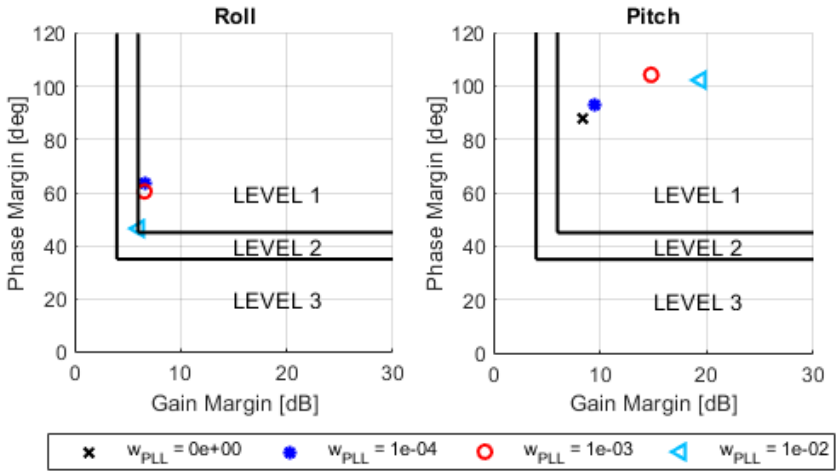

Figure 4.8: Stability margins for varying LQR weights on the pitch link load harmonics.

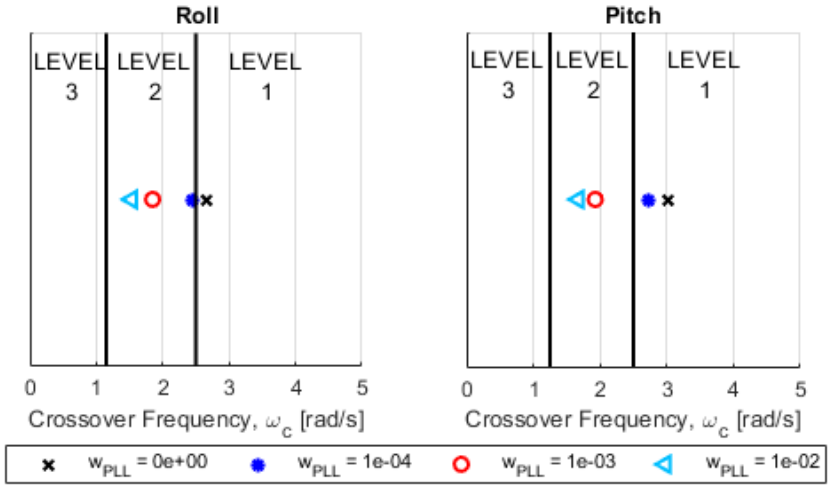

Figure 4.9: Crossover frequencies for varying LQR weights on the pitch link load harmonics.

for increasing LQR weights on the pitch link load harmonics. Similarly to the trend seen for crossover frequency, the DRB and DRP specifications are taken from [65] and reproduced on the plot. The DRB appears to decreases with increasing weights on both roll and pitch axes. This leads to a degradation of handling qualities in the pitch axis for low weights. This poses another possible limitation in achievable load alleviation.

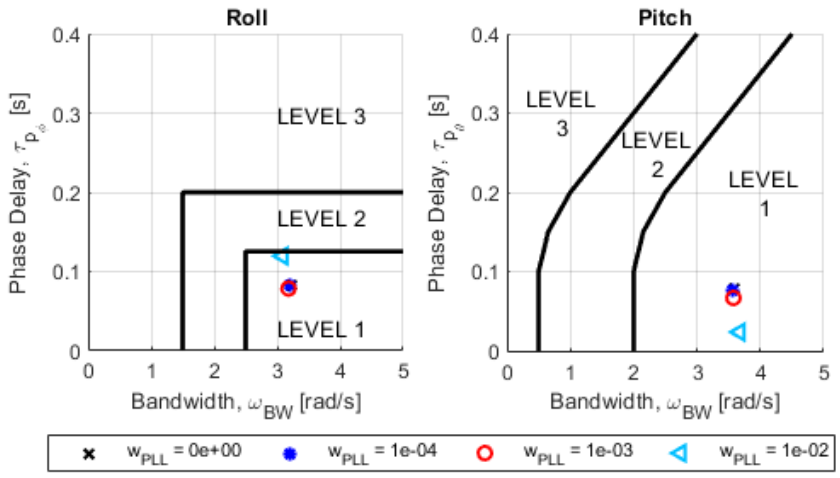

Figure 4.10: Bandwidth and phase delay specifications for varying LQR weights on the pitch link load harmonics.

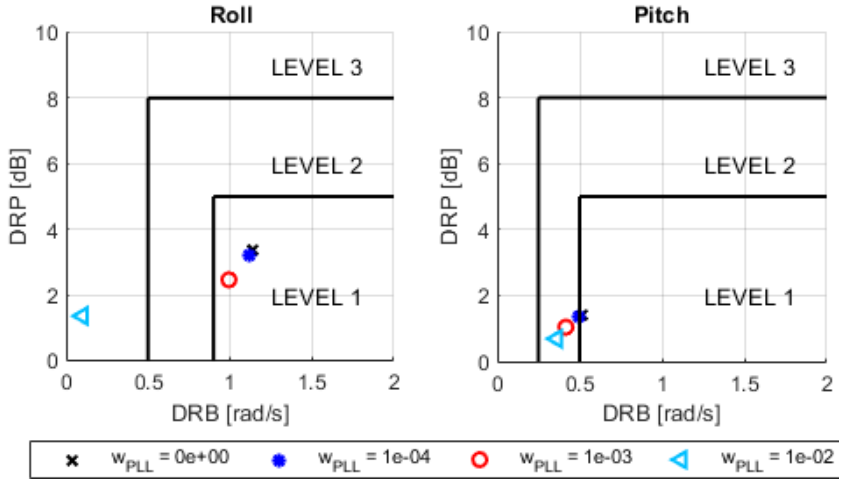

Figure 4.11: Disturbance rejection bandwidth (DRB) and peak (DRP) for varying LQR weights on the pitch link load harmonics.

The observations made for the handling qualities specifications in the frequency domain are reflected in time-domain simulations. The closed-loop response to a longitudinal stick doublet input is obtained for the different controllers, as shown in Fig. 4.12. It is apparent that increasing LQR weights on the pitch link harmonics effectively limits the pitch rate response, which substantiates the findings in [66]. Figure 4.13 shows the resulting load alleviation in terms of peak-to-peak pitch link load. Since satisfactory minimum crossover frequency and DRB for the pitch

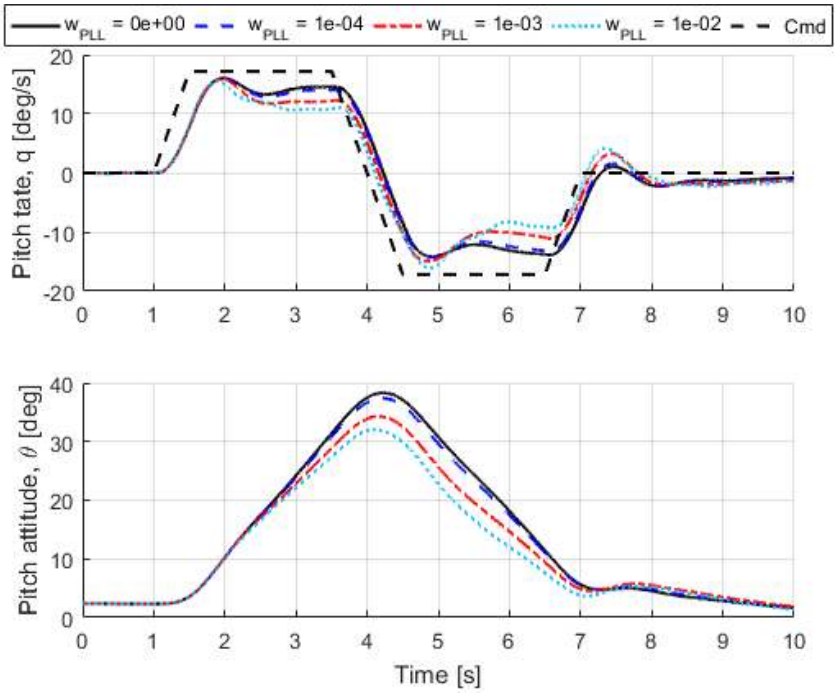

Figure 4.12: Closed-loop angular response to a longitudinal stick doublet.

axis are obtained for minimum LQR weights on the pitch link load harmonics ($\mathbf{w}_{\text{PLL}} = 1\text{e}^{-4}$), the maximum achievable load alleviation for the utility helicopter configuration is very modest, at least for the baseline controller that was derived.

This finding is further substantiated by the frequency response from a disturbance in the pitch rate to the pitch link load, as shown in Fig. 4.14. This particular response is chosen because, as opposed to the response from longitudinal stick to pitch link load, it is more representative of the feedback action only of the controller. Since flight control systems generally operate in a frequency range of about 1-60 rad/s, considerations are made based on that window. Indeed, the magnitude of the response decreases for increasing LQR weights on the pitch link load harmonics. However, weights of $\mathbf{w}_{\text{PLL}} = 1\text{e}^{-4}$ lead to a very modest reduction. Considering the frequency response from a disturbance in roll rate to the pitch link load, it is also observed that increasing LQR weights on the pitch link load harmonics do not result in any load alleviation.

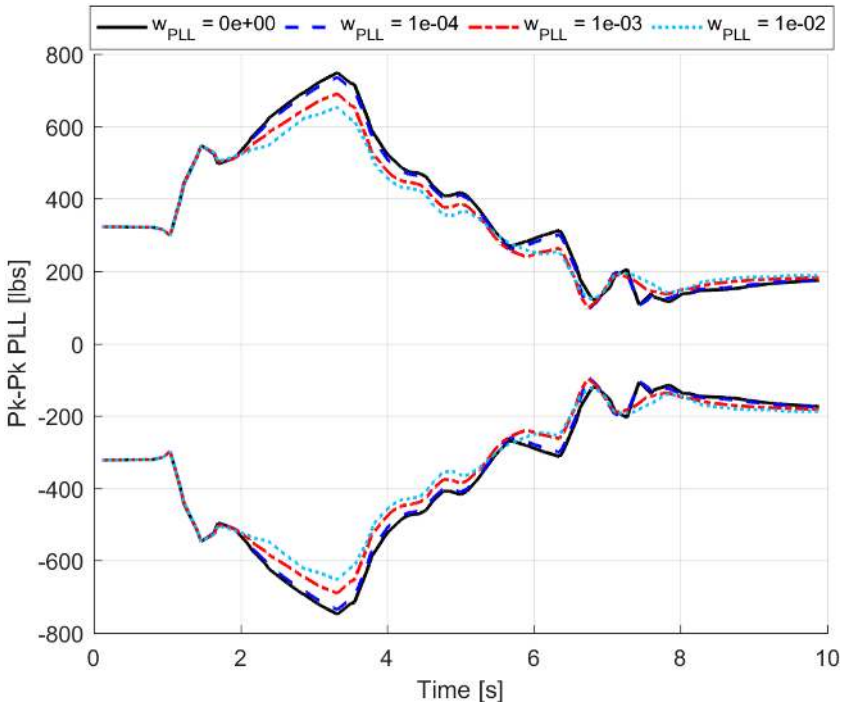

Figure 4.13: Closed-loop peak-to-peak pitch link load response to a longitudinal stick doublet.

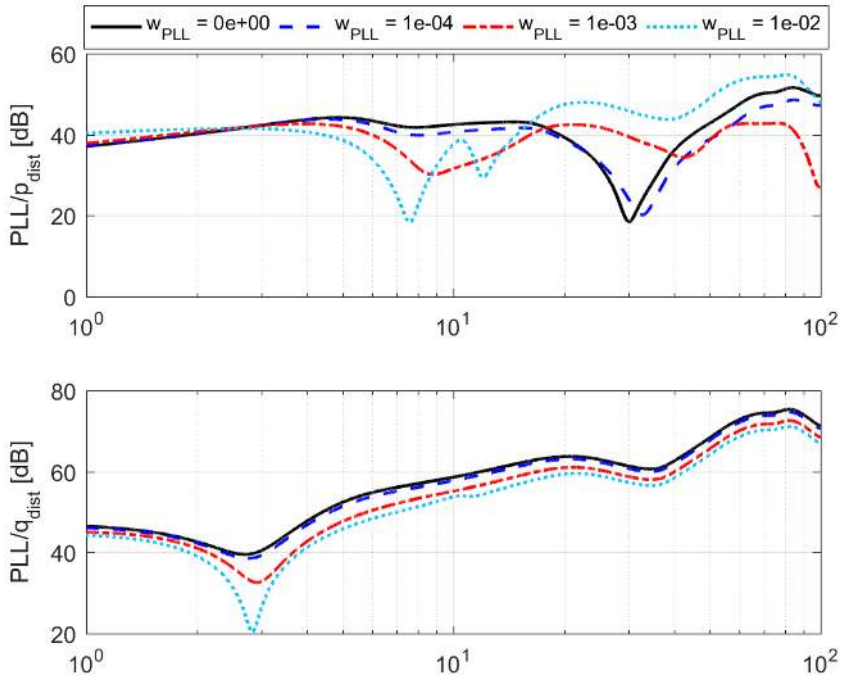

Figure 4.14: Response from angular rates disturbances to pitch link load.

In conclusion, it appears that load alleviation through feedback compensation comes at the cost of a degradation in the handling qualities, particularly in the pitch axis. In order to achieve significant load alleviation while still meeting the handling qualities requirements, a design margin optimization of the pitch axis DRB and minimum crossover frequency should be run on the baseline controller.

4.1.2.2 Rotor State Feedback

Starting from the Baseline RSFB controller, the LQR weights on the rigid-body states, rotor states, and controls are frozen while the weights on the pitch link load harmonics are varied to generate a set of LQR feedback gain matrices. Figure 4.15 provides an insight on how the weights on the pitch link load harmonics $\mathbf{w}_{\text{PLL}}$ affect the rigid-body and rotor weights in the state penalty matrix $\mathbf{Q}$. Only the diagonal terms of the state penalty matrix are shown. It is evident that constraining the pitch link load harmonics leads to increased constraints on the longitudinal and lateral flapping states.

Figure 4.16 provides insight on how the weights on the pitch link load harmonics in the output penalty matrix $\mathbf{w}_{\text{PLL}}$ affect the LQR feedback gains. Only the on-axis gains are shown. Increasing penalties on the pitch link load harmonics leads to decreasing LQR on-axis gains. This particularly true for the gains relating the longitudinal stick to the longitudinal flapping angle. These findings indicate that increasing load alleviation leads to decreasing pitch axis performance, as it was concluded for the RBFB controller.

4.1.3 Pseudo-Inverse Weighting Tailoring

Starting from the Baseline Compound RBFB controller, the pseudo-inverse weights in the feed-forward path are varied to understand how different redundant control allocations affect the rotor loads. Consider the pseudo-inverse weighting matrix:

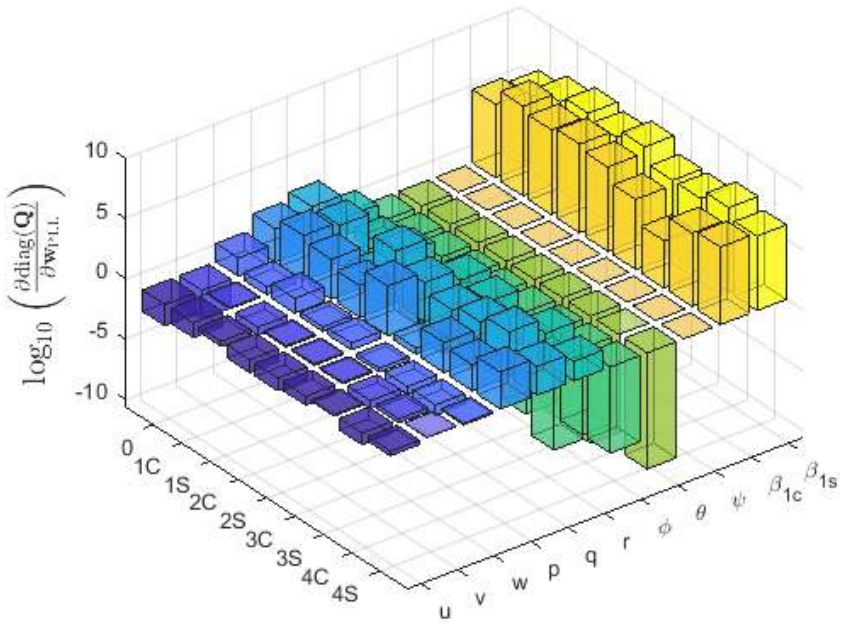

Figure 4.15: Gradient of the diagonal terms of the states penalty matrix with respect to the weights on the pitch link load harmonics.

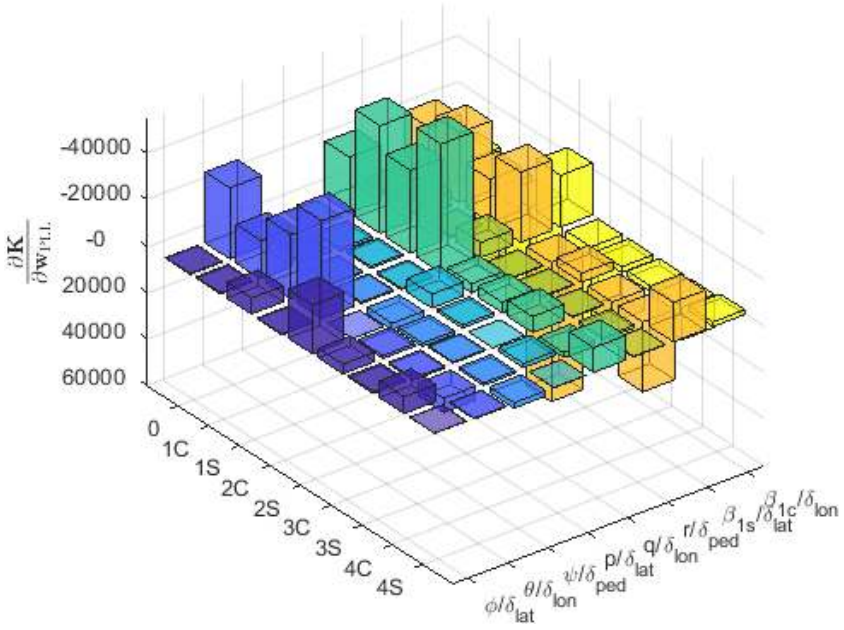

Figure 4.16: Gradient of the on-axis LQR gains with respect to the weights on the pitch link load harmonics.

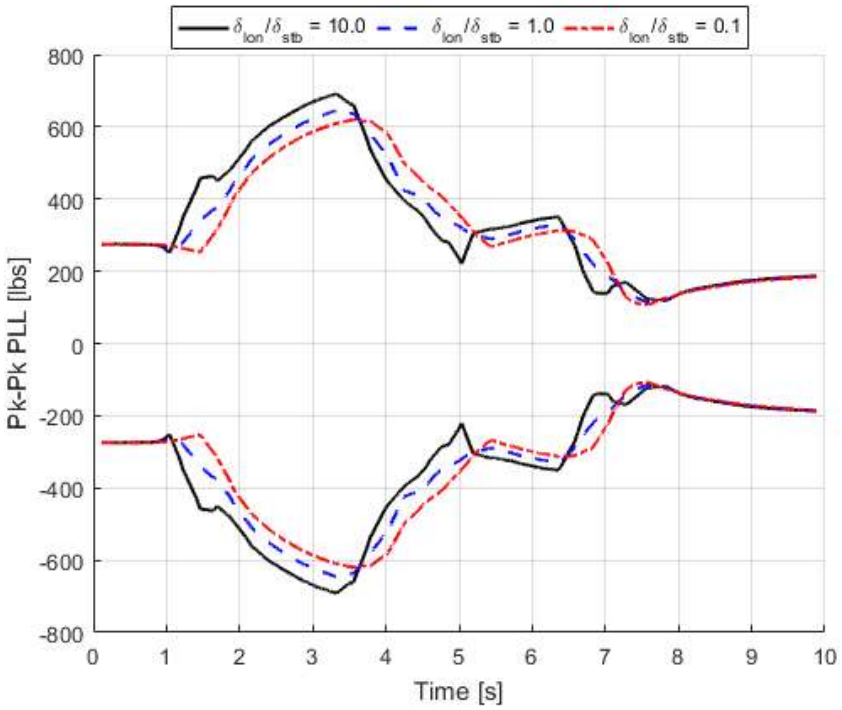

Figure 4.17: Closed-loop peak-to-peak pitch link load response to a longitudinal stick doublet.

$$\mathbf{W} = \text{diag}\left(W_{\delta_{\text{lat}}}\ W_{\delta_{\text{lon}}}\ W_{\delta_{\text{ped}}}\ W_{\delta_{\text{sym}}}\ W_{\delta_{\text{dif}}}\ W_{\delta_{\text{stb}}}\right) \tag{4.1}$$

For the longitudinal axis, the ratio of the weights on the longitudinal cyclic and stabilator sticks are varied to provide more or less feed-forward control actuation to each effector. The sum of the weights that are varied is kept constant, and is equal to 2. The set of controllers obtained this way is tested in batch simulations. Figure 4.17 shows how the rotor loads decrease with increasing control actuation of the stabilator. Figure 4.18 shows how the control signal is re-allocated from longitudinal cyclic to the stabilator.

The set of controllers obtained is analyzed in the frequency domain. Figure 4.19 shows the closed-loop frequency response of the pitch link load to the commanded pitch rate for varying pseudo-inverse weights. The rotor loads appear to decrease with increasing weighting on the stabilator for the typical flight control system's

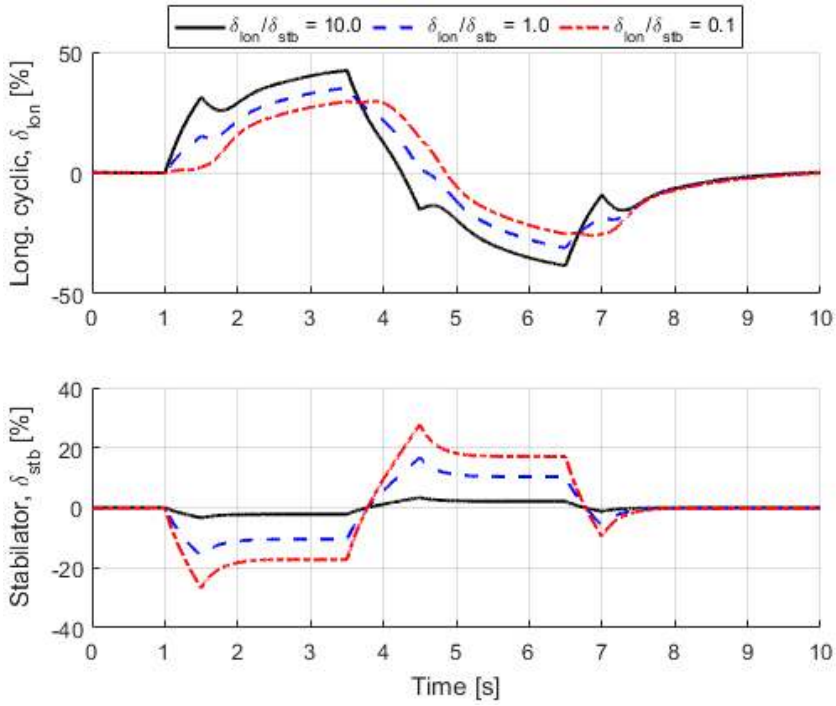

Figure 4.18: Closed-loop controls response to a longitudinal stick doublet.

frequency range.

For the lateral axis, the ratio of the weights on the lateral cyclic and differential flaperon sticks are varied to provide more or less feed-forward control actuation to each effector. The sum of the weights that are varied is kept constant, and is equal to 2. The set of controllers obtained this way is tested in batch simulations. Figure 4.20 shows how the rotor loads decrease with increasing control actuation of the differential flaperons. Figure 4.21 shows how the control signal is re-allocated from lateral cyclic to the differential flaperons.

The set of controllers obtained is analyzed in the frequency domain. Figure 4.22 shows the closed-loop frequency response of the pitch link load to the commanded pitch rate for varying pseudo-inverse weights. The rotor loads appear to decrease with increasing weighting on the differential flaperons for the typical flight control system's frequency range.

Since the pseudo-inverse control strategy is used solely in the feed-forward path,

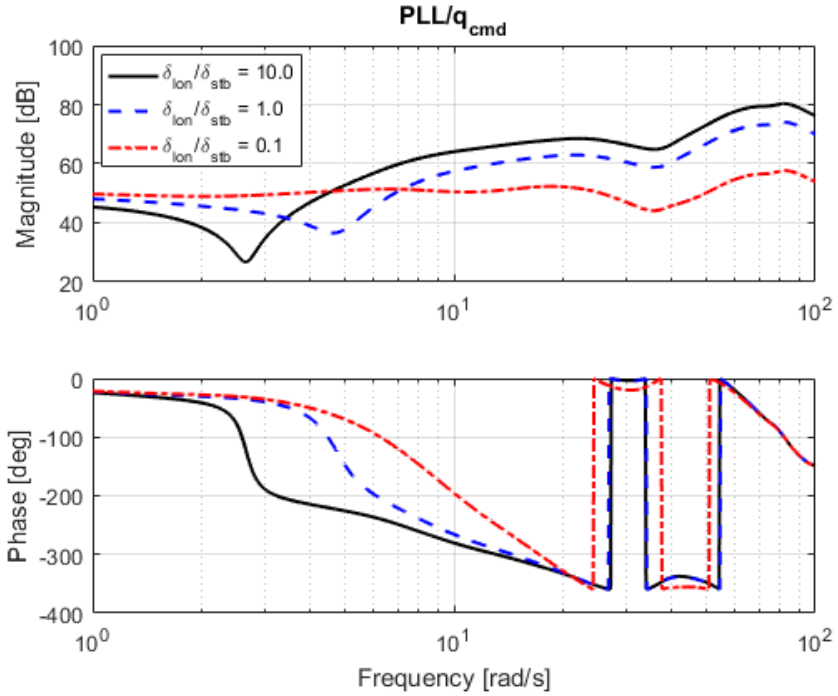

Figure 4.19: Closed-loop frequency response of the pitch link load to the commanded pitch rate for varying pseudo-inverse weights.

the only handling qualities affected by varying the pseudo-inverse weights are the bandwidth and phase delay. Figure 4.23 shows the bandwidth and phase delay with varying pseudo-inverse weighting. In general, the phase delay decreases with increasing allocation to the redundant aerodynamic surfaces. This is expected as the aerodynamic surfaces have much faster dynamics when compared to the rotor. Pitch bandwidth appears to increases with increasing pseudo-inverse weights on the stabilator. It is concluded that compounding the rotorcraft is an effective way of both decreasing rotor loads and improving handling qualities. Virtually, in forward flight at speeds where aerodynamic effects are significant, the control signal can be increasingly allocated to the redundant aerodynamic surfaces up to the point where the aerodynamic surfaces reach saturation for the most aggressive maneuvers.

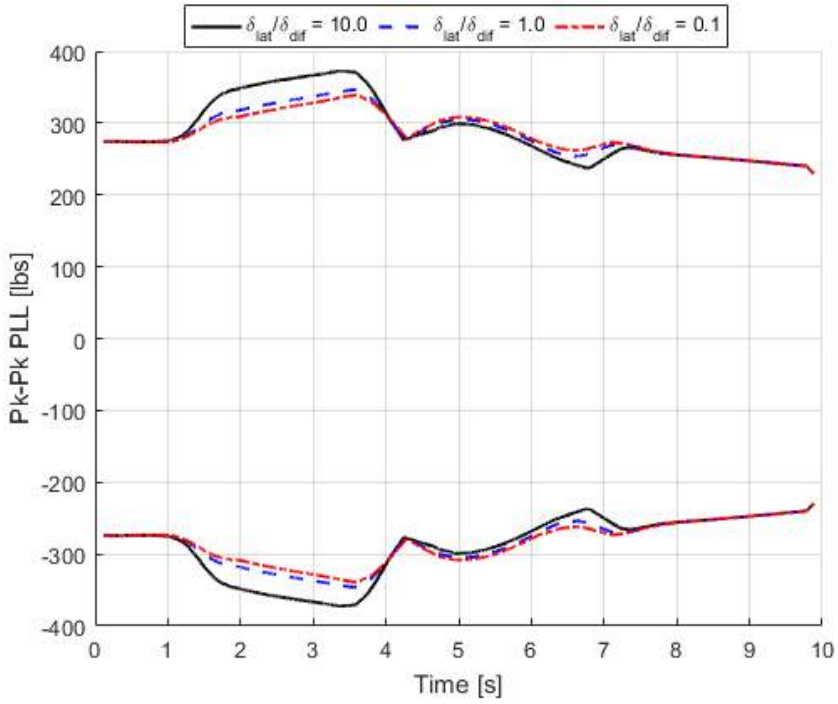

Figure 4.20: Closed-loop peak-to-peak pitch link load response to a longitudinal stick doublet.

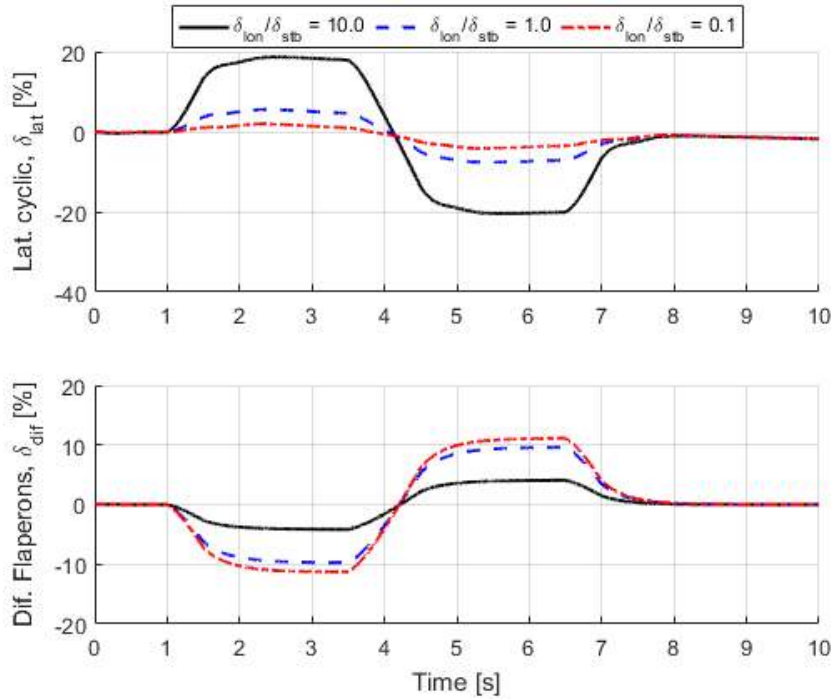

Figure 4.21: Closed-loop controls response to a lateral stick doublet.

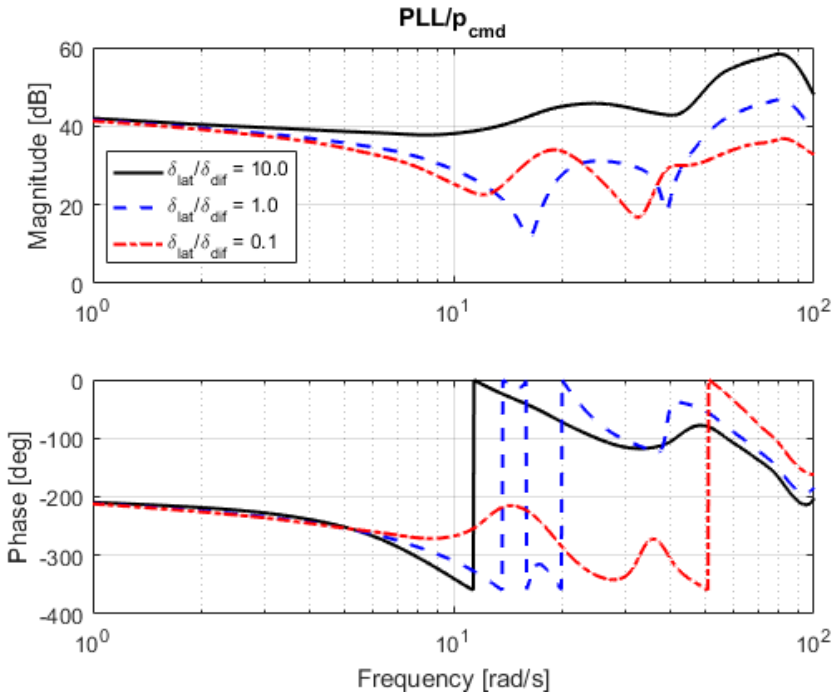

Figure 4.22: Closed-loop frequency response of the pitch link load to the commanded roll rate for varying pseudo-inverse weights.

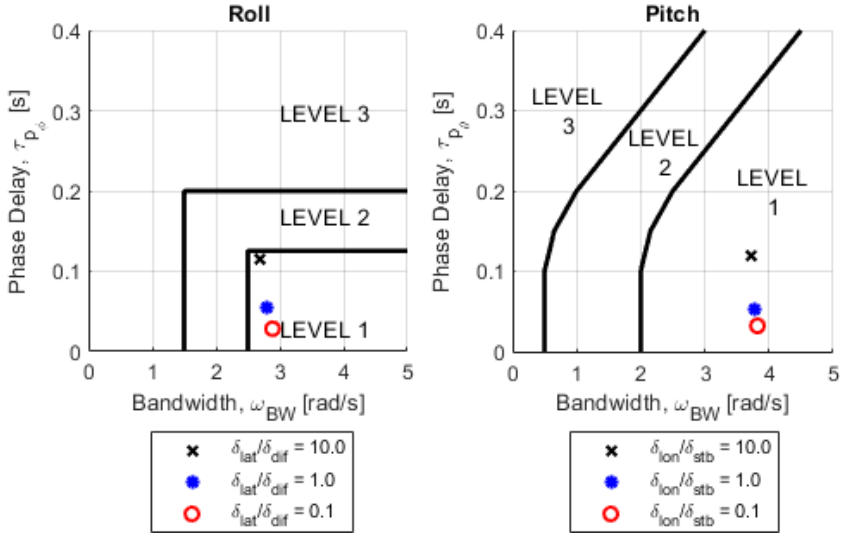

Figure 4.23: Bandwidth and phase delay with varying pseudo-inverse weighting.

4.2 Controller Optimization

4.2.1 Conventional Helicopter

An optimization of the feedback path is run in CONDUIT® for the conventional helicopter. The LQR weights on the pitch link load harmonics are optimized to meet ADS-33E-PRF specifications while minimizing the area under the PLL/q_{dist} frequency response. The weights on the rigid-body states and controls for the rigid-body feedback case, and the weights on the rigid-body states, rotor states, and controls for the rotor state feedback case, are frozen and the LQR weights on the pitch link load harmonics are set as separate optimization variables.

Figure 4.24 shows how the area under the PLL/q_{dist} response is minimized for the optimized LAC controllers. This directly translates to an alleviation in rotor loads, as shown for a pitch rate doublet in Fig. 4.25. The handling qualities are all met for the optimization controller, as shown in Figs. 4.26 and 4.27, respectively, for the rigid-body and rotor state feedback cases. Model following requirements in the pitch axis are not Level 1 as the response of the rotorcraft is actually best modelled by a 2^{nd} order model in high-speed forward flight. The penalties on the pitch link load harmonics for the optimized controller are reported in Table 4.1. It is concluded that constraining the the rotor load harmonics in LQR design successfully leads to load alleviation while still meeting desired handling qualities. The peak-to-peak rotor loads are reduced up to a 10% when Level 1 handling qualities for target acquisition and tracking are met. However, target acquisition and tracking is the most stringent mission task element (MTE) in ADS-33 specifications and may not be necessary for missions where load alleviation is active. Optimizing the gains for less stringent MTEs can lead to higher load reduction. A relaxation of the handling qualities requirements can lead to increased load reduction as well. Further, as shown in Section 4.1.3, employing redundant control surfaces can further increase load alleviation.

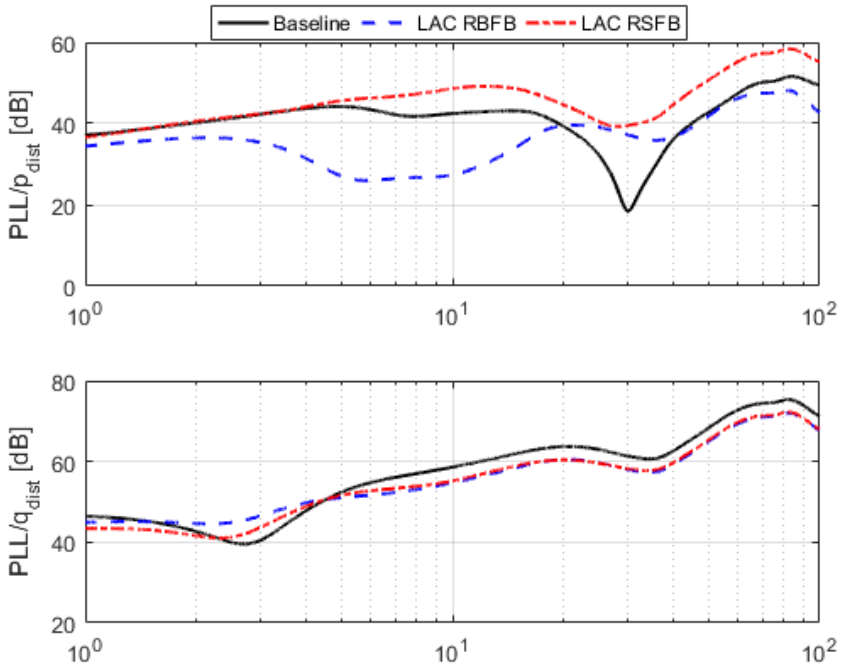

Figure 4.24: Minimization of the angular rates disturbances to pitch link load response.

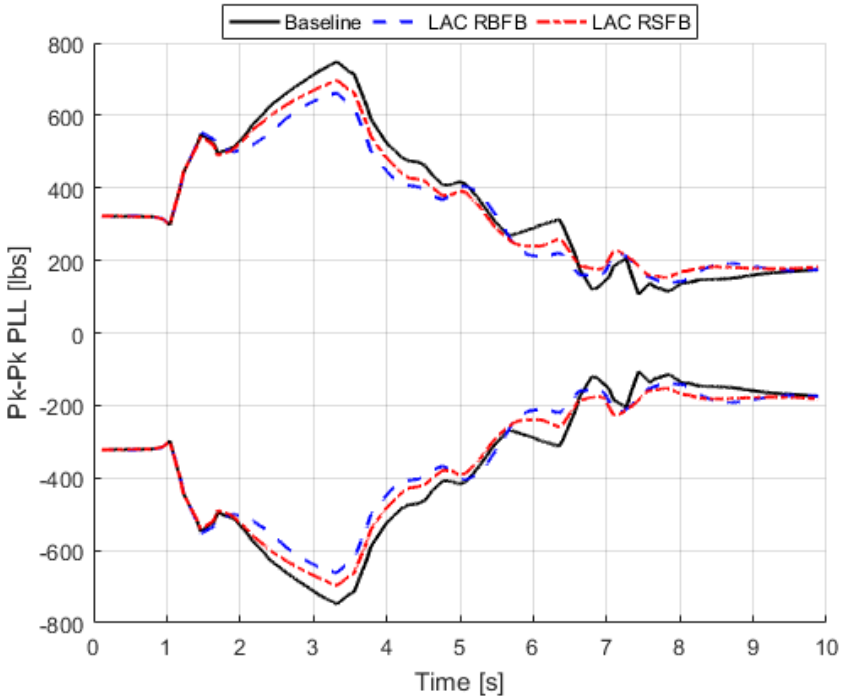

Figure 4.25: Closed-loop peak-to-peak pitch link load response to a longitudinal stick doublet.

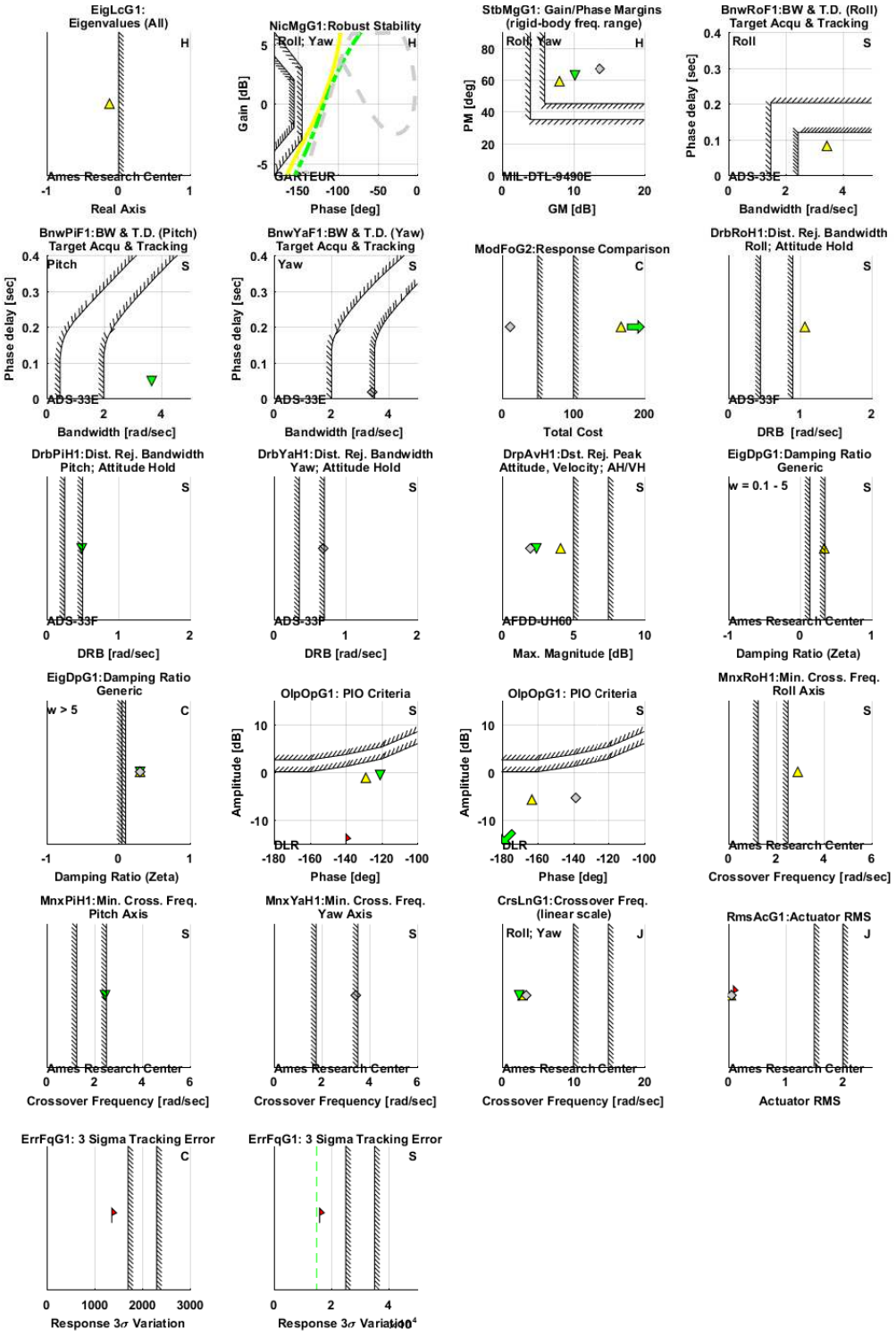

Figure 4.26: Handling qualities for RBFB LAC controller.

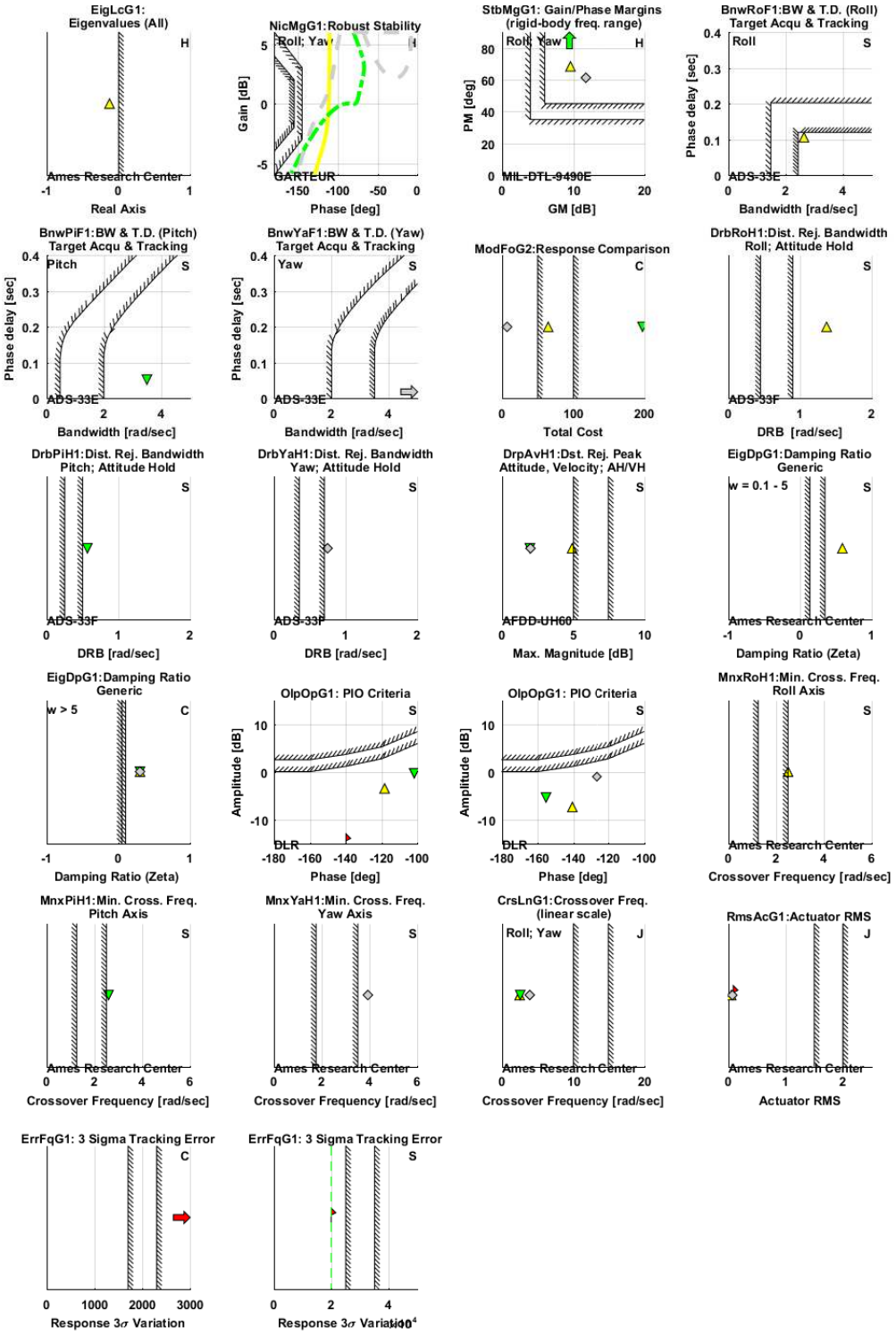

Figure 4.27: Handling qualities for RSFB LAC controller.

Table 4.1: Weights on the diagonal elements of $\hat{\mathbf{Q}}$.

Parameter	Units	RBFB	RSFB
u	ft/s	0	0
v	ft/s	0	0
w	ft/s	0	0
p	rad/s	1.0828e+2	7.2244e+1
q	rad/s	3.8252e+2	3.8028e+1
r	rad/s	2.0207e+1	4.6778e+1
ϕ	rad	6.2138e+2	6.3637e+2
θ	rad	1.9255e+2	1.9195e−2
ψ	rad	2.9349e+2	3.0897e+2
β_{1c}	rad	-	1.2958e−4
β_{1s}	rad	-	1.2823e−4
PLL_0	lbs	1.1040e−3	1.4387e−3
PLL_{1c}	lbs	2.6080e−3	2.7130e−3
PLL_{1s}	lbs	2.3360e−3	2.3876e−3
PLL_{2c}	lbs	2.2328e−3	2.4231e−3
PLL_{2c}	lbs	2.6670e−3	2.6878e−3
PLL_{3c}	lbs	1.7931e−2	1.8462e−2
PLL_{3s}	lbs	7.0606e−2	7.5601e−2
PLL_{4c}	lbs	2.3700e−4	2.1485e−4
PLL_{4s}	lbs	6.5220e−3	6.0963e−3

Chapter 5

Identification of Linear Time-Periodic Systems from Flight Test Data

5.1 Introduction

The formulation of Linear Time-Periodic (LTP) systems dates back to the late nineteenth century and it is attributed to Floquet [14]. This enabled the reduction of real-world systems that operate under a periodic regime to an LTP formulation under the assumption of small perturbations. While LTP systems exist in many fields (communication systems, space systems, industrial processes, etc.), the work presented herein focuses on the application to rotorcraft. In rotorcraft, LTP systems are relevant to the analysis and design of active rotor control systems such as Higher Harmonic Control (HHC) where the swashplate is actuated at higher harmonic frequencies, On-Blade Control (OBC) where HHC inputs are fed to actuators on each blade, and Individual Blade Control (IBC) where each blade input is actuated independently. A comprehensive survey of the different approaches and their history is found in a study by Friedmann and Millot [28]. In

recent years, Saetti and Horn studied the use of LTP systems towards the design of Load Alleviation Control (LAC) [66, 67].

Ever since the early 2000s, various techniques were developed to extract LTP systems from physics-based models via linearization schemes, and to subsequently approximate these LTP systems with a higher order Linear Time Invariant (LTI) systems that can be used in control design. Cheng, Tischler, and Celi [20] developed a numerical scheme to directly obtain an LTI approximation of a nonlinear simulation to capture the nonlinear system's periodic nature. This was accomplished by subjecting the nonlinear system to harmonic perturbations during the linearization procedure. The methodology was demonstrated using a blade-element helicopter simulation with rigid blades and a 3 state Pitt-Peters inflow model.

In the late 2000s Prasad, Olcer, Sankar, and He [21–24] demonstrated how a high-order LTI model representative of the rotor periodic nature is obtained using a two-step procedure. First, an LTP model is extracted by linearizing the nonlinear dynamics of the helicopter about a periodic equilibrium at incremental azimuthal steps over one rotor revolution. Second, Harmonic Decomposition [25] is performed on the LTP system states to obtain an approximated high-order LTI model. Although this numerical scheme has shown success, it relies on a second-order formulation of the original LTP system that can be problematic for degrees of freedom not explicitly represented in second-order form.

A more general formulation that accurately captures the higher harmonic dynamics relative to degrees of freedom not explicitly in second order form is proposed by Lopez and Prasad, starting from 2013 [12, 25, 26]. This formulation relies on a first-order representation of an LTP system. This technique has proven to accurately approximate nonlinear time periodic models by including the effects of coupling harmonic terms for body, inflow, and rotor degrees of freedom.

All the previously mentioned techniques concentrated on extracting a LTP systems from physics-based models via numerical schemes. However, very few studies

focused on experimentally characterizing LTP systems. In 2004, Verdult, Lovera, and Verhaegen identified an LTP system of the rotor dynamics alone from simulated experiments [32]. Surprisingly, no studies actually concentrated on identifying an LTP systems of the coupled rotor and rigid body dynamics from flight-test data.

The objective of this paper is to identify an LTP system representative of the coupled rigid body / rotor dynamics of a rotorcraft from flight-test data. This is a fundamental step toward the implementation of HHC/IBC/OBC in industry, where manufacturers design and validate their control systems using models obtained from flight-test data. Further, the LTP thus obtained could also be used towards LAC and limit envelope avoidance.

5.2 Methodology

5.2.1 CIFER® Overview

This research uses the Comprehensive Identification from Frequency Responses (CIFER®) software package developed by the U.S. Army Aeroflightdynamics Directorate (AFDD) at the NASA Ames Research Center [58]. CIFER® embodies frequency-response methods for system identification of both aircraft and rotorcraft. CIFER® is used to identify a completely generic state-space model structure of the form:

$$\mathbf{M}\dot{\mathbf{x}} = \mathbf{F}\mathbf{x} + \mathbf{G}\mathbf{u}(t-\tau) \tag{5.1}$$

that best fits MIMO frequency-response data. The matrices $\mathbf{M}$, $\mathbf{F}$, $\mathbf{G}$, and the vector τ contain the model parameters to be identified. A measurement (or output) vector $\mathbf{y}$ is introduced because the states $\mathbf{x}$ might not be directly measurable or

only a subset might be measurable:

$$\mathbf{y} = \mathbf{H}_0\mathbf{x} + \mathbf{H}_1\dot{\mathbf{x}} \tag{5.2}$$

where the matrices $\mathbf{H}_0$ and $\mathbf{H}_1$ are composed of known constants. Once the identification parameters are determined, the model equations can be expressed in conventional state-space form:

$$\dot{\mathbf{x}} = \mathbf{A}\mathbf{x} + \mathbf{B}\mathbf{u}(t-\tau) \tag{5.3a}$$

$$\mathbf{y} = \mathbf{C}\mathbf{x} + \mathbf{D}\mathbf{u}(t-\tau) \tag{5.3b}$$

where:

$$\mathbf{A} = \mathbf{M}^{-1}\mathbf{F} \tag{5.4a}$$

$$\mathbf{B} = \mathbf{M}^{-1}\mathbf{G} \tag{5.4b}$$

$$\mathbf{C} = \mathbf{H}_0 + \mathbf{H}_1\mathbf{M}^{-1}\mathbf{F} \tag{5.4c}$$

$$\mathbf{D} = \mathbf{H}_1\mathbf{M}^{-1}\mathbf{G} \tag{5.4d}$$

The frequency-response matrix of the identification model $\mathbf{T}(s)$ relates the Laplace transform of the measured data (or output) vector $\mathbf{y}$ to the Laplace transform of the input vector $\mathbf{u}$:

$$\mathbf{Y}(s) = \mathbf{T}(s)\mathbf{U}(s) \tag{5.5}$$

The frequency-response matrix of the model to be identified $\mathbf{T}(s)$ is expressed as a function of the state-space identification model matrices $\mathbf{M}$, $\mathbf{F}$, $\mathbf{G}$, $\mathbf{H}_0$, $\mathbf{H}_1$, and the time delays τ by taking the Laplace transform of Eq. 5.2 and performing some algebraic manipulations:

$$\mathbf{T}(s) = [\mathbf{H}_0 + s\mathbf{H}_1][(s\mathbf{I} - \mathbf{M}^{-1}\mathbf{F})^{-1}\mathbf{M}^{-1}\mathbf{G}] \circ \tau(s) \tag{5.6}$$

where a common time delay is included for all output responses to a particular control. The cost function to be minimized is:

$$J = \sum_{l=1}^{n_{\mathrm{TF}}} \left\{ \frac{20}{n_\omega} \sum_{\omega_1}^{\omega_{n_\omega}} W_\gamma [W_g(|\hat{T}_c| - |T|)^2 + W_p(\angle \hat{T}_c - \angle T)^2] \right\}_l \tag{5.7}$$

where:

n_ω is the number of frequency points,

ω_1 and ω_{n_ω} are the starting and ending frequencies of fit,

n_{TF} is the number of transfer functions to be fit,

$\hat{T}_c$ is the frequency response obtained from flight data, and

W_γ, W_g, and W_p are weighting functions.

Specifically, W_γ is a weighting function dependent on the value of the coherence function at each frequency point $\omega_1, \omega_2, ..., \omega_{n_\omega}$ and for each frequency response pair T_l:

$$W_\gamma(\omega) = \left[1.58 \left(1 - e^{-\gamma_{xy}^2} \right) \right]^2 \tag{5.8}$$

where γ_{xy}^2 is the coherence function, thereby emphasizing the most reliable data. The distribution of points is automatically adjusted to avoid data that shows a local drop in coherence below a cutoff frequency parameter of $(\gamma_{xy}^2)_{\mathrm{cut}} = 0.4$. W_g and W_p are the relative weights for magnitude and phase squared errors:

$$W_g = 1.0 \tag{5.9a}$$

$$W_p = 0.01745 \tag{5.9b}$$

The accuracy of the model is best characterized by the average overall cost function:

$$J_{\mathrm{ave}} = \frac{J}{n_{\mathrm{TF}}} \tag{5.10}$$

The n_p parameters to be identified in the model matrices are collected into an

identification vector:

$$\Theta = \left[\theta_1 \ \theta_2 \ ... \ \theta_{n_p}\right] \tag{5.11}$$

An optimization algorithm varies the identification parameters Θ until a minimum value of the average cost $J_{\text{ave}}(\Theta)$ is obtained. The algorithm uses a pattern search method. An overall average cost function that achieves $J_{\text{ave}} \leq 100$ is generally considered as reflecting an acceptable level of accuracy for flight dynamics modeling and is typical of helicopters.

The coherence function estimate is defined at each frequency f by:

$$\hat{\gamma}^2_{xy}(f) = \frac{|\hat{G}_{xy}|^2}{|\hat{G}_{xx}||\hat{G}_{yy}|} \tag{5.12}$$

where:

$\hat{G}_{xx}$ is the input autospectrum,

$\hat{G}_{xx}$ is the output autospectrum, and

$\hat{G}_{xy}$ is the cross-spectrum.

The values of the coherence function vary between 0 and 1. For a perfectly linear system where all of the output spectrum were attributable to all the input spectrum, the coherence would have an ideal value of 1. However, in practical applications the coherence will always be less than 1 due to noise contamination in the measured output signal, to nonlinearities in the input-output system, and to process noise associated with unknown or unmeasured inputs.

A measure of the accuracy of the identified model is provided by the Cramér-Rao (CR) bounds. The Cramér-Rao bounds defined as the minimum expected standard deviation σ_i in the parameter estimate θ_i that would be obtained from many repeated maneuvers:

$$\sigma_i \leq \text{CR}_\text{i} \tag{5.13}$$

Cramér-Rao bounds for individual parameters indicate poor identifiability and suggest that these parameters be eliminated (or fixed) in the model structure. The

Cramér-Rao bound of the ith identified parameter of the converged solution Θ_0 is determined from the associated diagonal elements of the inverse of the Hessian matrix $\mathcal{H}$:

$$\mathcal{H} = \frac{\partial^2 J}{\partial \Theta \partial \Theta^T} \tag{5.14}$$

in the following way:

$$\mathrm{CR}_i = 2\sqrt{(\mathcal{H}^{-1})_{ii}} \tag{5.15}$$

The Cramér-Rao bounds are best expressed as a percentage of the converged identification values:

$$\overline{\mathrm{CR}}_i = \left| \frac{\mathrm{CR}_i}{\theta_i} \right| \times 100\% \tag{5.16}$$

A reasonable guideline is to achieve $\overline{\mathrm{CR}}_i \leq 20\%$. Several of the largest Cramér-Rao bounds may be in the range 20-40% without loss of reliability or cause for concern [58].

A Cramér-Rao bound that significantly exceeds the guidelines reflects one or both of the following problems: insensitivity or correlation. High insensitivity occurs when changes in a single parameter θ_i have little or no effect on the converged cost function $J(\Theta_0)$, indicating that the parameter is not important in the selected model structure. Parameter insensitivity is determined from the diagonal elements of the Hessian matrix:

$$I_i = \frac{1}{\sqrt{\mathcal{H}_{ii}}} \tag{5.17}$$

The parameter insensitivities are best presented as normalized percentages of the converged parameter values:

$$\bar{I}_i = \left| \frac{I_i}{\theta_i} \right| \times 100\% \tag{5.18}$$

A reasonable goal for insensitivities is to obtain $\bar{I}_i \leq 10\%$. However, several of the largest insensitivities are typically in the range of 10-20% without loss of reliability of cause for concern [58].

High correlation occurs when two or more parameters can be simultaneously varied in a linear relationship while not having an offsetting effect on the cost function. In such situation, the parameters cannot be independently determined. For two identification parameters θ_i and θ_j the correlation coefficient is:

$$\rho_{ij} = \frac{(\mathcal{H}^{-1})_{ij}}{\sqrt{(\mathcal{H}^{-1})_{ii}(\mathcal{H}^{-1})_{jj}}} \tag{5.19}$$

where:

$$-1 \leq \rho_{ij} \leq 1 \tag{5.20}$$

An absolute value of the correlation coefficient close to 1 indicates high parameter correlation and can compromise greatly the accuracy of the results, as reflected by high Cramér-Rao bounds.

5.2.2 Frequency Response

This investigation aims at identifying an LTP system that is able to capture the coupled rigid-body / rotor dynamics and predict the vibratory loads of a helicopter. A general first-order formulation of an LTP system is given by:

$$\dot{\mathbf{x}} = \mathbf{F}(\psi)\mathbf{x} + \mathbf{G}(\psi)\mathbf{u} \tag{5.21a}$$

$$\mathbf{y} = \mathbf{P}(\psi)\mathbf{x} + \mathbf{R}(\psi)\mathbf{u} \tag{5.21b}$$

where case ψ is the main rotor azimuth angle in radians. It is convenient to note that ψ is equivalent to non-dimensional time, which can be related to dimensional time via the following relation: $\psi = \Omega t$, where Ω the main rotor angular speed in rad/s, and t is the dimensional time in seconds. Each coefficient matrix is periodic with a fundamental period of T seconds, which corresponds to 2π radians or one rotor revolution:

$$\mathbf{F}(\psi) = \mathbf{F}(\psi + \Omega_f T) \tag{5.22a}$$

$$\mathbf{G}(\psi) = \mathbf{G}(\psi + \Omega_f T) \tag{5.22b}$$

$$\mathbf{P}(\psi) = \mathbf{P}(\psi + \Omega_f T) \tag{5.22c}$$

$$\mathbf{R}(\psi) = \mathbf{R}(\psi + \Omega_f T) \tag{5.22d}$$

for all ψ. For rotorcraft, the fundamental frequency can be the main rotor angular speed $\Omega_f = \Omega$ (corresponds to 1/rev), or it can be any multiple of the number of blades times the rotor speed $\Omega_f = kN_b\Omega$, $k = 1, 2, 3, ...$ (corresponds to multiples of $\mathrm{N_b}$/rev).

The LTP identification approach used in this paper is similar to the one proposed by Allen [68], where frequency-domain identification of LTP systems is performed by means of LTI techniques. When the fundamental frequency of oscillation Ω_f is known, a lifting scheme can be used to transform measurements into a set of responses that each can be described by an LTI system. The lifting scheme is done by sampling the response of the nonlinear system at non-dimensional instants:

$$\psi_n = \psi_0 + n\Omega_f T \quad \text{for} \quad n = 0, ..., n_t - 1, \tag{5.23}$$

The periodicity of the response effectively vanishes if one samples at the same non-dimensional time within the fundamental period. One important difference between identification of the lifted LTP system and standard LTI identification is the bandwidth of the response. In an ideal case, the bandwidth of response is limited to half of the sampling frequency, according to the Nyquist Theorem. In practical applications however, the bandwidth of the response is limited to less than half on the sampling frequency [58]. So the upper limit of the bandwidth of the lifted responses used to identify the LTP system is $\Omega_f/2$, whereas the upper limit of the responses used to identify the standard LTI system is $p\Omega/2$, whre p is the

number of samples per rotor revolution of the flight-test data. The lifted responses are converted to frequency responses and subsequently identified separately to obtain a set of parametric LTI models. This set of LTI models constitutes an LTP system.

5.2.3 Parametric Identification

The linear model structure used to demonstrate the concept is chosen to be relatively simple and able to capture the coupled rigid-body / rotor dynamics and the vibratory loads. The following system describes the decoupled longitudinal / heave dynamics of the rotorcraft:

$$\begin{bmatrix} \dot{w} \\ \dot{q} \\ \dot{\theta} \\ \dot{\beta}_{1c} \end{bmatrix} = \begin{bmatrix} Z_w & Z_q & -g\sin\theta_0 & Z_{\beta_{1c}} \\ M_w & M_q & 0 & M_{\beta_{1c}} \\ 0 & 1 & 0 & 0 \\ 0 & 1 & 0 & M_{f_{\beta_{1c}}} \end{bmatrix} \begin{bmatrix} w \\ q \\ \theta \\ \beta_{1c} \end{bmatrix} + \begin{bmatrix} Z_{\delta_{\text{lon}}} \\ 0 \\ 0 \\ M_{f_{\delta_{\text{lon}}}} \end{bmatrix} \delta_{\text{lon}} \tag{5.24a}$$

$$\begin{bmatrix} a_z \\ q \\ \theta \\ \beta_{1c} \end{bmatrix} = \begin{bmatrix} Z_w & 0 & g\sin\theta_0 & Z_{\beta_{1c}} \\ 0 & 1 & 0 & 0 \\ 0 & 0 & 1 & 0 \\ 0 & 0 & 0 & 1 \end{bmatrix} \begin{bmatrix} w \\ q \\ \theta \\ \beta_{1c} \end{bmatrix} + \begin{bmatrix} Z_{\delta_{\text{lon}}} \\ 0 \\ 0 \\ 0 \end{bmatrix} \delta_{\text{lon}} \tag{5.24b}$$

The same model structure is used for the parametric identification of both LTI and LTP systems. However, the stability and control derivatives (parameters) are time-invariant for the LTI model but are assumed to be time-periodic in the LTP system through the rotor azimuth angle ψ.

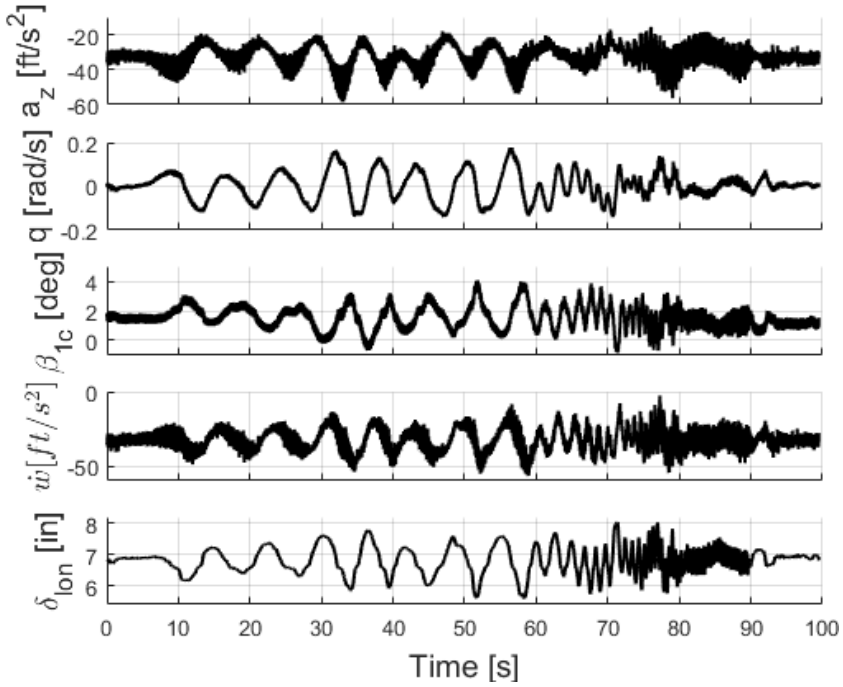

Figure 5.1: Piloted frequency sweep.

5.3 Identification from Flight Test Data

5.3.1 Frequency Response

The methodology is applied here to JUH-60 flight-test data collected at a flight condition of 80 kts in straight and level flight. A set of three frequency sweeps was performed in the longitudinal axis using longitudinal stick inputs. The measured outputs consists of the vertical acceleration in body axes a_z, the pitch rate q, and the longitudinal flapping angle in Multi-Blades Coordinates (MBC) β_{1c}. In addition, the time derivative of the vertical speed in body axes $\dot{w}$ was reconstructed in the time domain [58] and used in the identification. Although the input to the linear system is solely the longitudinal cyclic stick δ_{lon}, all of the pilot control inputs were measured. This is because when computing the frequency responses, the other pilot inputs are used to calculate and remove cross-correlation between axes [58]. Figure 5.1 shows one of the three piloted frequency sweeps. The Power

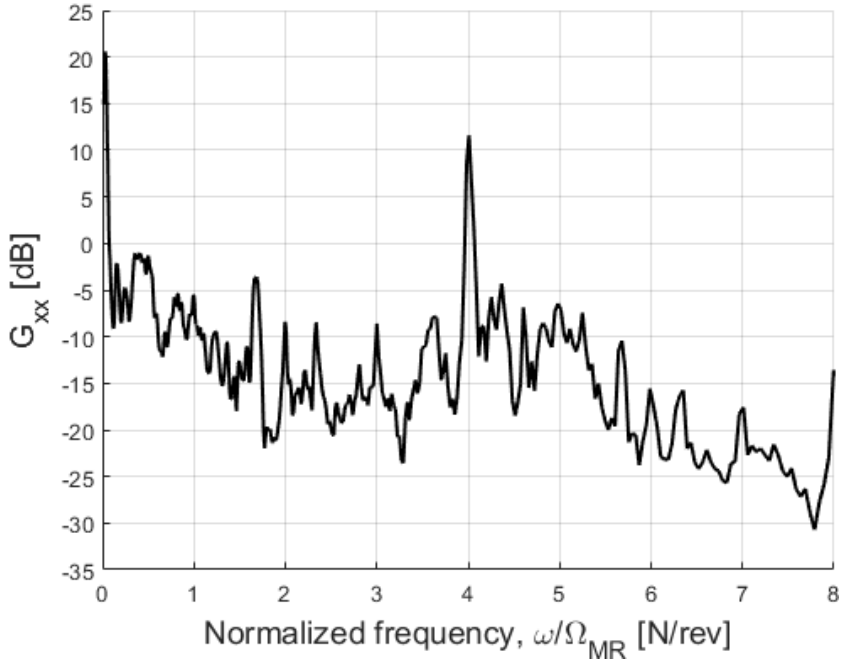

Figure 5.2: Power spectral density of $a_z(t)$.

Spectral Density is computed for the vertical acceleration measured from one of the frequency sweeps,as shown in Fig. 5.2. This is done to assess the harmonic content of the response. It is clear that the measured a_z signal has a dominant 4/rev content. This is typical of the dynamics of helicopters in forward flight, which exhibit a $\mathrm{N_b}$/rev periodic behavior [69]. In light of this, the fundamental frequency is chosen to be $\Omega_f = N_b\Omega$. Since the UH-60 has four blades and its main rotor speed is $\Omega = 27$ rad/s, the fundamental frequency is $\Omega_f = 108$ rad/s (4/rev), with a period of $T = 2\pi/108$ seconds (corresponds to 1/4 of a revolution). The frequency sweep data is sampled at the fundamental frequency (four times per rotor revolution) for each azimuthal position that is less or equal than 90 deg. Since the original flight-test data was sampled $p = 60$ times per rotor revolution, sampling at 4/rev for each azimuthal position less or equal than 90 deg leads to fifteen sets of frequency responses, one for each azimuthal position $\psi = 0, 6, 12, ..., 84$ deg. In the case of LTI estimation, the frequency sweep data is used as is. Figure 5.3 shows both the standard (in black) and the lifted (in colors) frequency responses

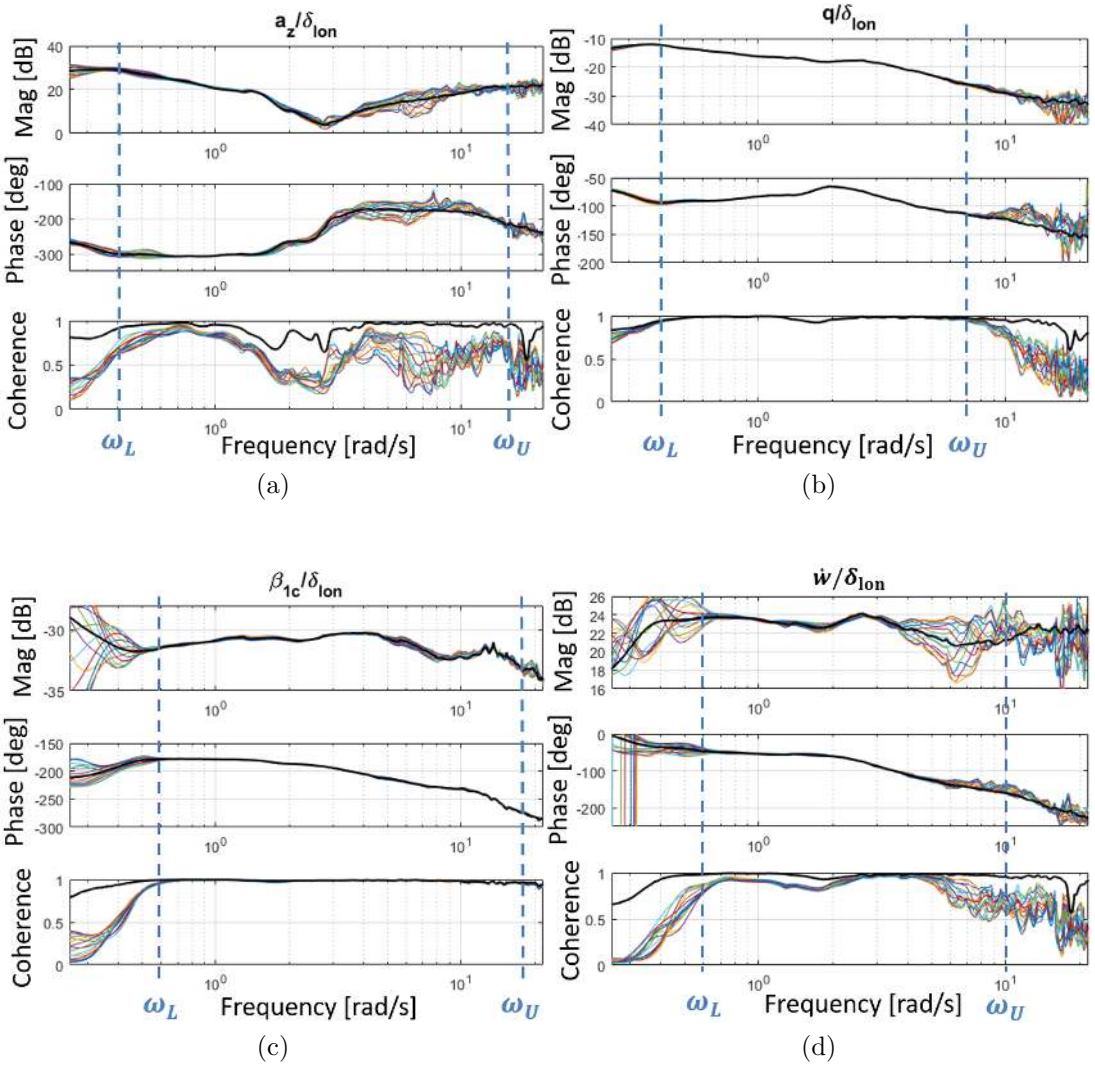

Figure 5.3: Frequency response of longitudinal stick to (a) vertical acceleration, (b) pitch rate, (c) longitudinal flap angle, and (d) vertical speed time derivative. Standard (LTI) response in black, lifted responses in colors.

computed with CIFER® [58].

5.3.2 Parametric Identification

Parametric identification is performed on each frequency response set, leading to fifteen LTI systems. Since the parameters of the LTP system are assumed to be 4/rev periodic, the fifteen LTI systems are repeated four times to constitute an

LTP system with sixty entries. An LTI system is also computed from the standard frequency response. The frequency range is chosen to be the same for both LTI and LTP parametric identification and such that the coherence of both standard and lifted responses is sufficiently high (i.e. greater than 0.6). The lower Ω_L and upper Ω_U frequency limits for each frequency response are reported visually in Fig. 5.3 and quantitatively in Table 5.1. The values of the identified stability and control derivatives for both LTI and LTP systems are shown in Fig. 5.4. A few observations can be made:

1. The identified LTP system parameters appear to be 4/rev and 8/rev periodic.

2. The mean of each of the identified LTP system parameters is very close to value of their respective LTI system parameter. This is to be expected as the LTI system constitutes the zeroth harmonic (mean) of an LTP system, and this is reflected in the stability and control derivatives as well.

A comparison between the identified LTI system and flight test data in the frequency domain is shown in Fig. 5.5. The identified LTI parameters, along with their Cramér-Rao bounds and insensitivities are reported in Table 5.2. The CR bounds provide a reliable measure of parameter accuracy for the frequency-response identification and indicate the level of correlation among the identification parameters [58]. Large relative CR bounds for individual parameters indicate poor identifiability and suggest that these parameters should be fixed in the model structure. The CR bounds for the identified LTI parameters are generally low (i.e. less than 20%). The parameters that show relatively high CR bounds have low insensitivity and are therefore retained as identification parameters. The average cost function associated with the identification is $J = 18$. The average cost functions for LTP identified models is $J = 20$. A cost function less than $J = 50$ indicates excellent match of the model to the frequency responses [58].

The eigenvalues of the identified LTI and LTP systems are reported in Table

Table 5.1: Parametric identification frequency range.

Frequency Response	ω_L [rad/s]	ω_U [rad/s]
a_z/δ_{lon}	0.4	16
q/δ_{lon}	0.4	7
$\beta_{1c}/\delta_{\text{lon}}$	0.6	18
$\dot{w}/\delta_{\text{lon}}$	0.6	10

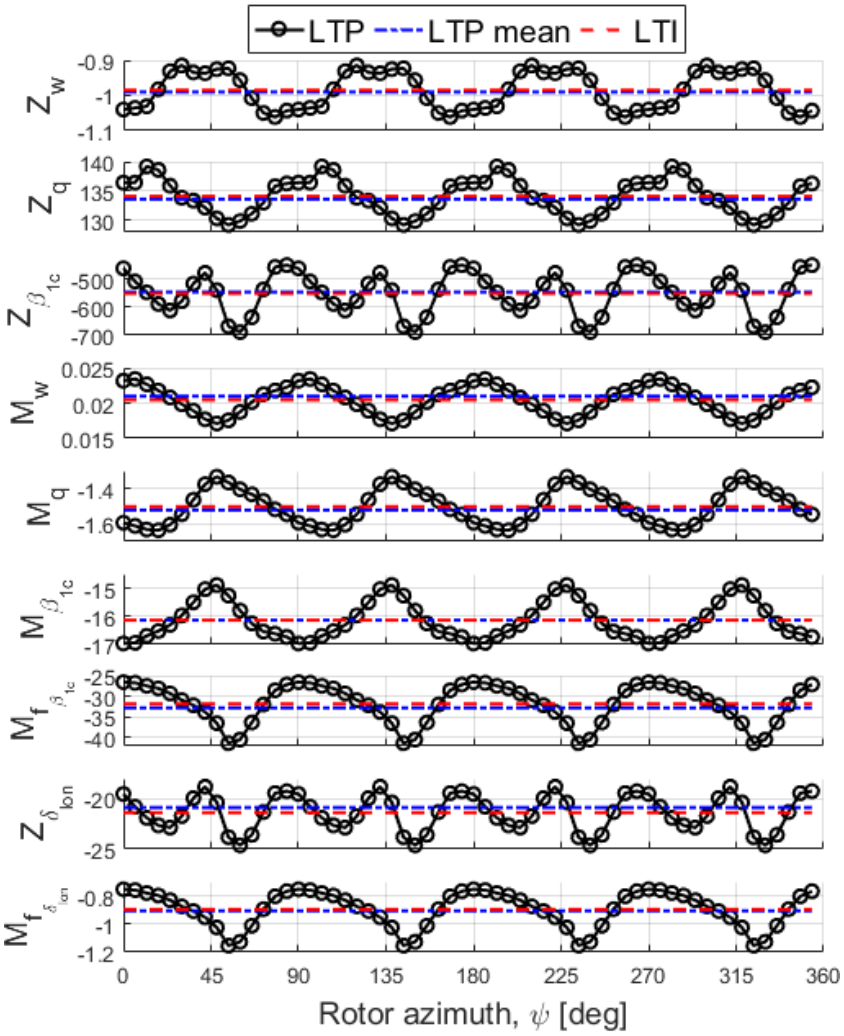

Figure 5.4: Identified parameters.

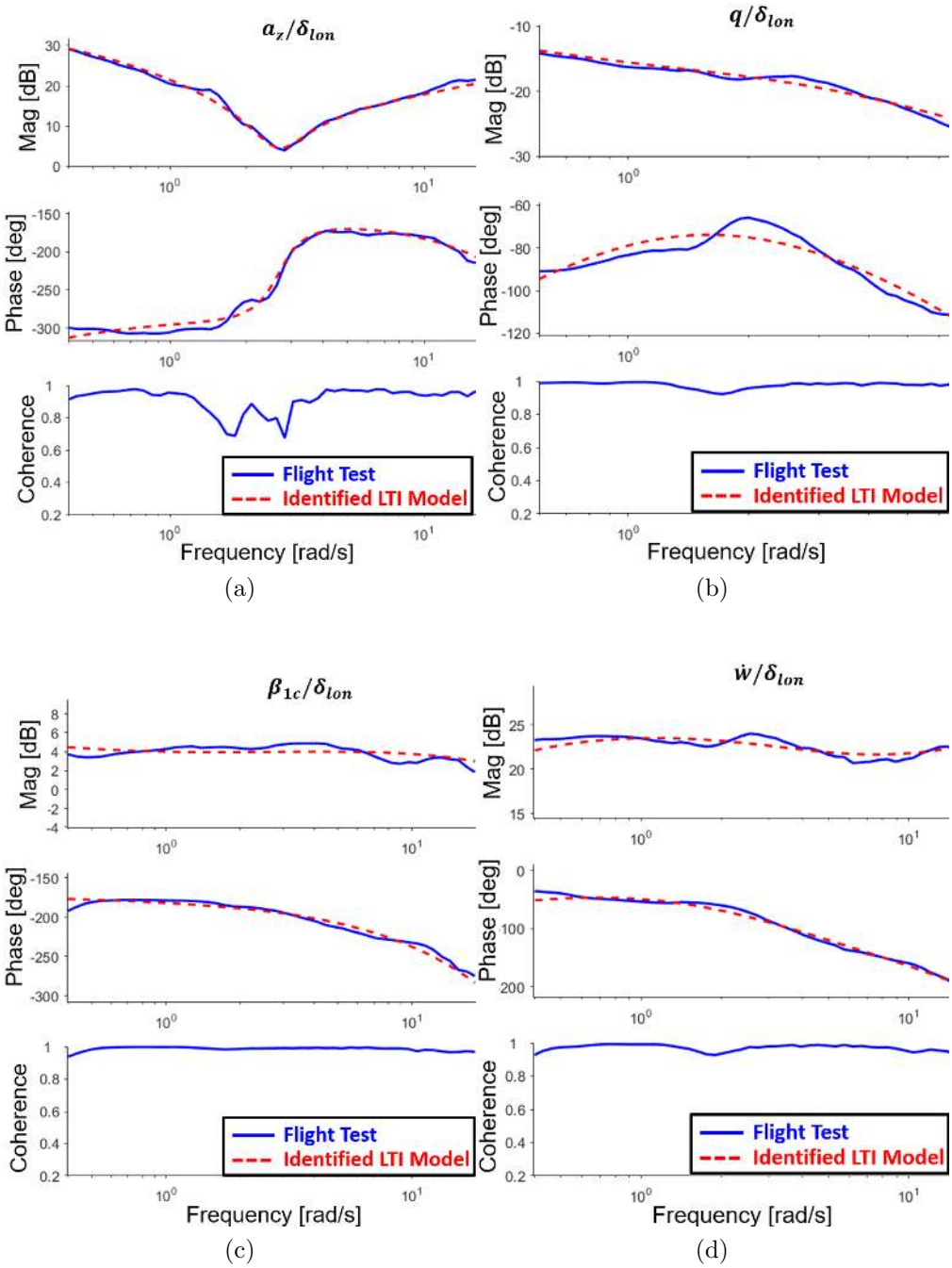

Figure 5.5: Frequency responses of the identified LTI system: longitudinal stick to (a) vertical acceleration, (b) pitch rate, (c) longitudinal flap angle, and (d) vertical speed time derivative.

Table 5.2: LTI parametric identification results.

Parameter	Value	Cramér-Rao Bound [%]	Insensitivity [%]
Z_w	-0.985 [1/s]	8.026	1.200
Z_q	134.1 [ft/(rad s^2)]	0.568	0.568
$Z_{\beta_{1c}}$	-551.6 [ft/(rad s^2)]	59.41	0.555
M_w	0.020 [rad/ft]	11.80	1.532
M_q	-1.502 [1/s]	11.74	2.041
$M_{\beta_{1c}}$	-16.13 [1/s]	6.428	0.929
$M_{f_{\beta_{1c}}}$	-31.83 [1/s]	46.55	0.384
$Z_{\delta_{\text{lon}}}$	-21.37 [ft/(s^{2}in)]	41.21	0.393
$M_{f_{\delta_{\text{lon}}}}$	-0.896 [rad/(s^{2}in)]	44.85	0.377
τ	0.072 [s]	16.73	2.673

Table 5.3: Eigenvalues.

System	λ_1	λ_2	λ_3	λ_4
LTI	-31.63	-3.001	0.302	0.019
LTP (mean)	-31.63	-3.004	0.299	0.019

5.3. The eigenvectors of the identified LTI system are reported in Table 5.4. The fastest eigenvalue $\lambda_1 \approx -31.6$ is stable and is associated with the rotor flapping mode. The second-fastest eigenvalue $\lambda_2 \approx -3.0$ is stable and is associated with short period mode. The third-fastest eigenvalue $\lambda_3 \approx 0.3$ is unstable and is associated with the short period mode as well. In this case, the short period mode, which is typically represented by a pair of complex conjugate poles, becomes two different modes represented by two real eigenvalues [70]. The slowest eigenvalue $\lambda_4 \approx -0.019$ is unstable and is associated to the pitch attitude integrator mode. All the eigenvalues and eigenvectors appear to be real. This can be imputed to the absence of the forward speed u in the model. The mean eigenvalues of the identified LTP system match closely the eigenvalues of the identified LTI system.

Table 5.4: Eigenvectors.

States	$\mathbf{v}_1$	$\mathbf{v}_2$	$\mathbf{v}_3$	$\mathbf{v}_4$
w	-0.274	1.000	-0.512	-0.027
q	-0.525	-0.907	-0.302	-0.019
θ	0.017	0.302	-1.000	-1.000
β_{1c}	-1.000	-0.017	-0.003	-0.000

5.3.3 Time Domain Validation

In order to validate the identified models, time history simulations from the LTI and LTP systems were compared to flight-test data, as shown in Fig. 5.6. The verification flight data that is used consists of a longitudinal cyclic doublet at 80 kts level flight. The time step used for the simulations is $\Delta_t = 2\pi/p\Omega$. Residual errors in the trim estimate are modelled as a bias vector $\dot{\mathbf{x}}_b$, which also provides a first-order correction for the effects of process noise in the estimate such as turbulence and unmeasured secondary controls. Similarly, residual errors in the output estimates are incorporated in the output equation as a periodic reference-shift vector $\mathbf{y}_{\text{ref}}$. The LTP system that is simulated is:

$$\dot{\mathbf{x}} = \mathbf{F}(\psi)\mathbf{x} + \mathbf{G}(\psi)\mathbf{u} + \dot{\mathbf{x}}_b \tag{5.25a}$$

$$\mathbf{y} = \mathbf{P}(\psi)\mathbf{x} + \mathbf{R}(\psi)\mathbf{u} + \mathbf{y}_{\text{ref}} \tag{5.25b}$$

If the mean of the identified LTP coefficients is close to the value of the identified LTI coefficients, one can use constant bias and reference shift vectors that are estimated from the identified LTI, as done is [58]. Several observations can be made:

1. The responses of the LTI and LTP systems are similar, and are both close to the flight data.

2. The LTI response constitutes the zeroth harmonic (mean) of the LTP response.

3. The LTP response well predicts the higher-harmonic content of the flight data. This is immediately apparent by looking at the vertical acceleration plot, presented in Fig. 5.7. Note that the vertical acceleration is predicted well up to about the tenth second of simulation, when the pitch attitude starts diverging. The pitch attitude diverges because the identified model has an unstable pitch subsidence mode.

4. Note that a periodic equilibrium is added to the LTP system response. An indication of the goodness of the identified LTP system is provided by how well its peak-to-peak response relates to the verification data. The peak-to-peak response of the vertical acceleration is shown in 5.8. For each 90 deg cycle the maximum and minimum peaks of the response are calculated. A running mean (or median) is obtained by taking the sum of the maximum and minimum peaks for each cycle and dividing by two. The curves that are plotted are the maximum and minimum peaks minus the median. The peak-to-peak response of the LTP system generally well tracks the one from the verification data.

5. Discrepancies in the predicted amplitude of a_z may be due to the simplicity of the structure of the identified LTP system. Specifically, the absence of the forward speed u and the fact that the model is decoupled from the lateral dynamics may be limiting factors.

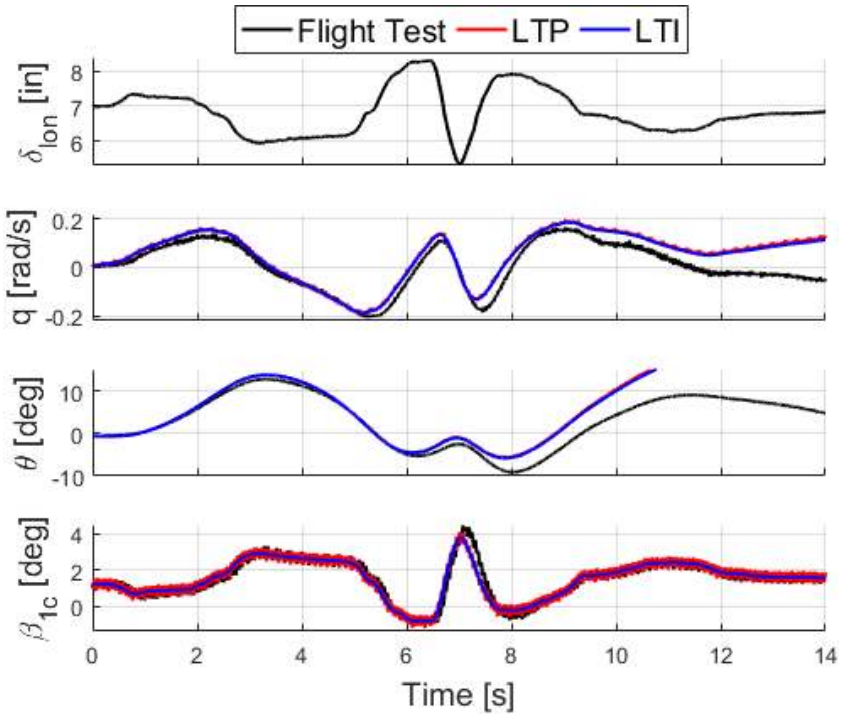

Figure 5.6: Rigid body and rotor response to a longitudinal stick doublet.

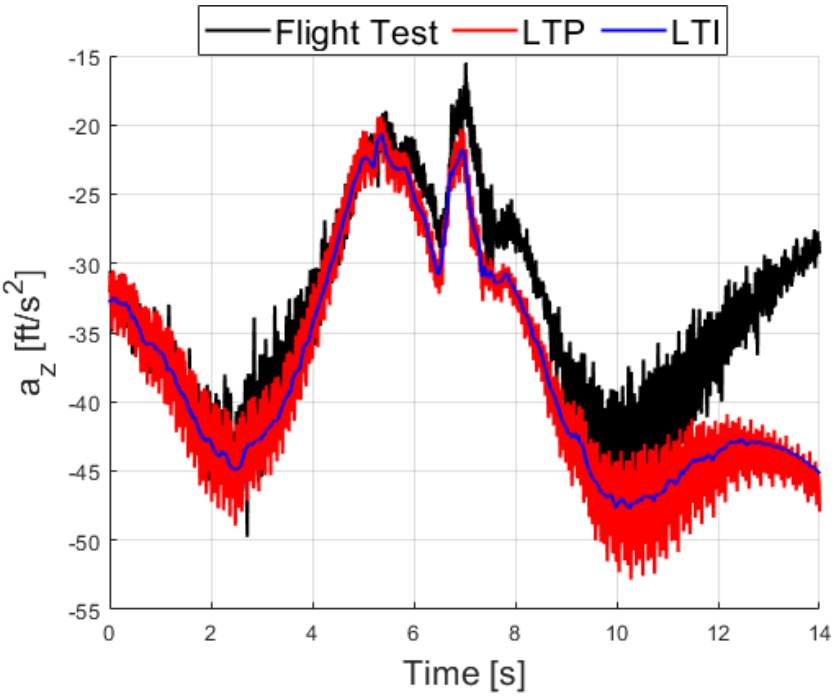

Figure 5.7: Vertical acceleration response to a longitudinal stick doublet.

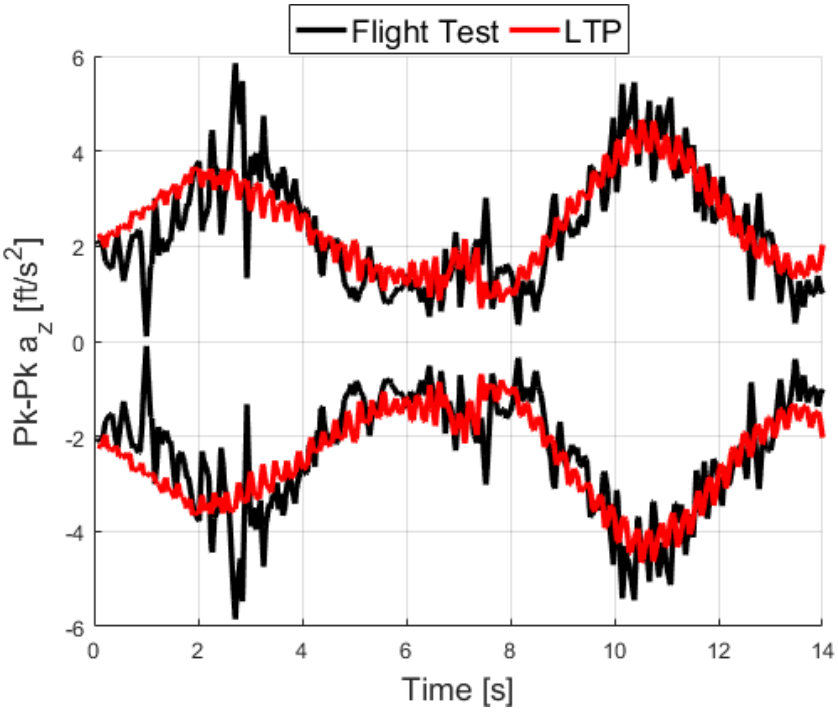

Figure 5.8: Peak-to-peak vertical acceleration responses to a longitudinal stick doublet.

5.4 Contribution of the Higher Harmonics to the Helicopter Dynamics

5.4.1 Modal Participation Factors

Modal participation factors are computed to quantify the influence of the higher harmonics on the dynamics of the helicopter. In particular, modal participation factors describe the modal participation of each state to each mode through the relative magnitude of the harmonic components of each state. The modal participation factors are calculated by harmonic decomposition means, as demonstrated by Lopez and Prasad [13]. Consider an LTP system:

$$\dot{\mathbf{x}} = \mathbf{F}(\psi)\mathbf{x} \tag{5.26}$$

Using a first-order formulation introduced by Lopez and Prasdad [25], the state of the LTP system is decomposed in a finite number of harmonics via Fourier analysis:

$$\mathbf{x} = \mathbf{x}_0 + \sum_{i=1}^{N} \mathbf{x}_{ic} \cos i\psi + \mathbf{x}_{is} \sin i\psi \tag{5.27}$$

An approximate high-order LTI can be represented in matrix form by defining the augmented state vector:

$$\mathbf{X}^T = \left[\mathbf{x}_0^T \mathbf{x}_{1s}^T \mathbf{x}_{1c}^T \ldots \mathbf{x}_{Nc}^T \mathbf{x}_{Nc}^T\right] \tag{5.28}$$

where x_0 is the zeroth harmonic component and x_{ic} and x_{is} are the ith harmonic cosine and sine components of the state. The state equation of the resulting LTI model is:

$$\dot{\mathbf{X}} = \mathbf{A}\mathbf{X} \tag{5.29}$$

Once the LTI system matrix is calculated, it can be used to compute the modal participation factors using the following procedure:

1. Solve for the eigenvalues of the high-order LTI system of Eq. 5.29.

2. Convert the harmonic states of the eigenvector from real-trigonometric Fourier coefficients to complex-exponential Fourier coefficients.

3. Compute modal participation factors by normalizing the modal participation with respect to the sum of the magnitudes of all harmonic components for each particular state and mode.

The above methodology is implemented and applied to the identified LTP system to assess how the harmonic components of each state contribute to each particular mode. The high-order LTI considered for this study retains up to the eighth harmonic. Figure 5.9 shows the modal participation factors of each state to each mode. Figure 5.9(a) shows the modal participation of the vertical speed to each

mode. Ninety-three percent of the contribution to the rotor mode comes from the zeroth harmonic, whereas the fourth and eighth harmonics contribute for up to 6% and 1%, respectively. The contribution of the vertical speed to all the other modes comes almost exclusively through the zeroth harmonic. Figures 5.9(b-c) show the modal participation factors of the pitch rate and pitch attitude, respectively, to each mode. Ninety-nine percent of the contribution to all modes comes from the zeroth harmonic, whereas the fourth harmonic contributes for up to a 1%. Figure 5.9(c) shows the modal participation factors of the longitudinal flapping angle β_{1c} to each mode. Ninety-three percent of the contribution to all modes comes from the zeroth harmonic of the longitudinal flapping angle, whereas the fourth and eighth harmonics contribute for up to 6% and 1%, respectively. It is concluded that the higher harmonics of the rotor states contribute to up to a 7% of the longitudinal helicopter dynamics, 4/rev being the most dominant higher harmonic. The zeroth-harmonic of the rotor states contributes to the remaining 93% of the longitudinal helicopter dynamics. The rigid-body states contribute to the helicopter flight dynamics almost exclusively through the zeroth harmonic. This validates the use of the LTI model for flight dynamics applications [69].

5.4.2 Time Vectors

The time vector diagram introduced by McRuer, Ashkenas, and Graham [71] provides a useful illustration of relative phasing and contribution of each term in the equations of motion for a selected response, and can be especially useful in interpreting the system ID model response [13]. For example, the unforced pitch rate response (i.e., controls fixed) is obtained as follows:

$$\dot{q} = M_w w + M_q q + M_{\beta_{1c}} \beta_{1c} \tag{5.30}$$

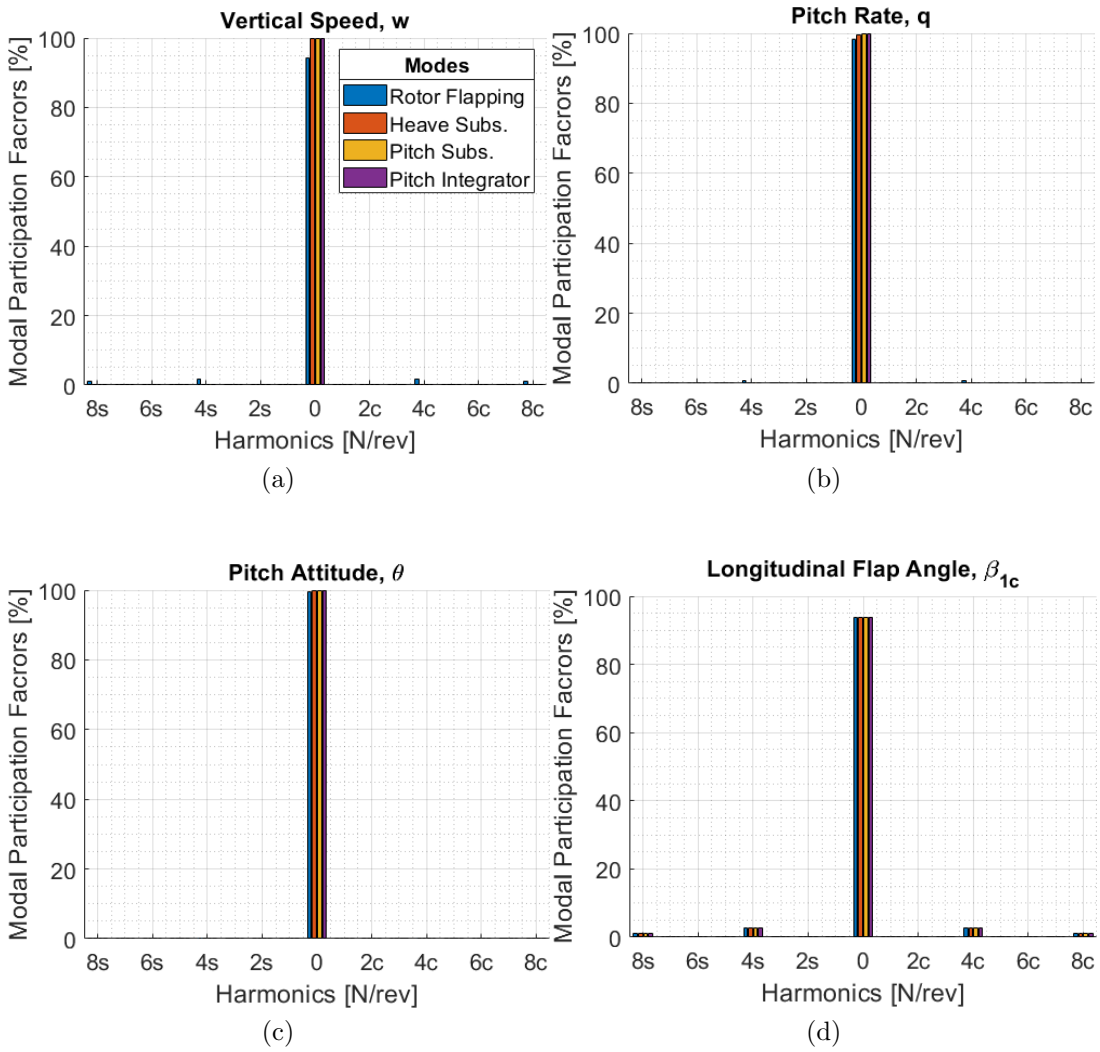

Figure 5.9: Modal participation factors of the various harmonics of (a) the vertical speed, (b) pitch rate, (c) pitch attitude, and (d) longitudinal flap angle.

If one takes the Laplace transform and assumes zero initial conditions (trim), obtains:

$$sq - M_w w - M_q q - M_{\beta_{1c}} \beta_{1c} = 0 \tag{5.31}$$

The time vector associated with a particular mode is calculated by substituting the eigenvalue ($s = \lambda_i$) relative to that particular mode, the associated eigenvector, and the identified values of the stability derivatives in Eq. 5.31. This was done both for the identified LTI and LTP systems. Note that the eigenvalues, eigenvectors,

and identified parameters of the LTP systems are dependent on the azimuth angle ψ. Generally, the plot of the time vector is a closed polygon that illustrates the balance of inertial moments sq with with the relative importance and phasing of each aerodynamic term in the unforced equation of motion. Since all eigenvalues and eigenvectors are real in this particular case, the components of the time vector are real as well. Figure 5.10 illustrate the time vectors for both LTP and LTI systems relative to the pitch rate equation and the heave subsidence mode. A few observation can be made:

1. The inertial term has opposite phase with respect to the aerodynamics terms.

2. The LTP system time vector is periodic with 4/rev and 8/rev components and its mean coincides with the LTI time vector.

3. The summation of the aerodynamic and inertial terms gives zero, which is expected since the time vector is a closed polygon.

4. Considering the LTP system time vector, the amplitude of oscillation of each term, when compared to the magnitude of the mean of each term (zeroth harmonic), gives an indication of the relative importance of the higher-harmonic content to the zeroth harmonic for each term for a particular state and mode.

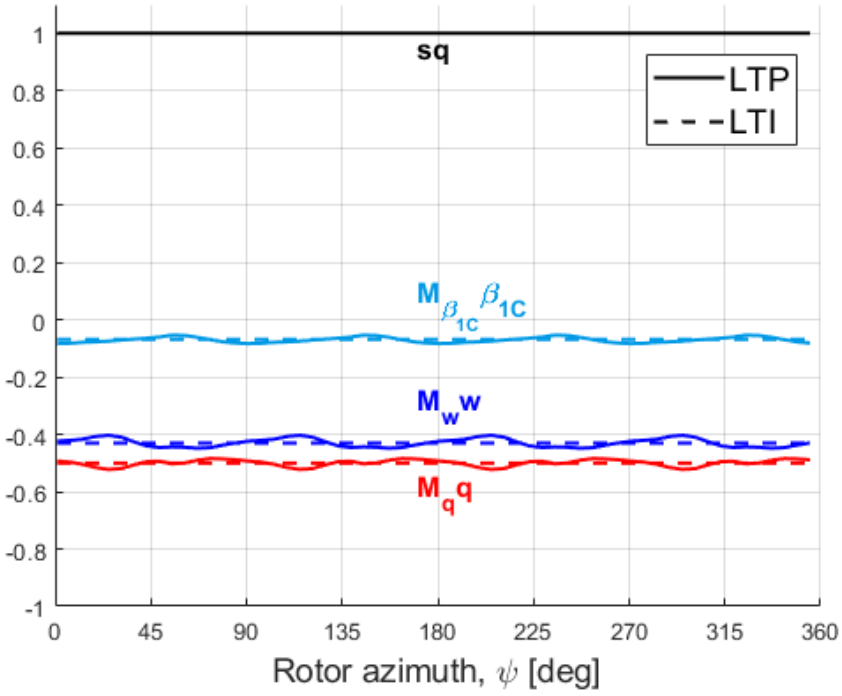

Figure 5.10: Time vector relative to the pitch rate equation of motion and the heave subsidence mode.

Chapter 6

Concluding Remarks and Recommendations for Future Work

6.1 Concluding Remarks

6.1.1 Alleviation of Unsteady Rotor Loads

Two nonlinear simulation models were developed with FLIGHTLAB®. The first model is representative of a notional conventional helicopter similar to a UH-60. The second model is representative of compound rotorcraft similar to a UH-60 with the addition of a wing with flaperons, and a moving horizontal tail (stabilator). Both models accurately model the rotor loads by including flexible blades, dynamic inflow models, and nonlinear aerodynamics. Linear Time-Periodic (LTP) systems were obtained from the nonlinear models via linearization schemes using a two-step procedure. First, the nonlinear FLIGHTLAB® models were trimmed at at 120 kts forward and level flight. Next, the models were linearized at incremental azimuth positions over one rotor revolution. High-order Linear Time-Invariant (LTI) approximations of the LTP systems were obtained using harmonic decomposition. Harmonic decomposition decomposes the state, input, and output vectors

into a finite number of harmonics. Reduced-order models were derived from the high-order LTI systems to make control design tractable. By retaining the higher-harmonics of the rotor loads in the output, the reduced order models accurately predicted the rotor loads.

Flight control laws based on a model following control strategy were developed to provide stability and rate command / attitude hold response in the roll, pitch and yaw axes for both the conventional helicopter and the compound rotorcraft. The flight control laws were first optimized to meet a comprehensive set of set of stability, handling qualities, and performance specifications. Next, an assessment was made on how the feed-forward and feedback paths of the controller affect the rotor loads. Finally, the controllers were optimized to minimize the unsteady rotor loads while still meeting the desired handling qualities.

Based on this work, the following conclusions are drawn.

1. Each harmonic of the Individual Blade Coordinates (IBC) states is influenced by the same, and a lower and a higher harmonic of the Multi-Blade Coordinates (MBC) states. For high-order LTI systems to capture the behavior of IBC states up to the N^{th} harmonic, it was retained up to the $(N+1)^{\text{th}}$ harmonic when performing harmonic decomposition on LTP systems with MBC states.

2. By retaining the higher-harmonics of the rotor loads in the output, the 9-state reduced-order model accurately predicted the influence of the 0^{th} harmonics of the rigid-body states on the higher-harmonics of the rotor loads. By also retaining the longitudinal and lateral flapping angles as states, the 11-state model predicted the influence of the 0^{th} harmonics of the rigid-body states and flapping states on the higher-harmonics of the rotor loads.

3. Previous work limitations, such as the reliance on non-physics-based models and curve fits to approximate rotor loads, were lifted.

4. Rotor loads in high-speed forward flight were particularly sensitive to pitch rate commands. Roll rate commands also affect the rotor loads, but in a minor way. Rotor loads were relatively insensitive to yaw rate commands.

5. Load alleviation through feed-forward compensation (command model tailoring) was effective in providing alleviation of the rotor loads. However, it came at the cost of a degradation in bandwidth and phase delay.

6. Load alleviation through feedback compensation came at the cost of a degradation in the handling qualities, particularly in the pitch axis. The pitch axis disturbance rejection bandwidth (DRB) and minimum crossover frequency posed potential limitations in achievable load alleviation.

7. Redundant control allocation was very effective towards load alleviation and did not degrade the handling qualities. Since the redundant control surfaces considered have much faster dynamics than the main rotor, their employment improved the handling qualities, especially bandwidth and phase delay.

8. The controller minimizes rotor loads perturbations from their periodic equilibrium. It follows that this methodology is well suited for alleviating unsteady loads. However, it does not affect stationary (trim) loads.

9. The optimized load alleviation controllers provided load alleviation while still meeting a comprehensive set of stability, handling qualities, and performance requirements. Rotor loads are abated by up to a 10% for the conventional helicopter when Level 1 handling qualities for target acquisition and tracking are met. Optimizing the gains for less stringent mission task elements (MTEs) can lead to higher load reduction. Employing redundant control surfaces can further increase load alleviation.

10. Since the load alleviation controllers act solely through 1^{st} harmonic swashplate controls, it can readily be integrated with existing or future Automatic

Flight Control Systems (AFCS) on civil or military rotorcraft.

6.1.2 Identification of Linear-Time Periodic Systems from Flight Test Data

A methodology to identify Linear Time Periodic (LTP) systems from flight test data was developed. Frequency sweeps were sampled at different rotor azimuth angles with a frequency of 4/rev. A set of frequency responses were obtained from the lifted time response using CIFER®. Subsequently, parametric identification was performed for each set of frequency responses. The resulting set of Linear Time Invariant (LTI) systems constitute an LTP system. The technique was applied to UH-60 flight test data. The LTP system obtained is representative of the coupled rigid body / rotor dynamics and accounts the higher harmonic content of the rotorcraft dynamics. The LTP system was validated both in the frequency and time domains. Modal participation factors and time vectors were computed to assess the contribution of the higher harmonics to the rotocraft dynamics. Based on this work, the following conclusions can be reached.

1. Linear Time-Periodic systems representative of the rotor dynamics and vibratory loads cannot only be derived from physics-based models via linearization schemes, but can also be identified from flight test data.

2. The identified LTP system is able to predict the higher-harmonic content of the rotorcraft dynamics. An indication of the goodness of the identified LTP system is provided by how well the contraction/expansion of the periodic equilibrium of the vibratory loads relates to the flight test data.

3. Discrepancies in the predicted amplitude of the vibratory loads may be due to the simplicity of the structure of the identified LTP system. Specifically, the absence of the forward speed u and the fact that the model is decoupled from the lateral dynamics may be limiting factors.

4. The higher harmonics of the rotor states contribute to up to a 7% of the of the helicopter flight dynamics, 4/rev being the most dominant higher harmonic. The rigid body states contribute to the helicopter flight dynamics almost exclusively through the zeroth harmonic.

5. Although this study concentrates on the vertical acceleration as vibratory load, other rotor loads could readily be included as outputs of the identified LTP system. Once the LTP system is identified, it can be used to obtain an approximate high-order LTI system that provides a convenient framework for dynamic analysis and controller synthesis.

6. Since manufacturers rely on dynamic models obtained from flight data, the use of high-order LTI models derived from identified LTP systems could lead to the extension of Higher Harmonic Control (HHC), Individual Blade Control (IBC), On-Blade Control (OBC), Load Alleviation Control (LAC), and flight envelope limit detection and avoidance to production rotorctaft.

6.2 Recommendations for Future Work

Since identified LTP systems have been shown to accurately predict rotorcraft vibratory loads, they constitute a viable and computationally-effective way to predict flight envelope limits. In this sense, LTP systems could be used towards flight envelope limit detection and protection. In previous studies [35–41], the limit detection problem was tackled with the use of stochastic methods such as neural networks and fuzzy-logic systems. LTP systems, unlike neural networks, are deterministic and could be readily identified across the entire flight envelope through a model stitching strategy [58, 72].

Although this study concentrates on the vertical acceleration as vibratory load, other rotor loads could readily be included as outputs of the identified LTP system. For instance, the pitch link loads could be taken into consideration. Once the

LTP system is identified, it can be used to obtain an approximate high-order LTI system that provides a convenient framework for dynamic analysis and controller synthesis. The use of high-order dynamics models towards HHC and LAC was recently demonstrated by Lopez and Prasad [12, 25, 26], and Saetti and Horn [66, 67]. Although these studies used high-order systems obtained from physics-based models, the approaches proved successful. Since manufacturers rely on dynamic models obtained from flight data, the use of high-order LTI models derived from identified LTP systems could lead to the extension of HHC and LAC to production rotorctaft.

In general, LTI models are sufficient for standard control design since the rigid-body states contribute to the helicopter flight dynamics almost exclusively through the zeroth harmonic. For primary flight control, where the objective is to control the zeroth harmonic (average) of the rigid-body motion, the difference in using LTI models rather than LTP systems is negligible. Certainly, LTI systems provide a more convenient and simpler framework. However, if one aims at predicting or controlling the higher harmonics of the rigid-body and rotor motion, LTP systems are necessary.

Flight control design based on LTP systems identified from flight-test data could benefit the Future Vertical Lift (FVL) program. FVL is a plan to develop a new generation of military helicopters for the U.S. Army with increased capabilities in speed, range, and payload, and reduced maintenance and operational cost. Because these rotorcraft would operate at significantly higher speeds than the current helicopters, alleviation of the higher harmonic rotor loads and flight envelope protection are key elements to reduced maintenance cost. These rotorcraft are also likely to employ redundant control surfaces which, in connection with LTP-based flight control design, demonstrated outstanding effectiveness towards the alleviation of unsteady rotor loads [66].

Bibliography

[1] G. E. Cooper and R. P. Harper, "The use of pilot rating in the evaluation of aircraft handling qualities," tech. rep., Advisory Group for Aerospace Research and Development, Neuilly-sur-Seine, France, 1969.

[2] Anon, "Aeronautical design standard performance specification handling qualities requirements for military rotorcraft," tech. rep., U.S. Army Aviation and Missile Command Aviation Engineering Directorate, Redstone Arsenal, AL, 2000.

[3] D. B. Caudle, "Damage mitigation for rotorcraft through load alleviating control," Master's thesis, The Pennsylvania State University, University Park, PA, 2014.

[4] B. R. Geiger, "Flight control optimization on a fully compounded helicopter with redundant control effectors," Master's thesis, The Pennsylvania State University, University Park, PA, 2005.

[5] C. Thaiss, C. C. McColl, J. F. Horn, E. E. Keller, A. Ray, R. Semidey, and N. D. Phan, "Rotorcraft real time damage alleviation through load limiting control," in *55th AIAA/ASME/ASCE/AHS/ASC Structures, Structural Dynamics, and Materials Conference*, (National Harbor, MD), Jan 13-17, 2014.

[6] N. A. Sahani, J. F. Horn, G. J. Jeram, and J. V. R. Prasad, "A hub moment limit protection system using neural network prediction," *Journal of the American Helicopter Society*, vol. 51, no. 4, pp. 331–340, 2006.

[7] N. A. Sahani and J. F. Horn, "Adaptive model inversion control of a helicopter with structural load limiting," *Journal of Guidance, Control, and Dynamics*, vol. 29, no. 2, pp. 411–420, 2006.

[8] D. O. Bridges, J. F. Horn, and A. Ray, "Model-following control of a military helicopter with damage mitigation," in *AIAA Guidance, Navigation, and Control Conference and Exhibit*, (San Franisco, CA), Aug 15-18, 2005.

[9] J. F. Horn and N. A. Sahani, "Detection and avoidance of main rotor hub moment limits on rotorcraft," *Journal of Aircraft*, vol. 41, no. 2, pp. 372–379, 2006.

[10] J. F. Horn, A. J. Calise, and J. V. R. Prasad, "Flight envelope limit detection and avoidance of rotorcraft," *Journal of the American Helicopter Society*, vol. 47, no. 4, pp. 253–262, 2006.

[11] D. G. Miller, T. M. Black, and M. Joglekar, "Tiltrotor control law design for rotor loads alleviation using modern control techniques," in *American Control Conference*, Jun 26-28, 1991.

[12] M. Lopez, *LINEAR TIME INVARIANT APPROXIMATIONS OF LINEAR TIME PERIODIC SYSTEMS FOR INTEGRATED FLIGHT AND VIBRATION CONTROL*. PhD thesis, Georgia Institute of Technology, Atlanta, GA, 2016.

[13] M. Lopez, J. V. R. Prasad, M. B. Tischler, and C. K. K. Takahashi, M D, "Simulating HHC/AFCS interaction and optimized controllers using piloted maneuvers," in *American Helicopter Society 71st Annual Forum Proceedings*, (Virginia Beach, VA), May 5-7, 2015.

[14] G. Floquet, "Sur les équations différentielles linéaires à coefficients périodiques," *Annales Scientifiques de l'École Normale Supérieure*, vol. 12, pp. 47–88, 1883.

[15] N. M. Wereley and S. R. Hall, "Frequency response of linear time periodic systems," in *29th IEEE Conference on Decision and Control*, (Honolulu, HI), Dec 5-7, 1990.

[16] N. M. Wereley and S. R. Hall, "Linear time periodic systems: Transfer function, poles, transmission zeroes and directional properties," in *American Control Conference*, (Boston, MA), Jun 26-28 1991.

[17] S. R. Hall and N. M. Wereley, "Generalized nyquist stability criterion for linear time periodic systems," in *American Control Conference*, (San Diego, CA), May 23-25 1990.

[18] P. Crimi, "A method for analyzing the aeroelastic stability of a helicopter rotor in forward flight," tech. rep., NASA CR-1332, National Aeronautics and Space Administration, Washington, DC, 1969.

[19] V. J. Piarulli and R. P. White, "A method for determining the characteristic functions associated with the aeroelastic instabilities of helicopter rotor blades in forward flight," tech. rep., NASA CR-1577, National Aeronautics and Space Administration, Washington, DC, 1970.

[20] R. P. Cheng, M. B. Tischler, and R. Celi, "A high-order, time invariant linearized model for application to HHC/AFCS interaction studies," in *American Helicopter Society 59th Annual Forum Proceedings*, (Phoenix, AZ), May 6-8 2003.

[21] J. V. R. Prasad, F. E. Olcer, L. N. Sankar, and C. He, "Linear models for integrated flight and rotor control," in *Proceedings of the 34th European Rotorcraft Forum*, (Liverpool, UK), Sep 16-19, 2008.

[22] J. V. R. Prasad, F. E. Olcer, L. N. Sankar, and C. He, "Linear time invariant models for integrated flight and rotor control," in *Proceedings of the 35th European Rotorcraft Forum*, (Hamburg, Germany), Sep 22-25, 2009.

[23] F. E. Olcer, *Linear Time Invariant Models for Integrated Flight and Rotor Control*. PhD thesis, Georgia Institute of Technology, Atlanta, GA, 2011.

[24] F. E. Olcer and J. V. R. Prasad, "A methodology for evaluation of coupled rotor-body stability using reduced order linear time invariant (LTI) models," in *American Helicopter Society 67th Annual Forum Proceedings*, (Virginia Beach, VA), May 3-5, 2011.

[25] M. Lopez and J. V. R. Prasad, "Linear time invariant approximations of linear time periodic systems," *Journal of the American Helicopter Society*, vol. 62, no. 1, pp. 1–10, 2017.

[26] M. Lopez and J. V. R. Prasad, "Periodic system analysis using a linear time invariant formulation," in *Proceedings of the 39th European Rotorcraft Forum*, (Moscow, Russia), Sep 3-6, 2013.

[27] J. Shaw, "Higher harmonic blade pitch control for helicopter vibration reduction: a feasibility study," Master's thesis, Massachusetts Institute of Technology, Cambridge, MA, 1967.

[28] P. P. Friedmann and T. A. Millot, "Vibration reduction in rotorcraft using active control: A comparison of various approaches," *Journal of Guidance, Control, and Dynamics*, vol. 18, no. 4, pp. 664–673, 1995.

[29] M. D. Abraham, F. E. Olcer, M. F. Costello, M. D. Takahashi, and M. D. Tischler, "Integrated design of AFCS and HHC for rotorcraft vibration reduction using dynamic crossfeed," in *American Helicopter Society 67th Annual Forum Proceedings*, (Virginia Beach, VA), May 3-5, 2011.

[30] A. K. Padthe, P. P. Friedmann, F. X. Bagnoud, and J. V. R. Prasad, "High-fidelity linear time-invariant models for higher harmonic closed-loop rotor control studies," *Journal of the American Helicopter Society*, vol. 62, no. 1, pp. 1–15, 2017.

[31] A. K. Padthe, P. P. Friedmann, M. Lopez, and J. V. R. Prasad, "Analysis of high fidelity reduced-order linearized time-invariant helicopter models for integrated flight and on-blade control applications," in *Proceedings of the 41st European Rotorcraft Forum*, (Munich, Germany), Sep 1-4, 2015.

[32] V. Verdult, M. Lovera, and M. Verhaegen, "Identification of linear parameter-varying state-space models with application to helicopter rotor dynamics," *International Journal of Control*, vol. 77, no. 13, pp. 1149–1159, 2004.

[33] C. P. Massey and P. Wells, "Helicopter carefree handling systems," in *Royal Aeronautical Society Conference on Helicopter Handling Qualities and Control*, (London, UK), Nov 15-17, 1988.

[34] J. Howitt, "Carefree maneuvering in helicopter flight control," in *American Helicopter Society 51st Annual Forum Proceedings*, (Fort Worth, TX), pp. 287–298, May 9-11, 1995.

[35] P. K. Menon, V. R. Iragavarapu, and M. S. Whalley, "Carefree maneuvering in helicopter flight control estimation of rotorcraft limit envelopes using neural networks," in *American Helicopter Society 52nd Annual Forum Proceedings*, (Washington, D.C.), June 4-6, 1996.

[36] S. S. Mulgund and G. L. Zacharias, "A hybrid neural network-fuzzy logic limit protection system for rotorcraft," in *AIAA Guidance, Navigation, and Control Conference*, (San Diego, CA), July 29-31, 1996.

[37] J. F. Horn, A. J. Calise, and J. V. R. Prasad, "Flight envelope limiting systems using neural networks," in *AIAA Atmospheric Flight Mechanics Conference and Exhibit*, (Boston, MA), Aug 10-12, 1998.

[38] J. F. Horn, A. J. Calise, and J. V. R. Prasad, "Development of envelope protection systems for rotorcraft," in *American Helicopter Society 55th Annual Forum Proceedings*, (Montreal, Canada), May 25-27, 1999.

[39] J. F. Horn, A. J. Calise, and J. V. R. Prasad, "Flight envelope cueing on a tilt-rotor aircraft using neural network limit prediction," *Journal of the American Helicopter Society*, vol. 46, no. 1, pp. 23–21, 2001.

[40] I. Yavrucuk, J. V. R. Prasad, and A. J. Calise, "Adaptive limit detection and avoidance for carefree maneuvering," in *AIAA Atmospheric Flight Mechanics Conference and Exhibit*, (Montreal, Canada), Aug 6-9, 2001.

[41] I. Yavrucuk, J. V. R. Prasad, and A. J. Calise, "Carefree maneuvering using adaptive neural networks," in *AIAA Atmospheric Flight Mechanics Conference and Exhibit*, (Monterey, CA), p. 4495, Aug 5-8, 2002.

[42] V. Sahasrabudhe, J. F. Horn, N. Sahani, A. Faynberg, and R. Spaulding, "Simulation investigation of a comprehensive collective-axis tactile cueing system," *Journal of the American Helicopter Society*, vol. 51, no. 3, pp. 215–224, 2002.

[43] D. G. Miller and N. D. Ham, "Active control of tiltrotor blade in-plane loads during maneuvers," in *Proceedings of the 14th European Rotorcraft Forum*, (Milano, Italy), Sep 20-23, 1988.

[44] D. W. King, C. Dabundo, R. L. Kisor, and A. Agnihotri, "V-22 load limiting control law development," in *American Helicopter Society 49th Annual Forum Proceedings*, (St. Louis, MO), May 19-21, 1993.

[45] J. F. Horn, "Rotor state feedback for high bandwidth control and structural load limiting," in *Proceedings of the American Helicopter Society Flight Controls and Crew System Design Specialists' Meeting*, (Philadelphia, PA), October 2002.

[46] J. N. Rozak, *Impact of Robust Control on Handling Qualities and Fatigue Damage of Rotorcraft*. PhD thesis, The Pennsylvania State University, University Park, PA, 1995.

[47] D. O. Bridges, "Damage mitigating control of rotorcraft," in *American Helicopter Society 59th Annual Forum Proceedings*, (Phoenix, AZ), May 6-8, 2003.

[48] J. F. Horn, D. K. Tolani, C. M. Lagoa, Q. Wang, and A. Ray, "Probabilistic robust control of rotorcraft," *Control Engineering Practice*, vol. 13, no. 8, pp. 1037–1046, 2005.

[49] D. K. Tolani, J. F. Horn, A. Ray, and J. Chen, "Hierarchical control of future generation rotorcraft," in *Proceedings of the 2004 American Control Conference*, (Boston, MA), June 30 - July 2, 2004.

[50] D. K. Tolani, J. F. Horn, M. Yasar, and A. Ray, "Hierarchical control of rotorcraft for enhanced performance and structural durability," in *AIAA Guidance, Navigation, and Control Conference and Exhibit*, (San Francisco, CA), Aug 15-18, 2005.

[51] D. Caudle, J. F. Horn, E. Keller, C. Thaiss, and M. C, "Damage mitigation on a large rotorcraft using load alleviating control laws," in *AIAA Atmospheric Flight Mechanics Conference and Exhibit*, (National Harbor, MD), Jan 13-17, 2014.

[52] W. D. Anderson and E. R. Wood, "AH-56A (AMCS) compound helicopter vibration reduction," in *American Helicopter Society 30th Annual Forum Proceedings*, (Washington, DC), May 7-9, 1974.

[53] M. Sekula and F. Gandhi, "Effects of auxiliary lift and propulsion on helicopter vibration reduction and trim," *Journal of Aircraft*, vol. 41, no. 3, pp. 645–656, 2004.

[54] F. Gandhi and M. Sekula, "Helicopter vibration reduction using fixed-system auxiliary moments," *AIAA Journal*, vol. 42, no. 3, pp. 501–512, 2004.

[55] "Flightlab overview," tech. rep., Advanced Rotorcraft Technologies, Inc., Sunnyvale, CA.

[56] P. V. Kokotovic, R. E. O'Malley, and P. Sannuti, "Singular perturbations and order reduction in control theory, an overview," *Automatica*, vol. 12, no. 2, pp. 123–132, 1976.

[57] Anon, "Flying qualities of piloting vehicles MIL-STD-1797A," tech. rep., Department of Defense, Washington, DC, 1997.

[58] M. B. Tischler and R. K. Remple, *Aircraft and Rotorcraft System Identification: Engineering Methods with Flight Test Examples*, ch. 5, 13, 17. Reston, VA: American Institute of Aeronautics and Astronautics, 2 ed., 2012.

[59] M. B. Tischler, T. Berger, C. M. Ivler, M. H. Mansur, K. K. Cheung, and J. Y. Soong, *Practical Methods for Aircraft and Rotorcraft Flight Control Design: An Optimization-Based Approach*. Reston, VA: American Institute of Aeronautics and Astronautics, 2017.

[60] J. H. Blakelock, *Automatic Control of Aircraft and Missiles*. New York: John Wiley & Sons, 1965.

[61] Anon, *MATLAB/Simulink Release 2016a*. Natick, MA: The MathWorks Inc., 2016.

[62] Anon, "Aerospace - flight control systems - design, installation and test of piloted military aircraft, general specifications for," tech. rep., AS94900, SAE International, Warrendale, PA, 2007.

[63] J. F. Magni, S. Bennani, and J. Terlow, *Robust Flight Control: A Design Challenge*. New York: Springer, 1997.

[64] C. Ivler and O. Juhansz, "Evaluation of control allocation techniques for a medium lift tilt-rotor," in *American Helicopter Society 71 Annual Forum Proceedings*, (Virginia Beach, VA), May 5-7, 2015.

[65] T. Berger, C. M. Ivler, M. G. Berrios, M. B. Tischler, and D. G. Miller, "Disturbance rejection handling-qualities criteria for rotorcraft," in *American Helicopter Society 72nd Annual Forum Proceedings*, (West Palm Beach, FL), May 16-19, 2016.

[66] U. Saetti and J. F. Horn, "Load alleviation control design using harmonic decomposition models, rotor state feedback, and redundant control effectors," in *American Helicopter Society 74th Annual Forum Proceedings*, (Phoenix, AZ), May 14-17, 2018.

[67] U. Saetti and J. F. Horn, "Use of harmonic decomposition models in rotorcraft flight control design with alleviation of vibratory loads," in *American Helicopter Society 72nd Annual Forum Proceedings*, (West Palm Beach, FL), May 16-19, 2016.

[68] M. S. Allen, "Frequency-domain identification of linear time-periodic systems using LTI techniques," *Journal of Computational and Nonlinear Dynamics*, vol. 4, no. 4, p. 041004, 2009.

[69] W. Johnson, *Helicopter Theory*, ch. 5. Princeton, NJ: Princeton University Press, 1980.

[70] B. Etkin and L. D. Reid, *Dynamics of Flight: Stability and Control*, ch. 6, p. 183. New York: John Wiley & Sons, 1996.

[71] D. T. McRuer, I. L. Ashkenas, and D. Graham, *Aircraft Dynamics and Automatic Control*, ch. 6. Princeton, NJ: Princeton University Press, 1973.

[72] M. B. Tischler and E. L. Tobias, "A model stitching architecture for continuous full flight-envelope simulation of fixed-wing aircraft and rotorcraft from discrete-point linear models," tech. rep., U.S. Army Aviation and Missile Research, Development and Engineering Center, Redstone, AL, 2016.

Vita

Umberto Saetti

Umberto Saetti was born on December 10, 1991 in Mirandola (Modena), Italy. After completing his high school studies at Liceo Scientifico Galileo Galiei Mirandola, he entered Politecnico di Milano, Milan, in Fall 2010. He graduated from Politecnico di Milano in 2014 with a Bachelor of Science in Aerospace Engineering. At Politecnico di Milano he joined the student association Skyward Experimental Rocketry. Along with his colleagues of Skyward Experimental Rocketry, Umberto successfully launched the first university designed Italian rocket on November 27, 2013. Umberto joined the Pennsylvania State University in Fall 2014 to pursue his graduate studies in Aerospace Engineering. He obtained a Master of Science in Summer 2016 and went on to pursue a PhD in Aerospace Engineering and a concurrent Master of Science in Electrical Engineering, along with a PhD minor in Computational Science.